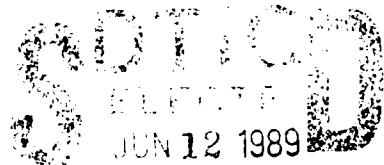


ETL-0523 AD-A208 806 ②

A Smart Mapping,
Charting and Geodesy
Control Generator
Phase II

W. Kober
J. Curlander
M. Karspeck
F. Leberl

Vexcel Corporation
2905 Wilderness Place
Boulder, Colorado 80301



December 1988

CK M

Approved for public release; distribution is unlimited.

Prepared for:

U.S. Army Corps of Engineers
Engineer Topographic Laboratories
Fort Belvoir, Virginia 22060-5546

03

Destroy this report when no longer needed.
Do not return it to the originator.

The findings in this report are not to be construed as an official
Department of the Army position unless so designated by other
authorized documents.

The citation in this report of trade names of commercially available
products does not constitute official endorsement or approval of the
use of such products.

DISCLAIMER NOTICE

**THIS DOCUMENT IS BEST QUALITY
PRACTICABLE. THE COPY FURNISHED
TO DTIC CONTAINED A SIGNIFICANT
NUMBER OF PAGES WHICH DO NOT
REPRODUCE LEGIBLY.**

UNCLASSIFIED

SECURITY CLASSIFICATION OF THIS PAGE

REPORT DOCUMENTATION PAGE**Form Approved
OMB No. 0704-0188**

1a REPORT SECURITY CLASSIFICATION UNCLASSIFIED		1b RESTRICTIVE MARKINGS	
2a. SECURITY CLASSIFICATION AUTHORITY		3 DISTRIBUTION / AVAILABILITY OF REPORT Approved for public release; distribution is unlimited.	
2b. DECLASSIFICATION / DOWNGRADING SCHEDULE		4. PERFORMING ORGANIZATION REPORT NUMBER(S) ETL-0523	
6a. NAME OF PERFORMING ORGANIZATION Vexcel Corporation	6b. OFFICE SYMBOL (<i>If applicable</i>)	7a. NAME OF MONITORING ORGANIZATION U.S. Army Engineer Topographic Laboratories	
6c. ADDRESS (City, State, and ZIP Code) 2905 Wilderness Place Boulder, Colorado 80301		7b. ADDRESS (City, State, and ZIP Code) Fort Belvoir, VA 22060-5546	
8a. NAME OF FUNDING / SPONSORING ORGANIZATION	8b. OFFICE SYMBOL (<i>If applicable</i>)	9 PROCUREMENT INSTRUMENT IDENTIFICATION NUMBER DACA72-87-C-0011	
8c. ADDRESS (City, State, and ZIP Code)		10 SOURCE OF FUNDING NUMBERS	
		PROGRAM ELEMENT NO.	PROJECT NO.
		TASK NO.	WORK UNIT ACCESSION NO.
11. TITLE (<i>Include Security Classification</i>) A Smart Mapping, Charting & Geodesy Control Generator, Phase II			
12. PERSONAL AUTHOR(S) W. Kober, J. Curlander, M. Karspeck, & F. Leberl			
13a. TYPE OF REPORT Annual	13b. TIME COVERED FROM 10/87 TO 6/88	14. DATE OF REPORT (Year, Month, Day) 1988 December	15. PAGE COUNT 26
16. SUPPLEMENTARY NOTATION			
17. COSATI CODES		18. SUBJECT TERMS (<i>Continue on reverse if necessary and identify by block number</i>) Automated Control Generation Inertial Navigation System (INS) Image Registration Global Positioning Satellite System (GPS)	
19. ABSTRACT (<i>Continue on reverse if necessary and identify by block number</i>) <p>The real-time automated registration of multi-sensor imagery begins with the generation of control information. A specific application may require the registration of newly acquired data to an existing spatial database (absolute registration), or to other images of a series (relative registration). This study examines the feasibility and upper-level design of a system capable of providing the control information required for a range of image registration tasks and image types. In general, the control generator we suggest will be guided by a spatial database maintaining information about the feature content of the area of interest. A rule-based query generator will extract candidate ground control optimized for the particular image type and geometry at hand.</p>			
20. DISTRIBUTION / AVAILABILITY OF ABSTRACT <input checked="" type="checkbox"/> UNCLASSIFIED/UNLIMITED <input type="checkbox"/> SAME AS RPT <input type="checkbox"/> DTIC USERS		21. ABSTRACT SECURITY CLASSIFICATION UNCLASSIFIED	
22a. NAME OF RESPONSIBLE INDIVIDUAL Lloyd Hauck		22b. TELEPHONE (<i>Include Area Code</i>) (202) 355-3833	22c. OFFICE SYMBOL CEETL-SL-C

Preface

This report was produced under contract DACA72-87-C-0011 for the U.S. Army Engineer Topographic Laboratories, Fort Belvoir, Virginia 22060-5546. The Contracting Officer's Representative was Mr. Lloyd Hauck. The Principal Investigator for this contract was Franz W. Leberl, Ph.D., of Vexcel Corporation.



Summary

This document is the final report for Phase II of an investigation into the feasibility and design of a smart control generator for the purpose of automated image-to-map and image-to-image registration. This Phase II effort is concerned with the problem of extracting control information in imagery and matching it with corresponding control information in spatial databases in order to calibrate the imagery. This problem is generically called "image-to-map matching". The use of other collateral navigational data sources, such as inertial navigation (INS) and Global Positioning System (GPS), is also addressed.

The work describes the scenarios that will motivate the selection of images, scenes, and collateral data and the processing of this data for generating control information.

Table of Contents

Preface	ii
Summary	iii
List of Figures	vii
List of Tables	xv
1.0 Introduction and Definition of Scenarios	1
1.1 Definition of Mission-Relevant Scenarios	1
1.2 The Problem of Image-Map Matching	3
1.3 Past and Recent Work in Image to Map Correspondence	5
1.3.1 Relevant Features	5
1.3.2 Extraction of Relevant Features	6
1.3.3 Feature Matching Techniques	7
1.3.3.1 Region-Based Matching	7
1.3.3.2 Boundary-Based Matching	12
1.3.4 Knowledge-Based Aerial Image Analysis	14
2.0 Generation of Control Information Using INS/GPS	15
2.1 Inertial Navigation Systems (INS)	15
2.1.1 Gyroscope Technologies	15
2.1.2 INS Error Sources	16
2.2 Global Positioning System (GPS)	18
2.2.1 GPS Error Sources	19
2.2.2 Differential GPS	20
2.3 Combined Use of INS/GPS for Control Information	21
2.3.1 Types of GPS/INS Combinations	21
2.3.2 Flight Path Estimation	22
2.3.3 Example Data Set	27
2.3.4 Real-Time Compensations for SAR Imaging	27

3.0 Generation of Control Information Using Terrain Data	32
3.1 Generation of Synthetic Imagery	33
3.1.1 Synthetic SAR Imagery	33
3.1.2 Synthetic Optical Imagery	34
3.2 Use of Terrain-Induced Shading for Control	34
3.2.1 Extraction of Shadows from SAR Imagery	35
3.2.1.1 Thresholding	35
3.2.1.2 Vectorizing Boundaries	37
3.2.2 Matching Techniques Using Shadows to Estimate Sensor Position	37
3.2.2.1 Discussion of Algorithms	38
3.2.2.2 Results	43
3.2.3 Analysis of Robustness	44
3.3 Use of Terrain-Induced Shading for Control	44
4.0 Generation of Control Information Using Feature Data	92
5.0 Generation of Control Information Using Image Segment Data	111
6.0 Generation of Control Information Using Satellite Ephemeris Data	112
7.0 Rule-Based Issues for Generation of Control Information	115
7.1 Overview on Rules for Image Control	116
7.2 Meta-Rules	118
7.2.1 Meta-Rules at Level 1	118
7.2.2 Meta-Rules at Level 2	124
7.2.3 Meta-Rules at Level 3	125
7.2.3.1 Planimetry	125
7.2.3.1.1 Planimetry Rules of Thumb	125
7.2.3.1.1.1 Image Formation Rules of Thumb	125

8.0 Spatial Database Issues	127
8.1 Data Structures	127
8.2 Database Management Functions	128
9.0 Summary and Conclusions	130
10.0 Appendices	131
10.1 Photogrammetry	131
10.2 Radargrammetry	132
11.0 References	134

Figure	Title	List of Figures	Page
1.1		Functions Required for Extracting Tactically Relevant Information from Imagery	2
3.1(a)		Four Adjacent Height Values in a Digital Elevation Model	46
3.1(b)		Vectors Corresponding to the Surface Gradient and the Surface Normal	46
3.1(c)		The Magnitude of the Energy Reflected Along the Range Vector R is Dependent Upon the Cosine of γ	46
3.2		The Actual Imaging Scenario	47
3.3		The Simulated Imaging Scenario	47
3.4		Actual SAR Image of Brazeau Area	48
3.5		Histogram of Actual SAR Image and Thresholded SAR Image	49
3.6		Vectorized Shadow Boundaries of SAR Image, Brazeau Range Area Minimum Contour Length: 10 pixels Threshold for Shadow Boundaries: 48	50
3.7		Vectorized Shadow Boundaries of SAR Image, Brazeau Range Area Minimum Contour Length: 10 pixels Threshold for Shadow Boundaries: 43	51
3.8		Vectorized Shadow Boundaries of SAR Image, Brazeau Range Area Minimum Contour Length: 10 pixels Threshold for Shadow Boundaries: 37	52
3.9		Vectorized Shadow Boundaries of SAR Image, Brazeau Range Area Minimum Contour Length: 10 pixels Threshold for Shadow Boundaries: 32	53
3.10		Vectorized Shadow Boundaries of SAR Image, Brazeau Range Area Minimum Contour Length: 10 pixels Threshold for Shadow Boundaries: 25	54
3.11		Simulated Image of Brazeau Area Sensor Height: 12 km Range: 15.49 km Maximum Height in Model: 2.5 km	55

(Continued on next page)

Figure	Title	List of Figures (Continued)	Page
3.12	Simulated Image of Brazeau Area Sensor Height: 10.25 km Range: 14.18 km Maximum Height in Model: 2.5 km		56
3.13	Simulated Image of Brazeau Area Sensor Height: 10 km Range: 14.00 km Maximum Height in Model: 2.5 km		57
3.14	Simulated Image of Brazeau Area Sensor Height: 9.75 km Range: 13.82 km Maximum Height in Model: 2.5 km		58
3.15	Simulated Image of Brazeau Area Sensor Height: 9.5 km Range: 23.35 km Maximum Height in Model: 2.5 km		59
3.16	Simulated Image of Brazeau Area Sensor Height: 8 km Range: 12.65 km Maximum Height in Model: 2.5 km		60
3.17	Simulated Image of Brazeau Area Sensor Height: 6 km Range: 11.41 km Maximum Height in Model: 2.5 km		61
3.18	SAR Gray Value Image Large Correlation Window Window Coordinates: 146, 243, 225, 225		62
3.19	Simulated Radar Image - 6 km Flight Altitude 50 x 50 Box to be Correlated with Large Box in SAR Gray Value Image Window Coordinates: 287, 313, 50, 50		63
3.20	SAR Gray Value Image Normalized Correlation Output Window 225 x 225 Box with Window in 6 km Simulated Image Window Coordinates: 291, 406, 50, 50		64
3.21	Simulated Radar Image - 8 km Flight Altitude 50 x 50 Box to be Correlated with Large Box in SAR Gray Value Image Window Coordinates: 287, 313, 50, 50		65

(Continued on next page)

Figure	Title	List of Figures (Continued)	Page
3.22	SAR Gray Value Image Normalized Correlation Output Window 225 x 225 Box with Window in 8 km Simulated Image Window Coordinates: 249, 357, 50, 50		66
3.23	Simulated Radar Image - 10 km Flight Altitude 50 x 50 Box to be Correlated with Large Box in SAR Gray Value Image Window Coordinates: 287, 313, 50, 50		67
3.24	SAR Gray Value Image Normalized Correlation Output Window 225 x 225 Box with Window in 10 km Simulated Image Window Coordinates: 240, 357, 50, 50		68
3.25	Simulated Radar Image - 6 km Flight Altitude 50 x 50 Box to be Correlated with Large Box in SAR Gray Value Image Window Coordinates: 287, 313, 50, 50		69
3.26	SAR Gray Value Image Sum of Differences Correlation Output Window 225 x 225 Box with Window in 6 km Simulated Image Window Coordinates: 297, 413, 50, 50		70
3.27	Simulated Radar Image - 8 km Flight Altitude 50 x 50 Box to be Correlated with Large Box in SAR Gray Value Image Window Coordinates: 287, 313, 50, 50		71
3.28	SAR Gray Value Image Sum of Differences correlation Output Window 225 x 225 Box with Window in 8 km Simulated Image Window Coordinates: 291, 414, 50, 50		72
3.29	Simulated Radar Image - 10 km Flight Altitude 50 x 50 Box to be Correlated with Large Box in SAR Gray Value Image Window Coordinates: 287, 313, 50, 50		73
3.30	SAR Gray Value Image Sum of Differences Correlation Output Window 225 x 225 Box with Window in 10 km Simulated Image Window Coordinates: 240, 357, 50, 50		74

(Continued on next page)

Figure	Title	List of Figures (Continued)	Page
3.31	Vectorized Shadow Boundaries in Simulated Image Brazeau Range Area, Alberta, Canada Sensor Height: 6 km Range: 11.41 km Maximum Height in Model: 2.5 km DEM Resolution: 60 m x 60 m x 1 m		75
3.32	Vectorized Shadow Boundaries in Simulated Image Brazeau Range Area, Alberta, Canada Sensor Height: 8 km Range: 12.65 km Maximum Height in Model: 2.5 km DEM Resolution: 60 m x 60 m x 1 m		76
3.33	Vectorized Shadow Boundaries In Simulated Image Brazeau Range Area, Alberta, Canada Sensor Height: 9.75 km Range: 13.82 km Maximum Height in Model: 2.5 km DEM Resolution: 60 m x 60 m x 1 m		77
3.34	Vectorized Shadow Boundaries in Simulated Image Brazeau Range Area, Alberta, Canada Sensor Height: 10 km Range: 14.00 km Maximum Height in Model: 2.5 km DEM Resolution: 60 m x 60 m x 1 m		78
3.35	Vectorized Shadow Boundaries in Simulated Image Brazeau Range Area, Alberta, Canada Sensor Height: 10.25 km Range: 14.18 km Maximum Height in Model: 2.5 km DEM Resolution: 60 m x 60 m x 1 m		79
3.36	Vectorized Shadow Boundaries in Simulated Image Brazeau Range Area, Alberta, Canada Sensor Height: 12 km Range: 15.49 km Maximum Height in Model: 2.5 km DEM Resolution: 50 m x 60 m x 1 m		80
3.37	Vectorized Shadow Boundaries in Actual SAR Image Brazeau Range Area, Alberta, Canada Approximate Altitude: 10 km Approximate Range: 14 km		81
3.38	Matched Output Points in Brazeau Range SAR Image Binarization Threshold: 37 Correlation Window: 240, 356, 50, 50		82

(Continued on next page)

Figure	Title	List of Figures (Continued)	Page
3.39	Matched Points in Brazeau Range Simulated Radar Image Flight Altitude: 10 km Correlation Window: 287, 313, 50, 50		83
3.40	Matched Points on the Vectorized Shadow Boundaries of the SAR Image (Lower) and the Synthetic Radar Image		84
3.41	Correlation Maxima and Sum of Differences Minima vs. Simulated Image Sensor Altitude for Brazeau Range Imagery		85
3.42	Intersections of Two Circles with Vertical Perturbation to Far Point Center Separation Approximately 0.1R		86
3.43	Intersections of Two Circles with Horizontal Perturbation to Far Point Center Separation Approximately 0.1R		86
3.44	Intersections of Two Circles with Vertical Perturbation to Far Point Center Separation Approximately 0.75R		87
3.45	Intersections of Two Circles with Horizontal Perturbation to Far Point Center Separation Approximately 0.75R		87
3.46a	Platform Offset (km) vs. Perturbation in DEM Ground Range (km) for Ill-Conditioned Coordinate Pair		88
3.46b	Platform Offset (m) vs. Perturbation in DEM Ground Range (m) for Ill-Conditioned Coordinate Pair		88
3.47a	Platform Offset (km) vs. Perturbation in DEM Ground Range (km) for Well-Conditioned Coordinate Pair		89
3.47b	Platform Offset (m) vs. Perturbation in DEM Ground Range (m) for Well-Conditioned Coordinate Pair		89
3.48a	Platform Offset (km) vs. Perturbation in DEM Height (km) for Ill-Conditioned Coordinate Pair		90
3.48b	Platform Offset (m) vs. Perturbation in DEM Height (m) for Ill-Conditioned Coordinate Pair		90

(Continued on next page)

Figure	Title	List of Figures (Continued)	Page
3.49a	Platform Offset (km) vs. Perturbation in DEM Height (km) for Well-Conditioned Coordinate Pair		91
3.49b	Platform Offset (m) vs. Perturbation in DEM Height (m) for Well-Conditioned Coordinate Pair		91
4.1	Brazeau Range Aerial Image, Alberta, Canada NHAP Photography Digitized at USC, Frame 176		95
4.2	Sobel Edge Image of NHAP Frame 176, Original Histogram, Brazeau Range Aerial Photography, Alberta, Canada		96
4.3	Reduced Resolution Sobel Image of Frame 176, Original Histogram, Brazeau Range Aerial Photography, Alberta, Canada		97
4.4	STAR-2 Radar Image of Brazeau Range Area		98
4.5	Comparison of Lee Sigma Filtered Versions of STAR-2 Radar Imagery (Left to Right) Sigma = 0, 15, 30, 45		99
4.6	Histogram of STAR-2 Radar Image		100
4.7	STAR-2 Image of Brazeau Range Area Preprocessing: Lee Sigma Filter Sobel Edge Image Threshold at Mean + Sigma		101
4.8	STAR-2 Image of Brazeau Range Area Preprocessing: Lee Sigma Filter Sobel Edge Image Threshold at Mean + 2 * Sigma		102
4.9	STAR-2 Image of Brazeau Range Area Preprocessing: Lee Sigma Filter Sobel Edge Image Threshold at Mean + 3 * Sigma		103
4.10	STAR-2 Image of Brazeau Range Area Preprocessing: Lee Sigma Filter Threshold by Bimodal Histogram Sobel Edge Image		104

(Continued on next page)

Figure	Title	List of Figures (Continued)	Page
4.11	STAR-2 Image of Brazeau Range Area		
	Preprocessing: Lee Sigma Filter		
	Threshold by Bimodal Histogram		
	Sobel Edge Image		
	Threshold at Mean + Sigma		105
4.12	STAR-2 Image of Brazeau Range Area		
	Preprocessing: Lee Sigma Filter		
	Threshold by Bimodal Histogram		
	Sobel Edge Image		
	Threshold at Mean + 2 * Sigma		106
4.13	STAR-2 Image of Brazeau Range Area		
	Preprocessing: Lee Sigma Filter		
	Threshold by Bimodal Histogram		
	Sobel Edge Image		
	Threshold at Mean + 3 * Sigma		107
4.14	STAR-2 Image of Brazeau Range Area		
	Preprocessing: Lee Sigma Filter		
	Threshold by Bimodal Histogram		
	Vectorization of Edges		108
4.15	STAR-2 Image of Brazeau Range Area		
	Preprocessing: Lee Sigma Filter		
	Threshold by Bimodal Histogram		
	Vectorization of Edges		
	2X Resolution Reduction		109
4.16	Subsampling the Feature Mask		110
4.17	Threshold Selection		110
7.1	Top-Level View of Image Control		119
7.2	Types of Image Control Information		119
7.3	Criteria for Choice and Evaluation of Planimetry Features for Control		120
7.4	Basic Physics of Received Signal as a Function of Object and Sensor		120
7.5	Heuristic "Rules of Thumb" Based on Imaging and Feature Extraction Considerations		121

(Continued on next page)

Figure	Title	List of Figures (Continued)	Page
7.6	Three Sensor Types Considered		121
7.7	Sensor Physical Determinants for SAR Feature Detectability		122
7.8	Object Physical Determinants for SAR Feature Detectability		122
7.9	Heuristics Concerning Sensor Characteristics Influencing Feature Detectability		123

List of Tables

Table	Title	Page
2.1	Comparison of Inertial Navigation System (INS) and Global Positioning System (GPS)	28
2.2	GPS Error Source Budget	28
2.3	Gyroscope Error Budgets	29
2.4	Accelerometer Error Budgets	29
2.5	Inertial System Initial Condition and Gravity Disturbance Error Budgets	30
2.6	Performance Summary of Low, Medium, and High Quality Hybrid Aided Inertial Navigation System Candidates	30
2.7	Hybrid System Performance Degradation Due to One Hour Total Jamming	31

1.0 Introduction and Definition of Scenarios

This Phase II effort is concerned with the problem of extracting control information in imagery and matching it with corresponding control information in spatial databases in order to calibrate the imagery. This problem is generically called "image to map matching." The use of other collateral navigational data sources, such as inertial navigation systems (INS) and Global Positioning System, is also addressed.

Section 1 describes the scenarios that will motivate the selection of images, scenes, and collateral data and the processing of this data for generating control information.

Issues involving INS and GPS are discussed in section 2, along with some results of using actual INS and GPS data for image calibration.

Techniques for using features in synthetic images generated from terrain data to provide control information is described in section 3.

Algorithms for choosing and extracting spatially extended features in images and matching their descriptions in DFAD data are explored and demonstrated for image control in section 4.

A discussion of the use of image segments for control information appears in section 5.

Techniques for calibration using satellite ephemeris data are discussed in section 6.

A discussion of rule-based considerations for control information appears in section 7.

Spatial database issues are considered in section 8.

1.1 Definition of Mission-Relevant Scenarios

Two tactical mission scenarios drive the research and test cases for this Phase II effort, and are distinguished by the presence or absence of GPS data. Both scenarios involve optical or Synthetic Aperture Radar (SAR) imagery sensed from aircraft platforms, as distinct from satellites. This imagery must be properly calibrated to allow the extraction of any positional estimates of tactically relevant targets. ETL's overall concept of the various functions that are required for extracting tactically relevant information from imagery is shown in Fig. 1.1.

The scenes which were selected for demonstrating and testing calibration concepts involved geometrically extended features, variations in shading caused by local terrain slopes, or shadows generated by occluding terrain. The usual ground-based navigational aids such as beacons or air traffic control radar were assumed not to be available for tactical mission scenarios.

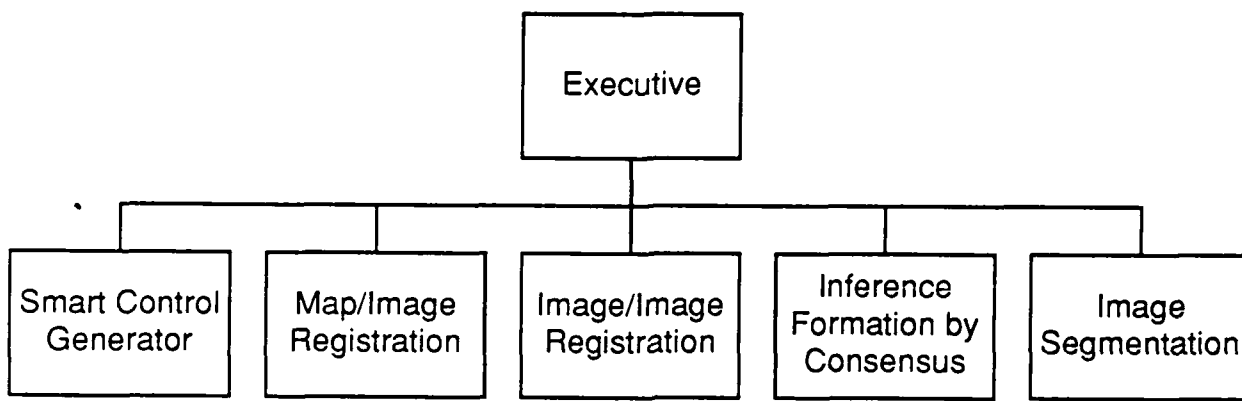


Figure 1.1
Functions Required for Extracting Tactically
Relevant Information from Imagery

The first tactical scenario concerns the calibration of imagery using inertial navigation system (INS) data along with a prior flight plan and/or flight log. The flight plan represents the desired approximate path of the aircraft. The pilot will use the output of the INS and visual sighting of landmarks in attempting to execute this flight plan.

The INS positional data is typically accurate over short time spans, but suffers from drifts over longer periods due to cumulative integration of errors. The heading information will be assumed to be accurate to within a degree, because it is available from other sources such as compass. Therefore, landmark sightings can be important for making positional corrections during longer missions, and the resulting maneuvers can be recorded in a pilot's log.

Imaged landmarks, either point-like or extended features, and terrain-induced shadows can provide more accurate calibration information. The INS data and the flight plan/log data provide approximate locations for the platform which can be used to initialize more precise position estimates using the pixel locations of such identifiable features.

The other tactical scenario involves the use of data from the Global Positioning System (GPS), along with INS data for calibrating imagery. This GPS data can be used with the INS data in a number of ways in order to improve the platform's flight path estimates. Because of the high accuracy of GPS, no additional positional corrections using imagery should be necessary. Instead, the main issue is how to combine INS and GPS.

Issues involving INS and GPS will be discussed in section 2.3.1, and the theory and results of using actual INS and GPS data for image calibration will be presented in sections 2.3.2 and 2.2.3 respectively. Flight plan or log data, when available, can be used to give initial estimates of the flight path.

1.2 The Problem of Image-Map Matching

In the following discussions, we shall use the term "maps" in the more general sense of meaning map information that is also available in feature and terrain databases as well as in ordinary maps themselves.

Image-map matching is the process of assigning a map coordinate to each pixel in the sensed image. This task can be achieved in a number of ways. One approach involves computing an estimate of the sensor platform position and possibly the sensor attitude. This problem is called "resection in space" in photogrammetric usage. Some other approaches are briefly mentioned in section 3.

In the past, resection in space has been achieved with computational procedures which relate individual pixel locations to ground control points with known geographic coordinates. These procedures are based on exploiting point-point correspondences. If enough individual control points are imaged and recognized, then such procedures are sufficient. However, often an imaged scene does not contain the signatures of individually recognizable control points, but does contain contours of known objects.

Little work has been done to generalize such resection in space procedures to exploit contour-contour correspondences. This subject is discussed in section 3.

The resection in space problem requires the previous determination of point-point or contour-contour correspondences. This correspondence problem is difficult because of a number of reasons involving differences in data types, levels of detail, accuracy, and data validity.

Concerning the latter issue, it is clear that maps are much more static than actual scenes in the real, dynamically changing world. For example, rivers meander and sometimes even dry up from one season to the next. Forest regions can be burned or cut, urban areas can be built up, and roads can be built. Even if scene content were not unchanged, as in the above cases, images of the same scene can change because of environmental effects such as rain or snow. Clearly, maps are not updated at a rate sufficient to accommodate such changes.

Maps and images differ in the content of their respective data. Maps generally contain information of a geometric nature, whereas images are formed from radiometric as well as geometric effects.

Maps and images also have incompatible data formats. Images are presented in raster format and maps in vector format. Planimetric maps also contain a great deal of non-visual data, such as textual and pictorial annotations, border lines, etc.

Real imaged scenes generally exhibit wide varieties of rich detail at many scales of length. Maps, on the other hand, are abstractions of much less detail at many fewer scales of length, and contain information on a more macroscopic level.

Another difference between the two data types involves accuracy and consistency. Images can support high measurement precision with high pixel resolution but require collateral ground truth data to support high accuracy. Maps can be highly accurate in principle, but often contain inconsistencies and approximations which can cause problems when trying to merge these two data sources.

For example, such inconsistencies can arise when performing updates to maps using real imagery. A typical problem that arises, called the "juxtaposition problem" [Goodenough,87], involves the outline of a newly added feature, obtained from imagery, incorrectly overlaying the outline of a feature already on the map.

Such inconsistencies would be more tractable if there were more descriptive information available on the construction of the map details. However, a map is an iconic abstraction of a real geographic region, and there are in general a number of undocumented interpolations and generalizations between the final iconic representation and the original data sources [McKeown,87].

Because of its importance to numerous applications, the problem of image-map matching has generated considerable attention. In the following section there is a discussion of some of the work in this area.

1.3 Past and Recent Work in Image To Map Correspondence

Because maps and images have differing data formats and data contents, any attempts at comparing and matching the information between the two types will require a common representation and common data content. Therefore, the structurally richer, sensed image must be processed so that abstractions compatible with map or spatial database information are formed from its individual pixel patterns.

These abstractions, i.e. features, from the sensed images are then matched with the data in maps or spatial databases. The relevant issues then concern the type of features to be used for matching, their extraction, their organization, and the processes for matching using these features. Some of the particulars of previous methods will be examined in the course of discussing these issues.

In the past, work on this problem and on the more general problem of interpreting aerial imagery was entirely concerned with the development of lower-level image processing procedures for extraction and matching. Reviews of such procedure-oriented work can be found in [Leberl,82], [Fischler,81], and [Medioni,84]. The more general area of model-based image analysis is thoroughly reviewed in [Binford,82], and more recent work is selectively discussed in [Kalvin,86]. Aspects of some of these works are discussed in the next sections.

However, some recent work has stemmed from the point of view that progress on more general image understanding and interpretation problems cannot be achieved by only working with lower level data and procedures. Some sort of "higher-level knowledge" is required for interpreting images and relating their content to other data sources such as maps.

Lower-level processes based entirely on pixel luminance values can often lead to ambiguities or errors. Therefore, there may be a requirement for a more robust synthesis allowing errors, inconsistencies, and partial evidence from the results of these processes. A good example of such a synthesis on a procedural level can be found in [Fischler,81], and is discussed in section 1.3.2.

Such a synthesis often depends strongly on the context of the objects being viewed. This context is the "knowledge" about real-world objects and their relationships. Recent work in AI has focused on methods of representing such knowledge and the use of non-procedural programming languages, such as PROLOG, for making reasoned conclusions in narrowly focused domains.

The more general area of aerial image "understanding" is beyond the scope of this effort. However, section 1.3.5 contains a discussion of some of the relevant work in knowledge-based aerial image understanding in order to survey some of the ideas which can be relevant to image-map correspondence.

1.3.1 Relevant Features

Because of the geometric nature of information stored in maps, the features to be abstracted from sensed images have been largely of a geometric nature also. Intuitively these features involve extracted boundaries of major regions or

large curvilinear objects, as well as regions themselves. This intuition is reflected in the practice of representing the data stored in maps and feature databases by templates of features, i.e. iconic data. However, terrain databases differ from these types of data and contain data suitable for surface description.

The visible portions of opaque three dimensional objects correspond to points, contours, or surfaces. The two dimensional imaged signatures of these objects are points, contours, and regions. In the past, the type of feature correspondence that was exploited for image-map matching was point-point. Because sufficiently many individually recognizable control points are not always present in imagery, the generalization to contour-contour correspondence can become important. Contour-contour mapping using DFAD data is discussed in section 4.

Other image signatures with definitive contours are terrain-induced shadows. The use of this type of feature for image-map matching is described in section 3.2.

The extraction of contours depends on the existence in the imagery of relatively sharp changes in gray-values rather than smooth changes. This subject is discussed in more detail in section 1.3.2.

On the other hand, the use of smoothly changing image intensities does not seem to have been greatly exploited in image-map correspondence, and has been associated more with robotics and industrial inspection under the heading of "photometric stereo".

Photometric stereo [Horn,86] is an example of the usage of shading information for identification of industrial parts. This technique exploits the relationship between local surface orientations and variations in image intensities.

Photometric stereo is part of a more general subject area loosely called shape-from-shading. The use of terrain-induced shading would represent an option for image-map matching if there were a lack of identifiable points or contours within a sensed image. The use of such terrain-induced shading has not been explored for image-map matching to the same extent as have boundary and point matching.

However, one very notable exception is described in [Horn,78], where optical synthetic images are created using a terrain model. The extension of this method to SAR imagery is described in section 3.

1.3.2 Extraction of Relevant Features

Clearly, the extraction of features in the sensed imagery should not proceed independently of the knowledge represented in the maps and databases, and any approximate knowledge of sensor platform position. Unguided segmentation based solely on image luminance values has long been known to lead to problems because object and intensity boundaries are not always the same. The use of this collateral map knowledge is loosely referred to as "map-guided segmentation", a term coined in [Barrows,77].

The approaches generally taken involve either boundary fragment extraction followed by some form of boundary matching or template matching.

Binary masks were used in [Kropatsch,81] for feature extraction using templates of objects known to have been in the vicinity of the imaged area. These masks were apparently not modified to take into account any projective effects, however.

The MAPS system [McKeown,87] also uses a priori location information to infer likely features present in the sensed image. It then projects models of these features into the image using the camera model, to aid in the extraction of these features and to make displacement calculations.

Two categories of edge extraction operators were used in [Fischler,81] for extracting roads in optical images. Type 1 operators were classified as those which never incorrectly classify, but which sometimes miss correct instances. Type 2 operators were those which sometimes misclassified, but which accurately measure true instances.

The output of these operator types is combined using a cost function to give a cost measure of a road going through every pixel in a some area. This cost function can incorporate some prior knowledge about road curvature and other parameters of road structure as weighting terms in this cost function. The extracted road is obtained as a least cost path through the connected graph of possible road locations. This least cost path is calculated using F^* , an efficient modification of the heuristic graph search algorithm A* [Pearl,84].

The importance of the method used in [Fischler,81] is the use of multiple, possibly contradicting, local sources of evidence, and using them to estimate a more global feature based on a minimization criterion.

1.3.3 Feature Matching Techniques

We will classify feature matching techniques as region-based or boundary-based, and these are discussed in sections 1.3.3.1 and 1.3.3.2 respectively. In either case, matching requires some analytic metric for making ranked comparisons of good, poor, and ambiguous matches. The challenge is to find metrics which are robust with respect to a wide variety of illumination and viewing conditions.

For the image-map matching problem, the approach is to infer some relationship of extracted features within the image and find the corresponding relationship within the map.

1.3.3.1 Region-Based Matching

Template matching using any of the various forms of the correlation metric has historically been a useful method for image-image matching. This method of matching is generally region-based rather than boundary-based, although it can also be used with some degree of success for matching high-pass filtered data. Another area-based metric is the sum of absolute differences [Barnea,72].

One classification scheme of image translation estimation methods appears in [Huang,81], and consists of: Fourier-based, matching, and differential.

Differential methods apply to image pairs with small amounts of relative translation, such as successive video frames. Such methods are based on Taylor's expansion for two variables truncated to linear terms. Obviously, such an approach is not applicable to this registration problem, and will not be discussed here.

Matching-type methods refer to the use of correlation-based methods as a measure of similarity for trial areas of overlap between image pairs. The use of such methods will be discussed in sections 3.2, 3.3, 4. and 5.

Fourier-based methods refer to an explicit use of the Fourier Shift Theorem [Champeney,73], which states that if two integrable continuous functions $f(x,y)$ and $g(x,y)$ are related as: $g(x,y) = f(x + \Delta x, y + \Delta y)$ then their Fourier Transforms are related as:

$$F(u,v) = G(u,v) \exp\{-j 2\pi (u \Delta x + v \Delta y)\}$$

In practice, such methods reduce to phase correlation.

A classical method for registering images is to successively register corresponding patches within the two images using an analytic metric for comparison. For each such patch in one image, candidate trial patches in the second image are compared using this metric. The trial patch in the second image which optimizes the metric is chosen as the "matching" patch for the given patch in the first image.

Historically, the normalized correlation coefficient has been the preferred metric, although other less robust versions of correlation-type metrics have been used because of computational advantages, such as non-normalized correlation, or variations on the sum of absolute difference metrics. These three are given below:

Normalized Correlation:

$$R(m,n) = \frac{\sum_{j=1}^N \sum_{k=1}^N F(j,k) F(j-m,k-n)}{\left[\sum_{j=1}^N \sum_{k=1}^N F(j,k) \right] \left[\sum_{j=1}^N \sum_{k=1}^N F(j-m,k-n) \right]}$$

Correlation:

$$R(m,n) = \sum_{j=1}^N \sum_{k=1}^N F(j,k) F(j-m,k-n)$$

Sum of Absolute Differences:

$$R(m,n) = \sum_{j=1}^N \sum_{k=1}^N |F(j,k) - F(j-m,k-n)|$$

Normalized correlation is the preferred method whenever computational cost is not an issue. The value of the normalized correlation coefficient is bounded absolutely, and always lies between -1 and +1. Therefore, absolute values of this metric close to +1 achieved for trial offsets are close to local maxima in the correlation surface. The normalized metric can allow for a constant multiplier between the gray-values for corresponding pixels in the two images. Also, the normalized correlation coefficient theoretically achieves its maximum value, in the absense of noise and nonlinearities, at the correct offset between the two images.

This is not always the case for non-normalized correlation algorithms, which can achieve high correlation values at some incorrect offsets simply because of high gray-values at certain localities. The sum of absolute values of differences generally performs better, in the sense of acceptable accuracy, than the non-normalized correlation approach, but also not as well as normalized correlation [Svedlow,78].

Correlation is computationally expensive. One route toward reducing the amount of computation has been to perform the equivalent operation in the Fourier domain, using the Fourier Convolution Theorem [Champeney,73]. The basis of computational savings using the FFT is that the latter requires a computation asymptotically proportional to $N \log N$ rather than N^2 , where N is the dimension of a square image. For relatively large images, there can be considerable savings using the FFT approach.

However, this approach does not deal with the observation that the determination whether a certain offset is very incorrect should somehow require less computation than the determination of a correct offset. This view is at the root of the idea of recursively searching for the correct offset in a "pyramid" of increasing-resolution versions of the image pairs [Rosenfeld,84].

This point-of-view is also the basis of the sequential approach using the sum of absolute differences metric in [Barnea,72]. Here, for any trial offset, whenever a pre-determined threshold has been exceeded before the entire sum has been evaluated, the summation is suspended and a new trial offset is evaluated.

Hybrid algorithms using this approach for a rough estimate of offset, followed by a version of normalized correlation using statistical pre-processing have been suggested [Pratt,73]. Clearly, this idea can be generalized to the use of other robust metrics following the initial rough estimate.

Another problem with correlation measures in general, including normalized correlation, includes the broad, flat nature of the peak regions in the correlation surface. This characteristic has advantages and disadvantages. An advantage of broad peaks is their "pull-in" range for search techniques that don't sample everywhere or that employ averaging, as in multi-resolution processing [Rosenfeld,84].

A disadvantage is that registration accuracy can be compromised whenever peaks are not sharp, and smaller perturbations due to noise can potentially have greater effects on accuracy.

This broad peak characteristic of correlation techniques occurs because spatial relationships in images are ignored for the most part. Instead, the values of the correlation metric are really related to energies of the broad areas within the images, i.e. the energy content of the low-frequency portions of the images. Since phase shifts of these lower frequencies can be relatively large compared to the pixel resolution and still be relatively small compared to the corresponding low-frequency wavelengths, there is a lack of sensitivity in correlation metrics to phase shifts. Therefore, correlation surfaces tend to have broad peaks.

One approach toward solving this problem has involved the preferential use of phase information in the images. The idea here is that the Fourier phase content of the images contains more accurate information than the low-frequencies which dominate correlation metrics. This is the basis for phase correlation methods [Kuglin,75,79], [Pearson,77], [DeCastro,87].

Using the previous example of the functions $f(x,y)$ and $g(x,y)$ related by translations Δx and Δy , the inverse Fourier transform of $\{F(u,v) / G(u,v)\}$ is just the inverse transform of the phase term, and thus is equal to the Dirac Delta Distribution evaluated at Δx and Δy , i.e. $\delta(\Delta x, \Delta y)$

Now, because of the effects of sampling and finite image sizes, sidelobes occur in addition to a main peak. Therefore, in practice, this technique reduces to correlation in the Fourier phase domain.

Such methods are also capable of subpixel accuracy with the use of interpolation, but suffer from the problem of potentially high sidelobes. Such a correlation surface, with sharp peaks and high sidelobes, does not lend itself easily to hierarchical processing with reduced resolutions because of the narrow "pull-in" range of the main lobe. However, used in conjunction with other methods which can acquire the main lobe, phase correlation can be a useful method for refining initial offset estimates to subpixel accuracy.

Another approach to rectify this broad peak problem has been to concentrate on the edge content in the images. This approach has both intuitive appeal as well as some theoretical justification.

Intuitively, it would seem that the "meaningful" information in an image lies at the locations of large, structurally significant contours and boundaries. Particularly in SAR images, the smaller edges are more often due to noise, speckle, and imaging effects. However, the larger edges are due to terrain and thematic value changes. It would seem that it is these edges and boundaries that should be involved in a registration scheme.

This notion has been explored on a more analytical basis from the standpoint of "optimally" filtering the images as a pre-processing step prior to registration. One approach has been to decorrelate the images by applying a "whitening" filter [Pratt,73], [Svedlow,78]. These methods essentially differ in their assumptions concerning image structure and statistical properties. The conclusions of these works point toward the use of pre-processing filters which can be approximated, under certain assumptions, by gradient filters [Svedlow,78], or Laplacian filters [Pratt,73].

Of course, there are some problems associated with this approach also. The high-frequency edge content of an image is relatively small compared to the total area of an image. Edges can be broken up slightly differently in two images which otherwise contain no other perturbations. Edges may also have slight variations in thickness. Therefore, such perturbations can lead to misalignment sensitivities for algorithms, like edge correlation, which examine the degree of "match" in overlapping edge images. One approach is to condition the edges in both images. This would include normalizing their intensities and broadening them. However, broadening edges can lead to reduction of registration accuracy.

These considerations mentioned above suggest that correlation-based matching involves considerable searching and is computationally expensive, unless the hierarchical "coarse-to-fine" approach previously discussed is used. The capabilities of correlation algorithms for achieving high accuracies often seems to require some form of pre-filtering to enhance edge content. However, certain potential instabilities are involved with the use of edge correlation.

In [Kropatsch,81] normalized correlation with a binary mask matrix was used for both feature extraction as well as feature matching in image-map matching. The use of correlation, however, assumes that there is little nonlinear geometric or radiometric distortion between the template and the actual imaged feature instance [Lahart,70].

Synthetic images corresponding to arbitrary viewing scenarios can be created using a terrain database. The available information in these synthetic images consists of shading corresponding to the interaction of the macro-relief of the terrain model and the viewing geometry.

Included in these shaded regions would be terrain-induced shadows. The shadows, although corrupted by noise, are more distinctive and should not involve other types of micro-structure. However, shadows are potentially more susceptible to certain instabilities. The use of shadows for image-map matching is discussed in section 3.

The use of synthetic images created from terrain databases for optical imagery is described in [Horn,78]. Two similar matching techniques were used. The first used the normalized correlation metric which normalizes the correlation coefficient by the standard deviations of the two images. The second method consisted of a modification of the normalizing term using the arithmetic mean [Moravec,77], which was easier to compute. The registration results were insensitive to the choice of normalizing terms.

As a variation on this theme, the use of synthetic images created from planimetric maps was also attempted in [Triendl,81] but specifically rejected as a general method in [Leberl,82]. The reason given for rejection was that maps contain a great deal of non-image data. Also, it was clear that matching with the sensed images would also require considerable filtering to remove the smaller levels of micro-structure present in imagery which are never present in maps.

1.3.3.2 Boundary-Based Matching

One method of boundary matching in binarized images which has achieved some success is "chamfer matching" [Barrows, 78]. This method uses a distance array between features in patches being matched, and estimates the translations between patches by searching for those offsets which minimize the distance array sums. This technique generally requires cleaner extraction of edges than does edge correlation. As is the case with all edge-based matching techniques, this metric is more sensitive to perturbations perpendicular to lines in the image than parallel to such lines.

One method developed at VEXCEL [McConnell,87] performs matching for translation estimation by creating binarized images from Marr-Hildreth operator zero crossings. This method has the advantage of accurate computation of edge content using this second-order operator, as well as the stability of regional matching. This method is especially well-suited for registering opposite-side satellite SAR images.

Another method was developed at VEXCEL for registering ice floes in arctic SAR imagery. This method performed boundary matching using dynamic programming, and reduced a two-dimensional search problem to one involving one-dimension. This method employed the psi-s representation of closed contours [Ballard,82], which allowed a convenient representation for translation and rotation. The particular implementation of the dynamic programming algorithm [Sankoff,83] was that used for string search and other sequence comparisons. The assumption was that the ice floes are rigidly rotated and translated, but some very localized distortions such as expansion, contraction, insertion and deletion could be tolerated.

Graph matching is a method which incorporates topological relationships into the matching process without undue emphasis on "exact" metric correspondence. This method has found considerable use in image-image matching, for example [Price, 82], [Ballard,82], [Nevatia, 82], [Shapiro,81], [Ayache,87]. Such problems involve subgraph isomorphism and can potentially be complex. Although graph matching problems belong to the worst-case computationally intractable class NP-complete [Aho,74], the use of heuristics to reduce the search has been successful.

In fact, all computationally successful graph matching algorithms must somehow use some means of distinguishing salient features in order to avoid the problem of combinatorial explosion when searching.

For example, in [Medioni,84], graph matching was used for both image-image and image-map matching. The computational complexity of matching was reduced by the use of a "coarse to fine" matching strategy which extracted isolated, long edges first, and matched these to the model at low resolution using relaxation.

Other boundary-oriented graph matching techniques have emerged from the field of robot vision. Typical of the problems encountered in this field is to correctly identify the individual parts in an imaged pile of parts which may be overlapping and are partially obscured by each other. Since the surfaces of these parts are often smooth, the boundaries contain most of the identifying information (although see section 1.3.1 for a brief discussion of photometric stereo).

An example of such work is [Bolles,82]. Significant local features are identified, such as corners and holes. These features are then clustered, and matching proceeds "cluster to cluster". The algorithm attempts to find the most significant cluster. A graph matching formulation is created wherein the nodes are matches of image and model features, and edges are pair-wise assignments between nodes. The match problem is then equivalent to searching for maximal cliques, which has complexity NP-complete. This method assumes that features will be clustered closely together.

Another method is that found in [Ayache,84]. Here, polygonal approximations of extracted boundaries and model sides are matched using a strategy of matching the longest sides first, as is done in [Medioni,84]. Lengths of sides and corner angles are used in measures of "compatibility". This method also attempts to generate "hypotheses" and continues until a sufficient number of hypotheses are evaluated and a good match score has been obtained.

The method of [Turney,85] divides a template of length n into $n/2$ subtemplates of length h . Every other pixel on the boundary of the template starts a subtemplate. Each subtemplate of each model object is then compared to the extracted object boundary in the sensed image.

The boundaries are represented using a variation of the psi-s representation mentioned previously. The matching metric is the least-squares measure of the differences. The method attempts to reduce the combinatorics of the comparisons by selecting "most salient" subtemplates. The successful matching of such salient subtemplates is weighted more than other matches. Again, this algorithm is slow.

The spirit of this last method, however, is carried out with significant computational improvements in [Schwarz,85]. Moreover, [Kalvin,86] continues computational improvements on this approach by employing the clever idea of "geometric hashing". This hashing is accomplished by the use of a "footprint" of an object's boundary. Only a small number of object footprints are retrieved for potential matching checks. This number of retrieved footprints does not depend strongly on the number of objects in the model database.

A footprint is a crude geometric characterization of an object boundary using 5 dimensions. A footprint is generated by a mapping that is not necessarily 1-1, but satisfies invariance under translation and rotation. continuity is essentially preserved by having locally similar objects into similar footprints. The five dimensional representation of each point of the object's boundary involves the first four Fourier coefficients of the boundary and the turning angle of a polygonal approximation at that boundary point.

The hashing occurs because 5-D space is divided into hypercubes of fixed size, and for each hypercube there is a list of all models whose footprints lie in that hypercube. In this way, searching for potential matches of boundary segments is considerably reduced.

1.3.4 Knowledge-Based Aerial Image Analysis

One of the tenets of this point of view is that a single pass over the data with any particular extraction algorithm will generally not be conclusive. Instead, what is required is an iterative process that examines results from one or more procedures, formulates hypotheses, and gradually eliminates competing hypotheses by a "convergence of evidence".

In particular, some important considerations for matching processes are the use of domain-specific collateral knowledge, partial matching, hypothesis formation, the use and propagation of constraints, selective attention and searching strategies, accumulation of confirming evidence, resolution of conflicting evidence, and efficiency.

2.0 Generation of Control Information Using INS/GPS

This section discusses the issues associated with the use of dead-reckoning aids such as inertial navigation systems (INS) as well as the Global Positioning System (GPS), also sometimes called NAVSTAR, for calibrating imagery.

The issues associated with INS and GPS separately are discussed in sections 2.1 and 2.2 respectively. The use of INS and GPS together is discussed in section 2.3.1 along with some results in the open literature. An example of the use of filtered INS/GPS data for calibrating actual detected SAR imagery is presented in section 2.3.2. Finally, a brief discussion on the use of INS/GPS data for making real-time phase adjustments to raw, complex SAR data is given in section 2.3.3.

2.1 Inertial Navigation Systems

An inertial navigation system (INS) contains an inertial measuring unit (IMU) and equipment for the stabilization and processing of sensor outputs from the IMU. The IMU provides sensor instruments for the three-dimensional monitoring of absolute rotation and non-gravitational translational acceleration. The latter is measured relative to a stationary point with respect to an inertial coordinate system or a point moving with constant velocity with respect to this coordinate system.

The instruments in an IMU are accelerometers for measuring linear accelerations and gyroscopes for measuring rotational rates. The IMU is either implemented as a gimballed or strapdown system. A gimballed system is mounted on a servo-driven platform, whereas a strapdown system is attached directly to the vehicle relative to a vehicle-based coordinate system. Gimballed systems are more expensive than strapdown, but are more accurate over longer time periods on the scale of hours. For flight times on the scale of minutes, strapdown systems are generally adequate. Errors also propagate differently for both types of systems.

A gimballed system is subjected only to relatively small, short angular rates because the servos counteract these rotations in order to preserve the "leveling" of the system. Moreover, only small torquers are required since the incremental rotations are small.

On the other hand, the strapdown system is subjected to all the vehicle rotations. The gyro rebalancing signals must be computed, requiring larger torquers. The accuracy of integrating these rebalancing signals is not as great as is obtained by the incremental stabilization of the gimballed platform. Likewise, the accelerometer directions are incrementally held along the reference axes in a gimballed system, whereas these accelerometer outputs must be recomputed onto reference directions in a strapdown system.

2.1.1 Gyroscope Technologies

The most complex component of an IMU is the gyroscope. In the past, the mechanical gyro has been used in an INS. The mechanical gyro is, of course, presently the best understood and perhaps still the most reliable type. However, it also has the greatest power and weight requirements and involves mechanically moving parts.

However, newer types of gyros based on laser technology have been in various stages of development. Such technologies do not depend on moving parts and friction, and include the ring laser gyro, the fiber optic gyro, and the hemispherical resonant gyro [Lundberg,87].

The ring laser gyro is for strapdown systems, and its operating principles are based on the interference pattern created by two planar, oppositely circulating laser signals. Mirrors are used to control the paths of these signals. By measuring phase shifts of the interference pattern, rotation about an axis perpendicular to this plane can be estimated. The corresponding power and weight requirements are less than for mechanical gyros. However, the observability of low rates of rotation is compromised by phase lock, and requires mechanical dithering to counteract [Lundberg,87]. Such a system has been in general service with some airline aircraft since 1982 [Divakaruni,87].

The fiber optic gyro is based on the same physical principles as the ring laser gyro, but does not use mirrors to control the laser signal paths. Instead, a fiber optic coil is used. No phase lock problem occurs at low rotation rates [Lundberg,87].

Finally, the hemispherical resonant gyro is based on the principle that standing, resonant waves on a hemisphere do not rotate at the same rate as the hemisphere. Some phase locking occurs at lower rotation rates, but is corrected using closed loop control [Lundberg,87], [Loper,87].

2.1.2 INS Error Sources

The error sources in an INS include bias errors and other degradations in the accelerometers and gyros. The following discussion summarizes some arguments in [Farrell, 76], in order to give a very simplified overview of such errors.

Bias errors due to incorrect initializations give rise to oscillations at the Schuler frequency. To see this, suppose a plane is travelling on an eastbound equatorial path with constant altitude. The platform must be kept level with a leveling command of \dot{V}_E/R . However, an initial nonzero uncertainty of:

\tilde{V}_E would overdrive the platform at a rate of:

$$\dot{\psi}_N = -\tilde{V}_E/R$$

$$\text{where } \tilde{V}_E = V_E - \dot{V}_E$$

\dot{V}_E is estimate of V_E

This incorrect tilt would result in aerodynamic lift, causing a retarding acceleration:

$$V_E = \dot{V}_E - g\psi_N \quad \dot{V}_E = g\dot{\psi}_N \quad (\psi_N, g \text{ given below})$$

Differentiating and combining these equations leads to:

$$\ddot{V}_E + (g/R) \tilde{V}_E = \ddot{\psi}_N + (g/R) \dot{\psi}_N = 0$$

The solutions to this linear, second order differential equation contains sinusoids at the Schuler frequency $W=(g/R)^{1/2}$ rad/sec. More generally, it can be shown that:

$$\tilde{V}_E = V_{E(0)} \cos Wt + (u\psi_{N(0)} + (n_{a2}/W)) \sin Wt + Rd(1-\cos Wt) + RD$$

$$\psi_N = \psi_{N(0)} \cos Wt + ((d/W) - (\tilde{V}_{E(0)}/u)) \sin Wt - (n_{a2}/g) + (w_2 n_{w3}/W^2) (1 - \cos Wt)$$

where: \tilde{V}_E , $\tilde{V}_{E(0)}$ are velocity error and initial velocity error, respectively in East direction

W is Schuler frequency

g is gravitational acceleration

R is nominal distance from center of Earth

$$u = \sqrt{g/R}$$

ψ , $\psi_{N(0)}$, $\psi_{A(0)}$ are respectively, the inertial system attitude uncertainty vector with respect to geographic reference system, and the initial uncertainties with respect to North, and North x East

n_{a2} is the East component of the acceleration error

n_{w1} , n_{w2} , n_{w3} are the components of the rotational drift rate

w_1 , w_2 , w_3 are the components of the angular drift rate of the reference frame

$$d = n_{w1} - w_2 \psi_{A(0)}$$

$$D \text{ is the time-varying drift rate} \\ = w_2 n_{w3} ((\sin Wt/W) - t)$$

Now, except for the last term involving azimuth drift rate, the velocity error consists of sinusoidal oscillations at $(W/2\pi)$ Hz, the Schuler frequency.

Interestingly, the tilt rate and accelerometer biases do not give rise to continuously increasing tilt or velocity errors. The velocity error produces a positional error in the East direction of:

$$\tilde{x}_E = \tilde{x}_{E(0)} + \tilde{V}_{E(0)} (\sin Wt/W) + R(\psi_{N(0)} + n_{a2}/g)(1 - \cos Wt) + RD(t - (\sin Wt/W)) + R w_2 n_{w3} ((1 - \cos Wt/W^2) - t^2/2)$$

Now, for time durations of $< (2\pi)/(10W)$, the following approximations are valid:

$$\sin Wt/W \approx t - (1/6)(Wt)^2 t$$

$$1 - \cos Wt \approx (1/2)(Wt)^2$$

$$\text{so: } \tilde{x}_e \approx \tilde{x}_{e(0)} + \tilde{v}_{e(0)} + 1/2(g\psi_{N(0)} + n_{a2})t^2 + R_d(st)^2 t$$

This last expression is now decomposed in terms of an initial position error, a linear term proportional to the initial velocity error, a quadratic term proportional to initial acceleration uncertainty, and a drift rate of $(1/6)R_d(Wt)$. This last term is about an order of magnitude less than d for time durations of about 1/6 the Schuler period, which is about 84.4 min [Meirovitch, 70]. This means that a relatively high drift rate could be tolerated for such short time periods.

Errors also arise from uncompensated gravitational uncertainties, which are equivalent to time-varying accelerometer errors. Other errors also arise from non-constant degradations of the components, such as the accelerometers and gyros.

Narrow band noise and these components can also lead to bias errors through a process called rectification (not to be confused with the photogrammetric term), as well as to random rotational drift rate and acceleration noise. Rectification is the process of creating constant and very slowly varying errors arising from products of oscillations with overlapping frequency spectra. Such products occur as unwanted interactions between noise oscillations and stabilizing computations or errors entirely within a particular instrument. Wideband errors such as gyro drift rate grow proportional to the square root of time, as opposed to the linear growth of constant drift rates.

2.2 Global Positioning System (GPS)

The Global Positioning System (GPS) is a system of navigational satellites expected to reach full operational 3-D capability in the mid 1990s. The system configuration will consist of six orbital planes inclined 55° relative to the equator at an altitude of about 20,000 km with an absolute orbital period of 12 hr., equivalent to a revisit time to the same rotating earth position of 24 hr.

Each orbital plane will contain three active satellites. Three additional satellites will serve as spares. Usually, at least four satellites will be in view anywhere on the earth at any time. Presently, seven satellites in two orbital planes are operational.

It is expected that GPS will be used as a stand-alone navigation aid, as well as with INS, heading reference systems, altimeters, on-board precision clocks, etc. [Stein, 87].

The GPS system operates by broadcasting four types of information [Lundberg,87]:

- o time signal
- o pseudo range measurement
- o integrated doppler measurement
- o ephemeris for each of the GPS satellites

Pseudo range is obtained by converting the received time-coded navigation signals into offsets relative to the internal clock of the GPS receiver. The term "pseudo range" is used because of the synchronization error between the user's and the GPS clocks, resulting in ambiguities of the time of transmission of the received signal.

Two L-band signals are continuously broadcast by each satellite. Two coded versions will be available on each band, but the higher precision P code will be encrypted whereas the lower precision C/A code will be generally available. The pseudo range measurement accuracies will be on the order of 1.5 m (RMS) for P code and 15 m for C/A code [Lundberg,87], and .1 m/sec velocity accuracies for P code [Teasley,87]. The integrated doppler measurement accuracy will be on the order of .2 m (RMS) [Lundberg,87].

2.2.1 GPS Error Sources

Four types of degradation are the major error sources affecting the determination of positional accuracy [Teasley,87]:

- o ionospheric delay errors
- o tropospheric delay errors
- o ephemeris prediction errors
- o geometric dilution of precision (GDOP)

Other sources of error include [Kleusberg,87]:

- o limited measurement resolution
- o clock errors
- o receiver noise
- o signal multipath

Ephemeris information is used for estimating the position of the GPS satellites in view. The pseudo-range and integrated doppler measurements are used to calculate the user's position relative to the satellites in view.

The accuracy of the ephemeris data broadcast by GPS is claimed to be about 12m (RMS) if ground station ephemeris updates are regularly received three times daily by GPS. In the event of jamming or other interference with these updates, the ephemeris errors could grow to about 20 km after 6 months [Lundberg,87]. However, by using cross-linking of range and integrated doppler signals among the GPS satellites themselves, this error could be reduced to about 40m, and user range errors to about 6m [Menn,87].

Additional loss of accuracy can occur when the geometry of the satellites visible to the user is such that these satellites are nearly coplanar. Another case is when less than four satellites are in view because of occlusion by terrain or satellite failure.

Such cases of unfavorable geometry are often quantified by the "Geometric Dilution of Precision" (GDOP). GDOP is the ratio of rms position and clock error to the 1-sigma satellite ranging error [Massatt,87]. Another ratio which is more useful to most users is the "Positional Dilution of Precision" (PDOP). PDOP is the ratio of rms position error to the 1-sigma satellite ranging error. Other ratios for particular positional component errors or time are also defined. A more intensive discussion of these issues along with some examples of calculations for affected latitudes, longitudes and operating times given minimum acceptable values of PDOP is found in [Massatt,87].

The first case occurs for a few regions along the 40th parallel. Some of these situations could be improved using equatorial orbits for the three spares [Stein,87].

Models of tropospheric delay and dual frequency measurements may be used to reduce the ionospheric delay errors [Kleusberg,87].

2.2.2 Differential GPS

There are a number of methods for potentially increasing the accuracy of positional determination using either the doppler portion of the signals or positional data relative to a known position. Such methods are referred to as "Differential" GPS.

One such scheme, described in [Beser,87], proposes the use of a stationary GPS receiver at a previously surveyed monitor location. Using the GPS-computed position and the known position of this monitor, correctional estimates can be computed and broadcast to users by GPS.

Such a relatively simple scheme would work reasonably well for three reasons [Kleusberg,87]. First, the satellite clock errors for a remote receiver and monitor would be the same and are cancelled. Also, satellite ephemeris errors affect measurements of simultaneous observers almost equally. Therefore, the computed position of a remote receiver could be computed relative to the monitor position. Finally, the remaining errors due to receiver noise, limited measurement resolution, and signal multipaths, are more in the high frequency range. These high frequency errors can be reduced by either smoothing with INS data or using the GPS carrier signal doppler.

Two alternatives for the use of doppler data are presently considered. One such method would filter the pseudo range time series with the doppler measurements for each visible satellite in order to derive the receiver's position and clock offsets. Another alternative would use the doppler measurements to filter the receiver positions which have been separately derived from pseudo range measurements.

Both of these methods would work better if smoothing of the entire appropriate data set were employed rather than recursive filtering.

2.3 Combined Use of INS/GPS for Control Information

A short summary comparison of the relative advantages of INS vs. GPS is given in Table 2.1 [Teasley,87]. It is clear that there would be advantages in using the two data sources together to reduce the effect of INS drift errors, GPS jamming, and GPS tracking of high dynamic maneuvers. Other uses include initialization of the INS alignments using GPS, using INS in the presence of partial or degraded GPS signals, and using the INS to aim the GPS antenna and control the receiver bandwidth [Bose,87].

The types of GPS/INS combinations are discussed in section 2.3.1, a scheme for loosely coupled, flight path estimation using combined GPS/INS data appears in section 2.3.2, and an example of the use of this procedure on real data is given in section 2.3.3. A brief discussion of some of the issues for real-time compensations to raw, complex SAR data is given in section 2.3.4.

2.3.1 Types of Combined GPS/INS

INS and GPS data can be combined jointly using a number of processing options. These options can be classified as loosely coupled or strongly coupled [Teasley,87].

Loosely coupled processing essentially involves processing the GPS data separately, and then using it to compensate for the bias arising from the INS drift errors. Therefore, a Kalman filter formulation for processing the INS data measurements models augmented states which include bias terms.

However, there are problems arising from the different clock errors for the two time sources.

Tightly coupled processing involves processing the raw GPS and INS data in a single filtering operation. The GPS pseudo range and doppler measurements and the INS linear and angular acceleration measurements are filtered using a combined dynamic model. In addition, the short-term INS data can be used to track the GPS carrier signals.

A simulation of such combined processing is reported in [Bose,87]. The initial error sources and some representative error budgets are given in Tables 2.2, 2.3, 2.4, and 2.5. Results are given for the non-jamming case in Table 2.6 and for the case of GPS jamming in Table 2.7.

Interestingly, one conclusion of this study [Bose,87] was that strapdown systems were found to be superior in performance for land vehicle navigation. This was mostly because the z-gyro height bias was more observable over hilly terrain using strapdown rather than gimballed systems.

2.3.2 Flight Path Estimation

This section contains an estimation procedure for combining GPS and INS in a loosely coupled form to estimate a flight path. This procedure is based on Kalman smoothing, as distinct from Kalman filtering. Essentially, such a smoothing procedure allows all the GPS and INS data for a given imaging period to be used as a whole rather than only successive portions of it to be used recursively. That such processing should lead to better estimates is not only intuitively appealing, but also theoretically valid [Bierman,73], [Gelb,74], [Maybeck,79].

Although such a procedure cannot be as efficiently implemented "on the fly" as a Kalman filter, it can be computed as a combination of time-forward and time-backward Kalman filters. Of course, all of the processed time-forward data must be kept to implement the time-backward filter.

The following is an implementation of a smoothing procedure based on the computational approach of [Bierman,73] for using GPS and INS data to estimate flight path parameters.

Algorithm to estimate aircraft position from INS/GPS data

1. Coordinate System

Let $R = (R_N, R_E, R_V)$ be the component of the aircraft position vector as measured in a rotating geographic coordinate frame with orthogonal unit vectors I_G, J_G, K_G . The origin is fixed to the earth at latitude, longitude (λ, ϕ) ; I_G points towards local North; J_G points toward local East; K_G points down.

The apparent aircraft velocity as measured in this same frame is $V = (V_N, V_E, V_V)$; i.e., $V_N(t) = \frac{d}{dt} P_N(t)$, etc

2. Single channel dynamic model.

Consider the case of 1 accelerometer which measures acceleration in the I_G (North) direction. Let the state vector be

$$x = \begin{bmatrix} R_N \\ V_N \end{bmatrix}$$

For short time durations we use the following model [Farrell, 76]:

$$(1) \quad \dot{x}(t) = Fx(t) + u(t)$$

where F is a (2×2) matrix of coefficients and u is a (2×1) vector representing the forcing function. Since:

$$\dot{R}_N(t) = V_N(t)$$

$$\dot{V}_N(t) = A_N(t) \quad (\text{the measured acceleration}),$$

we have

$$F = \begin{bmatrix} 0 & 1 \\ 0 & 0 \end{bmatrix}$$

$$u(t) = \begin{bmatrix} 0 \\ A_N(t) \end{bmatrix}$$

Equation (1) has the solution

$$x(t) = \Phi(t, t_0)x(t_0) + \int_{t_0}^t \Phi(t, \tau) u(\tau) d\tau$$

where the transition matrix Φ is computed by

$$\begin{aligned} \Phi(t, \tau) &= e^{F(t-\tau)} \\ &= I + F(t-\tau) + \frac{F^2}{2!} (t-\tau)^2 + \dots \end{aligned}$$

$$= I + F \cdot (t-\tau) + 0$$

$$= \begin{bmatrix} 1 & t-\tau \\ 0 & 1 \end{bmatrix}$$

Therefore

$$\begin{aligned} x(t) &= \begin{bmatrix} R_N(t) \\ V_N(t) \end{bmatrix} = \begin{bmatrix} 1 & t-t_0 \\ 0 & 1 \end{bmatrix} \begin{bmatrix} R_N(t_0) \\ V_N(t_0) \end{bmatrix} + \int_{t_0}^t \begin{bmatrix} 1 & t-\tau \\ 0 & 1 \end{bmatrix} \begin{bmatrix} 0 \\ A_N(\tau) \end{bmatrix} d\tau \\ &= \begin{bmatrix} R_N(t_0) + (t-t_0)V_N(t_0) + \int_{t_0}^t (t-\tau)A_N(\tau) d\tau \\ V_N(t_0) + \int_{t_0}^t A_N(\tau) d\tau \end{bmatrix} \end{aligned}$$

3. Single channel error model [Gelb, 74]

Let $\tilde{x}(t)$ be the measured value of the state vector $x(t)$. This is provided by the INS data;

$\tilde{x}(t) = x(t) - x(t)$ is the measurement error

$u(t)$ be the measured value of the forcing function (INS accelerometer data).

$w(t) = u(t) - u(t)$ is the noise in the accelerometer data.

Since the actual motion satisfies: $\dot{x} = Fx + u$

and the measured motion satisfies: $\dot{x} = Fx + u$

the errors must also satisfy: $\dot{x} = Fx + w$

At times $\{t_k, k = 1, \dots, N\}$ we get measurements of position g_k from GPS

$$g_k = \tilde{R}_N(t_k) - v_k$$

where $\tilde{R}_N(t_k)$ is the true position, and v_k is the error in the GPS position measurement. At each time t_k , form the difference between the INS measurements and the GPS measurements:

$$\begin{aligned} z_k &= \tilde{R}_N(t_k) - g_k \\ &= (\tilde{R}_N(t_k) - \tilde{R}_N(t_k)) - (\tilde{R}_N(t_k) - v_k) \\ &= v_k - \tilde{R}_N(t_k) \end{aligned}$$

$$\text{or } z_k = [-1 \quad 0] \begin{bmatrix} \tilde{R}_N(t_k) \\ v_k \end{bmatrix} + v_k$$

where we have now put this in the Kalman filter format. The "measurement matrix" is $H = [-1 \quad 0]$. The "measurement error" v_k is the error in the GPS positioning. It is assumed that $E(v_k) = 0$ and $\text{CoVar}(v_k) = R_k$.

The system model is

$$\dot{x}(t) = Fx(t) + w(t)$$

$$\text{or } \begin{bmatrix} \tilde{R}_N(t) \\ \tilde{v}_N(t) \end{bmatrix} = \begin{bmatrix} 0 & 1 \\ 0 & 0 \end{bmatrix} \begin{bmatrix} \tilde{R}_N(t) \\ v_N(t) \end{bmatrix} + \begin{bmatrix} 0 \\ \tilde{A}_N(t) \end{bmatrix}$$

$\tilde{A}_N(t)$ is noise in the INS acceleration measurements, with

$$E(\tilde{A}_N(t)) = 0, \text{Var}(\tilde{A}_N(t)) = \sigma_A^2.$$

The covariance of $w(t)$ is therefore

$$Q(t) = \text{covar}(w(t)) = \begin{bmatrix} 0 & 0 \\ 0 & \sigma_A^2 \end{bmatrix}$$

4. Single channel estimation procedure.

Since all of the measurements needed by the estimation process are available before beginning the procedure, we can use a Kalman smoother. This is guaranteed to give smaller errors than the "real time" Kalman filter [Gelb, 74], [Maybeck, 82]. The overall plan to estimate the aircraft position is as follows:

- Use the GPS position estimates, assumed GPS measurement variances, and assumed INS accelerometer variance to estimate the values of the INS error vector

$\tilde{x}(t)$. Use the Kalman smoother in step 5 below.

- Form the estimate of position and velocity using

$$x(t) = \hat{x}(t) + \tilde{x}(t)$$

where $x(t)$ is the measured INS data. The covariance of these estimates is given by the U_k matrices in the Kalman smoother.

5. Kalman Smoother [Gelb 74], [Maybeck, 82]

System Model

$$\dot{x}(t) = F x(t) + w(t)$$

$$\text{where } x = \begin{bmatrix} R_N \\ V_N \end{bmatrix}, \quad F = \begin{bmatrix} 0 & 1 \\ 0 & 0 \end{bmatrix}$$

$$\text{covar}(w(t)) = Q_k = \begin{bmatrix} 0 & 0 \\ 0 & \tau_A^2 \end{bmatrix}$$

Measurement Model

$$z_k = H_k x_k + v_k$$

$$\text{where } H_k = \begin{bmatrix} -1 & 0 \end{bmatrix}$$

$$w_k = x(t_k)$$

$$\text{var}(v_k) = R_k$$

Initial conditions

$$E(x(t_0)) = x_0,$$

$$\text{covar}(x(t_0)) = P_0 = P_0^t$$

$$E(w(t_k)v_k^t) = 0$$

for $k = 1$ to N , begin (iteration on k for forward filtering step)

State estimate extrapolation

In the following, the notation (-) refers to a quantity before an update, and (+) after an update.

States are first extrapolated from the $(k-1)$ st stage to the k th stage, and then estimated at the k th stage.

$$\hat{x}_k(-) = \Phi_{k-1} \hat{x}_{k-1}(+) \text{ where } \Phi_k = \begin{bmatrix} 1 & t_{k+1} - t_k \\ 0 & 1 \end{bmatrix}$$

$$P_k(-) = \Phi_{k-1} P_{k-1}(+) \Phi_k^t + Q_k$$

$$K_k = P_k(-) H_k^t [H_k P_k(-) H_k^t + R_k]^{-1}$$

State estimate update

$$K_k = P_k(-) H_k^t [H_k P_k(-) H_k^t + R_k]^{-1}$$

$$\hat{x}_k(t) = \hat{x}_k(-) + K_k [z_k - H_k \hat{x}_k(-)]$$

$$P_k(+) = [I - K_k H_k] P_k(-)$$

For backward filtering step,

$$\text{set } \hat{y}_N = \hat{x}_N^t$$

$$U_N = P_N^t$$

for $k = N-1$ down to 1, do begin

$$A_k = P_k^t (+) \Phi_k^t P_{k+1}(-)^{-1}$$

$$\hat{y}_k = \hat{x}_k(+) + A_k [\hat{y}_{k+1} - \hat{x}_{k+1}(-)]$$

$$U_k = P_k(+) + A_k [U_{k+1} - P_{k+1}(-)] A_k^t$$

end

$\{\hat{y}_k, k = 1, \dots, N\}$ are the resulting smoothed estimates
 $\{U_k, k = 1, \dots, N\}$ are the smoothed covariances

6. 3-dimensional extension

The simple model given here may be generalized to each of the three dimensions. The resulting dynamic model is uncoupled. If one also assumes that the measurement errors on each of the three directions I_G, J_G, K_G are uncorrelated, one can solve for each axis individually.

2.3.3 Example Data Set

An example of the use of the smoothing method of the previous section may be demonstrated on Intera's STAR2 imagery in a subsequent Option. Both INS and GPS data are available with the processed SAR imagery. The INS and GPS data were not filtered together by Intera using a tightly coupled algorithm, but were processed separately. We will combine the two data sources by smoothing in a loosely coupled fashion.

The INS data was used to make real-time phase and range corrections to the raw SAR data in the SAR processor (see section 2.3.4).

2.3.4 Real-Time Compensations for SAR Imaging

Real-time compensations for aircraft SAR imagery differ from those used in satellite SAR imagery (see sec. 5.) because of the differences in platform stability, the importance of earth rotation effects, and other factors. In Option 1, these effects may be studied in greater detail.

COMPARISON OF INERTIAL NAVIGATION SYSTEM
AND GLOBAL POSITIONING SYSTEM

<u>Parameter</u>	<u>GPS</u>	<u>INS</u>
Position	X	
Velocity	X	
Time	X	
Acceleration		X
Attitude		X
High Dynamic Performance		X
Time Invariant Accuracy	X	
Immunity to Countermeasures		X

Table 2.1 (from [Tensley, 87])

GPS ERROR SOURCE BUDGET

GPS Error Source	Symbol	Number of Sources	RMS Value
SPACE VEHICLE			
Clock			
Phase initial condition	δt_{so}	4	5.0 ft
Frequency bias	δf_{sb}	4	0.25×10^{-3} ft/sec
Frequency white noise	δf_{sw}	4	0.01 ft/sec/ $\sqrt{\text{Hz}}$
Ephemeris			
Position initial condition	$\delta X_{sc}, \delta Y_{so}, \delta Z_{so}$	12	5.0 ft
Position rate bias	$\delta X_{srb}, \delta Y_{srb}, \delta Z_{srb}$	12	0.56×10^{-3} ft/sec
ATMOSPHERIC			
Troposphere			
Phase bias	δt_{tb}	4	2.0 ft
Correlated noise	δt_{tc}	4	1.0 ft \pm 2.0 Hr.C.T.
Ionosphere			
Phase correlated noise	δt_i	4	5.0 ft \pm 0.5 Hr.C.T.
Multipath			
Position white noise samples	δt_{mw}	4	5.0 ft every 4 seconds
USER			
Clock			
Phase initial condition	δt_{uo}	1	1.0×10^4 ft
Frequency initial condition	δf_{uo}	1	10.0 ft/sec
Frequency rate bias	δf_{rub}	1	0.165×10^{-4} ft/sec ²
Frequency white noise	δf_{uw}	1	0.01 ft/sec $\sqrt{\text{Hz}}$
Frequency rate white noise	δf_{rw}	1	0.3×10^{-2} ft/sec ² $\sqrt{\text{Hz}}$
Receiver			
Multipath/pseudorange white noise samples	δP_{rw}	4	6.0 ft every 4 seconds
Delta pseudorange white noise	$\delta \Delta P_{rw}$	4	0.3 ft every 4 seconds

Table 2.2 (from [Bose, 87])

GYROSCOPE ERROR BUDGETS

Error Source	Units	RMS Values		
		Low Quality	Medium Quality	High Quality
Bias	°/Hr	1.0	0.1	0.01
Scale Factor	°/°	0.1	0.02	0.005
Scale Factor Asymmetry	°/°	0.01	0.002	0.0005
Mass Unbalance	°/Hr/g	0.5	0.1	0.02
Quadrature	°/Hr/g	0.3	0.05	0.01
Aniso-elasticity	°/Hr/g ²	0.2	0.04	0.01
Nonorthogonality	sec	100	20	10
Correlated Noise	° Hr $\sqrt{\text{sec}}$ (C.T.)	0.03 \pm 200	0.01 \pm 200	0.002 \pm 200
White Noise	° Hr $\sqrt{\text{Hz}}$	0.2	0.1	0.05
Trend	°/Hr/Day	0.01	0.002	0.0005

Table 2.3 (from [Bose, 87])

ACCELEROMETER ERROR BUDGETS

Error Source	Units	RMS Values		
		Low Quality	Medium Quality	High Quality
Bias	μg	500	100	50
Scale Factor	°	0.2	0.04	0.01
Scale Factor Asymmetry	°	0.05	0.01	0.005
Direct Quadratic Nonlinearity	$\mu\text{g g}^2$	140	70	20
Cross Quadratic Nonlinearity	$\mu\text{g g}^2$	50	20	5
Nonorthogonality	sec	100	20	10
Correlated Noise	$\mu\text{g}^2 \text{ C T}$	10 \pm 10 sec	3 \pm 20 sec	1 \pm 20 sec
White Noise	$\mu\text{g} \sqrt{\text{Hz}}$	30	10	5
Trend	$\mu\text{g Day}$	5	2	1

Table 2.4 (from [Bose, 87])

**INERTIAL SYSTEM INITIAL CONDITION AND
GRAVITY DISTURBANCE ERROR BUDGETS**

Error Source	Symbols	Units	RMS Values
Level Position	$\delta x_0, \delta y_0$	Sec	30
Altitude	δh_0	Feet	0
Velocity	$\delta v_{x0}, \delta v_{y0}, \delta v_{z0}$	ft/sec	0.1
Verticality	ϵ_x, ϵ_y	Degrees	1.0
Azimuth	ϵ_z	Degrees	2.0
Gravity Deflection	$\delta g_x, \delta g_y$	ug & NM (C.D.)	35 & 20
Gravity Anomaly	δg_z	ug & NM (C.D.)	35 & 20
Deflection Initial Condition	$\delta \epsilon_x, \delta \epsilon_y$	deg	35
Anomaly Initial Condition	$\delta \epsilon_z$	deg	35

Table 2.5 (from [Bose, 87])

PERFORMANCE SUMMARY OF LOW, MEDIUM, AND HIGH QUALITY HYBRID AIDED INERTIAL NAVIGATION SYSTEM CANDIDATES

Hybrid System Candidates	Average RSS East Velocity Error (Meters/Sec)	Average RSS North Velocity Error (Meters/Sec)	Average RSS Vertical Velocity Error (Meters/Sec)	Average RSS Azimuth Error (Mils)	Peak RSS Horizontal Position CEP (Meters)	Peak RSS Altitude Error (Meters)
GIMBALED INERTIAL						
Odometer Only	Low 0.120	0.122	0.037	21.8	360.0	38.7
	Medium 0.049	0.055	0.030	2.67	62.0	38.7
	High 0.046	0.049	0.027	0.74	72.0	38.0
With PLRS	Low 0.040	0.043	0.037	10.0	52.5	38.7
	Medium 0.03	0.037	0.03	1.76	25.8	38.7
	High 0.03	0.037	0.027	1.20	26.5	38.0
With GPS	Low 0.012	0.015	0.015	4.9	6.0	13.2
	Medium 0.01	0.012	0.015	0.79	6.0	13.2
	High 0.0091	0.0113	0.0146	0.46	6.0	13.2
With GPS & PLRS	Low 0.012	0.015	0.015	4.9	5.5	13.2
	Medium 0.01	0.012	0.015	0.79	5.5	13.2
	High 0.0091	0.0113	0.0146	0.46	5.5	13.2
STRAPDOWN INERTIAL						
Odometer Only	Low 0.076	0.091	0.040	10.2	131.0	32.3
	Medium 0.046	0.046	0.030	1.53	66.0	31.7
	High 0.043	0.043	0.030	0.69	62.0	31.7
With PLRS	Low 0.040	0.046	0.037	7.64	41.6	32.3
	Medium 0.03	0.037	0.03	1.20	20.3	31.7
	High 0.03	0.037	0.03	0.74	17.7	31.7
With GPS	Low 0.015	0.017	0.015	5.1	6.1	13.7
	Medium 0.01	0.012	0.015	0.83	6.0	13.7
	High 0.0085	0.0116	0.015	0.44	6.0	13.7
With GPS & PLRS	Low 0.015	0.017	0.015	5.1	5.5	13.7
	Medium 0.01	0.012	0.015	0.83	5.5	13.7
	High 0.0085	0.0116	0.015	0.44	5.5	13.7

Table 2.6 (from [Bose, 87])

**HYBRID SYSTEM PERFORMANCE DEGRADATION
DUE TO ONE HOUR TO .L JAMMING**

Hybrid System Candidates	Peak RSS Horizontal Position CEP (Meters)		Peak RSS Altitude Error (Meters)		Average RSS Azimuth Error (Mils)	
	Unjammed	Jammed	Unjammed	Jammed	Unjammed	Jammed
GIMBALED INERTIAL						
With PLRS	Low	52.5	68.0	38.7	38.7	9.95
	Medium	25.8	47.0	38.7	38.7	1.76
	High	26.5	50.0	38.0	38.0	1.20
With GPS	Low	6.0	140.0	13.2	31.2	4.86
	Medium	6.0	36.5	13.2	31.1	0.79
	High	6.0	33.0	13.2	31.1	0.46
With GPS & Unjammed PLRS	Low	6.0	15.0	13.2	31.1	4.86
	Medium	6.0	8.8	13.2	31.1	0.79
	High	6.0	8.8	13.2	31.1	0.46
STRAPDOWN INERTIAL						
With PLRS	Low	41.6	53.9	32.3	32.6	7.64
	Medium	20.3	37.0	31.7	31.8	1.30
	High	17.7	33.6	31.7	31.8	0.74
With GPS	Low	6.0	75.0	13.7	20.8	5.09
	Medium	6.0	36.5	13.7	20.7	0.83
	High	6.0	36.5	13.7	20.7	0.44
With GPS & Unjammed PLRS	Low	5.5	14.0	13.7	20.8	5.09
	Medium	5.5	8.1	13.7	20.7	0.83
	High	5.5	8.1	13.7	20.7	0.44

Table 2.7 (from [Bose, 87])

3.0 Generation of Control Information Using Terrain Data

This section discusses the use of terrain data for extracting control information to calibrate imagery. The simulated scenario will assume that approximate position estimates of the sensor platform will be available from an INS or combined INS/GPS source, and that the flight path direction will be accurate to within a degree [Mercer,87].

Two distinct methods for extracting control from terrain data will be described here. Both methods will employ synthetic images generated from assumed flightlines using terrain models.

Because the available sensed images are ground range images, the synthetic images must also be ground range images for any comparisons to occur. Because slant range images compress the near-ranges compared to the far ranges, ground range images are produced which are more visually pleasing. However, there are errors associated in producing the conversion to ground-range, and these errors are dependent on the terrain. Therefore, accurate ground range presentation really requires registration of the slant range image with the terrain.

The approach for generating control information for a SAR image, i.e. assigning a geographic location to every pixel, will be to determine the sensor platform position as a function of time. Ideally, the flight path for an aircraft should be straight and level. Of course, this does not occur in practice (see section 2.3.3 and 2.3.4). Therefore, straight line flight path approximations for smaller blocks of azimuthal lines will be attempted. These straight line approximations can be used as supplementary update measurements to remove the bias effects of drift in the INS data for estimating a flight path as a function of time. In this way, these measurements could be used in the same way as the GPS measurements are used for updates in the Kalman smoothing algorithm described in section 2.3.2. Of course, GPS measurements would be much more accurate.

Once a flight path or smaller flight path segments have been determined, i.e. the "resection in space" has been estimated, the range and doppler equations for each pixel can be used to intersect with the terrain model to obtain geographic coordinates [Leberl,83], [Kwok, 87], [Curlander, 87]. In the case of airplane SAR, usually no squint is used, and the doppler cone degenerates into a scanning plane.

An alternate approach would be to try to register the image to model coordinates without determining the exterior orientation of the sensor, i.e. the flight path. As is discussed in [Leberl,83], such approaches generally fall into three categories:

- o "rubber sheeting" interpolative methods using ground control points
- o using the projection equations and ground control points to estimate parameters
- o hybrid combinations of the above

It would seem that using the model to obtain the sensor flight path is the better approach because it directly uses the model information to generate control features such as shadows or shading.

The generation of synthetic SAR images appears in section 3.1. The use of shadows created by terrain occlusions for estimating sensor platform position is discussed in section 3.2. The use of terrain-induced shading for estimating sensor platform position is discussed in section 3.3. Finally, a brief summary of the problem of resection in space is treated in the Appendices, sections 9.1 and 9.2.

3.1 Generation of Synthetic SAR Imagery

Synthetic image generation for both SAR and optical imagery is discussed in this section.

3.1.1 Synthetic SAR Imagery

The present software for forming projected views assumes that the flight line, and therefore the azimuthal direction, is parallel to one of the model coordinate axes. If this is not the case, then the appropriate rotation of the model must be performed. Operationally, this is not much of a constraint since the flight path is assumed to be known within a degree. No squint angle is assumed, which is the usual case for aircraft SAR imagery. Therefore, the doppler equations reduce to planar scanning.

Essentially, the formation of projected views requires the calculation of a local surface orientation of the terrain model for each resolution element, and the suppression of occluded regions. Another component of image intensity which affects gray values in a real sensed image is local thematic value, ie. the scattering cross section coefficient.

Because such thematic values are not available in most terrain model data, their effect is ignored in these simulated views. The use of thematic values is irrelevant for the calculation of shadows in synthetic images.

However, when non-shadowed regions in a synthetic image are to be compared to the corresponding regions in a real sensed image, there will generally be intensity distortions which are not related to terrain. This issue is discussed in section 3.3.

The geometry of the imaging scenario and its inputs is shown in Fig. 3.1.

There are a number of considerations for producing such synthetic, aircraft SAR images:

- o intensity values
- o occlusions/radar shadows
- o range overlay
- o discretization artifacts

The intensity values are computed using the cosine of the local incidence angle of the radar beam with respect to the local surface facet normal. These intensities are computed for every terrain cell surface facet.

A separate file for occlusions or overlay is computed for every terrain cell surface facet. Occlusions are computed simply by checking for changes in the monotonicity of the angle (see Fig. 3.1) as one proceeds from the far range, r_f , to the near range r . Overlay is determined by whether the monotonicity of range offsets is violated as one proceeds from far to near range.

Discretization artifacts can potentially occur in the construction of a synthetic image because the changes in the range for terrain cell increments may involve jump discontinuities when measured as range resolution increments. If uncorrected, this leads to a synthetic image for which there are no returns for certain range resolution pixels.

A simple averaging scheme using oversampling is employed to offset this anomaly. Basically, this procedure oversamples the range buffer by some factor. For practical purposes, an oversampling factor of 4 was sufficient. Then the intensities for the final range cells of correct resolution are computed by averaging groups, in this case groups of 4, of contiguous cells from the oversampled buffer.

3.1.2 Synthetic Optical Imagery

A framed optical image is formed by pixels representing azimuthal and elevation angle "rays", instead of pixels representing azimuthal and range distances as in SAR. The same cosine relationship is used for calculating intensities as above. No overlay occurs as in SAR imaging, but shadows and occlusions are calculated using monotonicity of projection angle as before.

3.2 Use of Terrain-Induced Shadows for Control

There is no problem determining the occurrence of a shadow or locating its boundary in a synthetic image. However, the situation is obviously not quite as straight-forward in real imagery.

Shadows in a real SAR image are subject to two kinds of instabilities. A geometrically-induced instability involves the problem of edge migration due to small perturbations in the platform flightpath and unmodeled perturbations in the real terrain. A radiometrically-induced instability involves the uncertainty in the choice of a precise shadow threshold because of the effects of noise and speckle.

These geometrically-induced instabilities can arise whenever there is a portion of real terrain present that is not convex. Departures from convexity can potentially introduce relatively large changes in shadow contours for relatively small changes in platform position.

The extent of shadow boundary instabilities due to changes in the shadow threshold are potentially greater in the side of the shadow furthest away from the sensor. The shadow side closest to the sensor should have a stronger

radiometric edge because the terrain slopes near this geometric discontinuity often approach a near-specular orientation.

Because of the potential for such large changes, precise measurements on shadows are more appropriate for finer estimation of platform position rather than for acquisition.

3.2.1 Extraction of Shadows From Imagery

The approach for extracting the shadowed regions in the real imagery involves thresholding and vectorization. These issues are described in sections 3.2.1.1 and 3.2.1.2 respectively.

3.2.1.1 Thresholding

Segmenting shadows involves discriminating between highly specular no-return areas such as large bodies of water and true radar shadows due to terrain occlusions. It also involves carefully choosing a shadow threshold so that a clean delineation of the shadow boundary from the surrounding region is formed.

Solving the former problem of determining a specular no-return region is greatly aided by the use of prior knowledge of the nearby existence of lakes, reservoirs, etc. Such knowledge would be represented in DFAD or other feature data. This feature would then be actively searched for in the same way that a particular terrain shadow is searched for, given some hypothesized sensor platform position.

Without such prior knowledge, an evaluation of the degree of "goodness of fit" of each segmented potential shadow region would be the only way of deciding that the segmented region is a no-return region, or that there are terrain model errors. Such decision issues can be approached using a rule-based approach, and are discussed in section 7.

An examination of the intensities of a real STAR1 Intera SAR image (see Fig. 3.4) shows a clear bimodality of the histogram for shadow and non-shadow regions. This is shown in Fig. 3.5. The variations in shadow outline are shown in Fig. 3.6 - 3.10. As can be seen in these images, the variations in shadow shape are reasonably well-conditioned with respect to small threshold changes around the local minimum in the histogram separating shadow from non-shadow intensities.

For SAR images with a great deal of noise and speckle content, it may be necessary to prefilter the images using some nonlinear spatial filter prior to calculating the histogram. Two examples of such nonlinear filters which reduce these effects but still preserve edge structures relatively well are described in [Lee,86]. One of these, the "sigma filter", has been used by VEXCEL on SEASAT SAR images of arctic ice floes to reduce the effects of speckle prior to thresholding using the image histogram.

The sigma filter is based on a Gaussian distribution model of the pixel intensities in a (5x5) or (7x7) pixel window. The algorithm uses this statistical model for selective averaging of pixel intensities. The assumption is that real contours arise as pixels representing the higher percentiles of

the local distribution. Unfortunately, spot noise also satisfies this criterion. Only pixels belonging to the two-sigma range of the normal distribution, i.e. 99.5%, are averaged. The pixels falling outside this range remain as before. A special thresholding procedure, somewhat ad-hoc, is then applied to remove spot noise.

The other of these two algorithms is called the "local statistics" method. However, this name is somewhat misleading, since the real basis of this algorithm is estimation theory using local statistics in (5x5) and (7x7) neighborhoods. The method is based on a multiplicative noise model relating the observed pixel intensity as the product of the true "signal" at that pixel location and an independent noise term. A linear series expansion of this model giving the observed intensity as a function of the mean values of both the true signal and the noise term, assumed to be unity, allows an estimation of the mean and variance of the true signal as a function of the mean and variance of the observed intensity. These estimates of the mean and variance of the true signal are then used in a linear least-squares estimator to form an estimate of the actual pixel value of the true signal at that pixel location.

As an alternative, there are other approaches which could be used for thresholding shadows in images with histograms that do not have a clearly bimodal shape. One type of approach involves iterative relaxation methods [Rosenfeld,81]. Such a method assigns probabilities to a pixel's classification and uses the probabilities of neighboring pixels for iterative reinforcement. This iteration eventually converges with high probabilities accumulating for each class. It is claimed that the method is robust. Such methods can also be extended to include geometric properties, not just pixel intensity.

Another type of approach is to formulate analytic criteria that the desirable thresholding is to achieve. The approach used in [Dunn,84] computes that threshold which equalizes the probabilities of misclassifying pixels in the background and object. This method can also be extended, although not as efficiently, to compute a solution for the minimum probability of misclassification error. The method seems quite effective for highly speckled and noisy imagery because of some of the statistical independence assumptions made for neighboring pixels in (2x2) windows. However, the analysis explicitly ignores statistical contributions of pixel neighborhoods on borders between object and background. Therefore, this method may not perform well on images where the background-object borders represent a significant fraction of the total pixel content of an image.

The method of [Pun,81] develops an analytic measure of asymmetry of the image histogram based on the information theoretic definition of entropy. This method claims to have obtained some good results on images with quickly decaying histograms, such as high-pass filtered imagery.

The approach used in [Perez,87] uses the illumination-reflectance model of [Stockham,72] for imagery. In this view, image intensity is the product of a reflectance component associated with the scene content and an illumination component which may be spatially varying.

This method develops a spatially-varying, adaptive threshold function which can be implemented in raster fashion. This threshold function is approximated by a highly differentiable function whose Taylor series coefficients are modeled by certain exponential functions. This method is intended for imagery subject to slowly varying illumination. Therefore, this method is not recommended for use with heavily speckled SAR images, but may be appropriate for passive optical imagery.

For the actual SAR images presently used in this shadow matching study, no additional filtering was required prior to examining the histogram. However, an experiment was performed using the STAR-2 SAR image in the upper left quadrant in Fig. 4.5 to condition the image for feature extraction. The results of filtering this image in the upper left quadrant using the sigma filter with values of sigma = 0, 15, 30, 45 are shown in the other three quadrants.

3.2.1.2 Vectorizing Boundaries

Vectorization of a feature's boundary is the process of representing that boundary as a connected, ordered sequence of pixels. The vectorization procedure used in this effort consists of three modules, and is appropriate for binary images.

The first module is the executive module. This module scans an image window for binary region boundary pixels and determines whether the boundary region intersects the image window or is entirely within the window. In either of these two mutually exclusive cases, the executive calls either module two or three as appropriate.

The executive module scans the window as follows. First, it examines each of the four borders of the image window and searches for boundaries of binary regions. Upon detection of such a boundary, the second module is activated. The second module then tracks the boundary until it again intersects the window border. This module records consecutive boundary pixel locations in a special data structure, as well as in a raster format array to keep track of visited locations.

Next, the executive module examines the interior of the window line by line, and calls the third module whenever a region boundary is encountered that is not already identified as a previously visited location in the raster format array. The third module follows the edge of a binary region until it returns to the starting pixel. This module, just as the second module, also records consecutive boundary pixel locations in a special data structure and a raster format array.

3.2.2 Matching Techniques Using Shadows to Estimate Sensor Position

In section 3.2.2.1, there is a description of some of the algorithms used to estimate the sensor position using measures of similarity between real and simulated radar shadows. In section 3.2.2.2, there are some preliminary results using some of these methods.

3.2.2.1 Discussion of Algorithms

Once a shadow region has been thresholded in a real image, the outer boundary must be extracted and vectorized. Some low-pass filtering may be necessary if there is a great disparity in the resolutions of the real imagery and terrain model.

Matching of the shadow boundaries in the real and synthetic images can be accomplished in a number of ways. One type of metric would seek to match entire shadow regions in the real and synthetic images. Such metrics are briefly mentioned in section 1.3.3.1, and often involve correlation or sum of absolute differences. Because the shadow areas involve more pixels than the shadow boundaries, such methods should be quite robust to smaller errors in the data, but less sensitive to small changes in the platform position.

Other methods for matching could involve boundary matching techniques (see section 1.3.3.2). These methods would seem to have the potential for higher sensitivity to both platform position and errors in the data than area-based methods.

Both of these methods are used for estimation of platform positioning. The area-based techniques are used for acquisition and the contour-based techniques are used for finer adjustments.

There follows a discussion of the current method.

The actual imaging scenario is shown in Figure 3.2. The real slant range image is created by measuring slant ranges r_{A3} and r_{A4} obtained from the actual sensor position p to the points p_3 and p_4 . Then the ground range image is created by projecting these slant ranges into the ground as if the sensor were at the assumed position \hat{p} . All ground range measurements are relative to \hat{g}_{A0} .

The assumption is that \hat{p} is at altitude h_A and offset \hat{g}_{A0} , the 1st ground range line. Moreover, \hat{g}_{A0} is computed so as to have slant range equal to the measured nearest slant range r_{A0} .

Here, the origin is at the perpendicular projection to the ground of the assumed sensor position. This is not the origin of the DEM model. However, all the units can be converted to DEM units.

The pixel values for p_3 and p_4 in real ground range image are:

$$m_3^* = (\hat{g}_{A3} - \hat{g}_{A0})/\Delta g_r$$

$$m_4^* = (\hat{g}_{A4} - \hat{g}_{A0})/\Delta g_r$$

where: Δg_r = ground range resolution

The scenario for the simulated image is shown in Fig. 3.3. The simulated slant range image is created by measuring the slant ranges from the simulated sensor position p_s to the model points p_3 and p_4 . Denote these slant ranges by r_s , and r_{s4} .

The simulated ground range image is created by projecting the slant ranges r_{s_3} and r_{s_4} into the DEM ground plane from the (incorrect) sensor position p_s^* .

Now p_s^* is at altitude h_A and offset $-g_{AD}$ from the origin of the DEM.

Denote these simulated ground range projections of p_3 and p_4 by g_{s_3} and g_{s_4} .

The pixel values for p_3 and p_4 are: $m_3 = (g_{s_3}/\Delta g_r)$, $m_4 = (g_{s_4}/\Delta g_r)$ where Δg_r is ground range resolution.

(1) An initial guess to use for a straight line approximation of the actual flight path of the sensor relative to the scene is the assumed altitude and assumed ground range to the first slant range line. This first guess is then refined using shadow feature correspondences between the real image and a sequence of simulated images created using refined position estimates.

(2) Extract the shadowed regions in the real image using the histogram technique described in section 3.2.1, and then vectorize the shadow boundaries as described in section 3.2.2.

(3) To find correspondingly shadowed regions, use a hierarchical form of normalized correlation (see section 1.3.3.1) which employs a sequence of matches on a pyramid of reduced resolution versions of the real and synthetic image taken along some assumed approximate flight path. Coarse registration is performed with the coarsest resolution, leading to finer adjustments on higher resolution versions of the imagery (see [Rosenfeld,84]). Such a scheme uses the wider peak properties of the correlation metric to full advantage, since wider peaks allow a wider "pull-in" range for acquisition even when the resolution is degraded.

Such a procedure is much more computationally efficient than exhaustive, high-resolution correlation.

(4) Using the vectorized description of shadow boundaries in real and synthetic images, form the psi-s representation [Ballard,82]. This representation of a curve ideally gives tangent angle as a function of arclength (see section 1.3.3.2)

Because of the differences in shapes between corresponding real and synthetic shadows due to terrain model errors and incorrect platform position estimates, the psi-s matching technique described in section 1.3.3.2 requires good sensor position estimation in order for the corresponding shadows to be similar enough.

Also, the psi-s representation is used to infer corresponding shadow points of high curvature using the derivative of the psi-s representation. In this way, this representation is used as part of an interest operator.

On the near side of the shadow to the sensor, these corresponding points are better matched than on the far side. This is because on the far side, the shadow's movement is much more sensitive to errors in platform position than on the near side where the occluding terrain elements lie.

At this point, it is important to recall that the slant range to ground range transformation of the real SAR image was created assuming the geometry of Fig. 3.2. This transformation was created using the a priori values of sensor height, and range offset. Therefore, whenever updated estimates for these parameters are obtained, they must be used in the creation of a synthetic slant range image. However, the a priori values must be used for the slant to ground range transformation of a synthetic image. Otherwise, a synthetic image could be created from exactly the correct sensor position and still appear slightly different than the real image.

(5) We now seek to find that simulated sensor position p_s that creates slant ranges for p_3 and p_4 which, when projected into a ground range image from p_s , will give the same pixel values for p_3 and p_4 as are found in the real ground range image (see Fig. 3.2 and 3.3).

From p_3 :

$$(x_s - x_3)^2 + (h_s - h_3)^2 = (\dot{g}_{s3} + \dot{g}_{A0})^2 + h_A^2$$

From p_4 :

$$(x_s - x_4)^2 + (h_s - h_4)^2 = (\dot{g}_{s4} + \dot{g}_{A0})^2 + h_A^2$$

want: $\dot{g}_{s3} = \dot{g}_{A3} - \dot{g}_{A0}$

$$\dot{g}_{s4} = \dot{g}_{A4} - \dot{g}_{A0}$$

recall: $\dot{g}_{A3} = m_3 \cdot \Delta g_r + \dot{g}_{A0}$

$$\dot{g}_{A4} = m_4 \cdot \Delta g_r + \dot{g}_{A0}$$

This implies the simultaneous system:

$$(x_s - x_3)^2 + (h_s - h_3)^2 = \dot{g}_{A3}^2 + h_A^2 = c_1$$

$$(x_s - x_4)^2 + (h_s - h_4)^2 = \dot{g}_{A4}^2 + h_A^2 = c_2$$

which is the intersection of 2 circles.

Another issue involves multiple measurements and the distribution of measurements. If at least two range measurements are available per range line, then the flight path is determined for each range line. This, of course, ignores measurement error. If one could assume a perfectly straight and level flight path of known direction then one would only require two range measurements, not necessarily on the same range line. Again measurement error is ignored.

A more realistic scenario would be to assume that the direction of the flight path is known to sufficient accuracy, that the INS positional errors for the imaging period give good relative positional estimates, and that what is required is an offset estimate in crossrange and altitude.

To show how to combine INS measurements and image-derived range measurements under these assumptions, we first demonstrate how to use multiple measurements for estimating a constant horizontal flight path of known orientation. This technique borrows from a method used in sonar [Smith, 87] for locating a source given an over-determined system of simultaneous range measurements. This method will then be generalized for the use of INS measurements.

Let:

\bar{x}_s = sensor position

\bar{x}_i = known DEM locations, $i=1, \dots, N$

$c_i = |\bar{x}_s - \bar{x}_i|$

$\Delta c_{ij} = c_i - c_j$

Using the N geographic DEM points, one can generate an over-determined set of nonlinear equations. However, using range differences and one known range value, one can generate an over-determined set of linear equations.

From the definition of c_i we have:

$$|\bar{x}_s|^2 - 2\bar{x}_s^T \bar{x}_i + |\bar{x}_i|^2 = c_i^2$$

Now let:

$$r_s = |\bar{x}_s|$$

$$r_i = |\bar{x}_i|$$

Using these definitions and that for Δc_{ij} , and letting one of the \bar{x}_i be the origin, we have for $i=2, \dots, N$

$$(r_s + \Delta c_{i1})^2 = r_i^2 - 2\bar{x}_i^T \bar{x}_s + r_s^2$$

This implies:

$$0 = r_i^2 - \Delta c_{i1}^2 - 2r_s \Delta c_{i1} - 2\bar{x}_i^T \bar{x}_s \quad i = 2, \dots, N$$

Note that the unknown sensor position \bar{x}_s now enters linearly into this system of equations, even though range is a

nonlinear function of \bar{x}_s .

Let ε_i = "equation error" for i^{th} equation, then:

$$\varepsilon_i = r_i^2 - \Delta c_{i1}^2 - 2r_s \Delta c_{i1} - 2\bar{x}_i^T \bar{x}_s \quad i = 2, \dots, N$$

Using vector and matrix notation, this system of equations can now be summarized:

$$\bar{\epsilon} = \bar{v} - 2r_s \bar{\Delta c} - 2M\bar{x}_s$$

where:

$$\bar{\epsilon} = (\epsilon_1, \dots, \epsilon_N)^T$$

$$\bar{v} = (r_1^2 - \Delta c_{11}^2, \dots, r_N^2 - \Delta c_{N1}^2)^T$$

$$M = \begin{bmatrix} x_1 & z_1 \\ \vdots & \vdots \\ \vdots & \vdots \\ x_N & z_N \end{bmatrix}$$

$$\bar{\Delta c} = (\Delta c_{11}, \dots, \Delta c_{N1})^T$$

This over-determined system can be solved to yield the minimum least squares value for

$\bar{\epsilon}^T \bar{\epsilon}$ by the use of the generalized inverse:

$$\bar{x}_s = 1/2 (M^T M)^{-1} M^T (\bar{v} - 2r_s \bar{\Delta c})$$

Such an expression can even be generalized to include a weighting matrix W for the measurements:

$$\bar{x}_s = 1/2 (M^T W M)^{-1} M^T W (\bar{v} - 2r_s \bar{\Delta c})$$

Now, we generalize this result to incorporate the use of INS measurements and we again assume that what is required is an offset estimate in cross range and altitude.

Let:

$\{t_i\}$ be the time points corresponding to a range measurement with respect to an identified DEM position.

$\{\bar{p}(t_i)\}$ be the set of INS measurements for the time points $\{t_i\}$ $i = 1, \dots, N$

\bar{x}_o be the desired INS offset

Then make the modified definition:

$$c_i = |\bar{p}(t_i) - (\bar{x}_o - \bar{x}_i)|$$

$$\text{but } c_i = |\bar{x}_o - (\bar{x}_i - \bar{p}(t_i))|$$

Therefore, one can use the previous generalized inverse solution to obtain the INS offset but with the

\bar{x}_i replaced by $(\bar{x}_i - \bar{p}(t_i))$

Of course, another smaller error will occur because the association between image and model points is dependent on occluding points for shadows. If the sensor position changes, the position of occluding points changes slightly. However, this is a second-order effect, and will be ignored because the process will be repeated by iteration for the new estimated sensor position P' .

(6) Using the newer approximation for the flight path, iteration can now be performed on the previous steps. The convergence should be rapid.

Of course, the problem of resection for any sensor is ill-conditioned if the control points are not well-distributed. For the case of SAR, some examples are given in Fig. 3.42 - 3.45 for the variation in the location of the intersection of two range circles as a function of perturbations of the center separations.

Another relevant problem is the degree of precision required for the DEM to achieve a given accuracy for shadow matching. Some numerical results on this issue are shown in Fig. 3.46 - 3.49.

3.2.2.2 Results

In order to test some of the concepts in the previous section, one test that was performed was to vary the assumed altitude of the flight path (assuming that the flight path is a straight, horizontal line) and create synthetic images corresponding to these offsets. The real SAR image is in Fig. 3.4. Synthetic images for a number of different altitudes, but correct ground range offsets, are shown in Fig. 3.11 - 3.17.

The use of normalized correlation metric for acquisition matching of shadowed regions is shown in Fig. 3.18 - 3.24. A large window was picked out in the real image which contained a shadow. This was established using the thresholding in step (1) of the algorithm. Because of an initial positional approximation available from the INS, it is possible to select a small region within the simulated images which will be known to be within this larger region in the real image. Then, the normalized correlation metric was used to find that patch within the real image which corresponded to each of these patches in the synthetic images corresponding to the different flight altitudes. The best match was achieved using a hypothesized value of 10.0 km.

The use of the sum of differences metric for matching shadowed regions is shown in Fig. 3.25 - 3.29. The same procedure was employed as for the images in Fig. 3.18 - 3.24.

The vectorized shadow boundaries corresponding to different flight altitudes are shown in Fig. 3.31 - 3.37.

The computed flight path altitude, for which the best match using the normalized correlation metric was achieved, was 10.0 km. This agrees with the flight log. Fig. 3.41 shows the values of the metrics used, i.e. normalized correlation and sum of differences, on both intensity and binarized images.

Fig. 3.38 shows a windowed area containing shadows used for the correlations, along with the points identified from their high curvature in their psi-s representation. The same is shown in the corresponding synthetic image shown in Fig. 3-39. Finally, Fig. 3-40 shows the correspondences formed between these identifiable points in the real and synthetic images. These corresponding points are used to implement steps (5) and (6) of the algorithm described in the previous section.

The particular SAR image shown in Fig. 3.4 has its radar shadows clustered together in the range direction since the single mountain range in the field of view is roughly parallel to the flight path. Therefore, using shadows alone in this case will lead to ill-conditioned resection unless other control information is used that is more spread out in the range direction. In general, various combinations of control information from both terrain and features will be required to form well-conditioned resections.

3.2.3 Analysis of Robustness

Using the previous imagery and the positional acquisition technique described above, several initial estimates for offset were attempted. The limits on initial errors are discussed below.

In one case, the correct sensor position was about 10 km. in altitude, and 14 km. in range to near range offset. The correlation/matching technique failed at initial estimates for altitude in excess of 12 km. and lower than 7.5 km., ie. for about a 25% relative error.

In another case, where the correct ground range offset was 9.76 km., all initial estimates within 5 km. to 20 km. converged to the correct solution. These two upper and lower values represent only the limits of testing.

Azimuthal offsets of up to 27 km. were tested, and convergence occurred in all cases.

Clearly, the above comments only represent empirical results using a small data set. A more complete analytical analysis must be performed to better understand the robustness of these procedures.

3.3 Use of Terrain-Induced Shading for Control

The use of shading information in a real and synthetic optical image for registration of image and terrain model has been done previously [Horn,78]. However, the transformation that was sought was not a perspective, but just a global rotation and translation since the imaging scenario was orthographic projection.

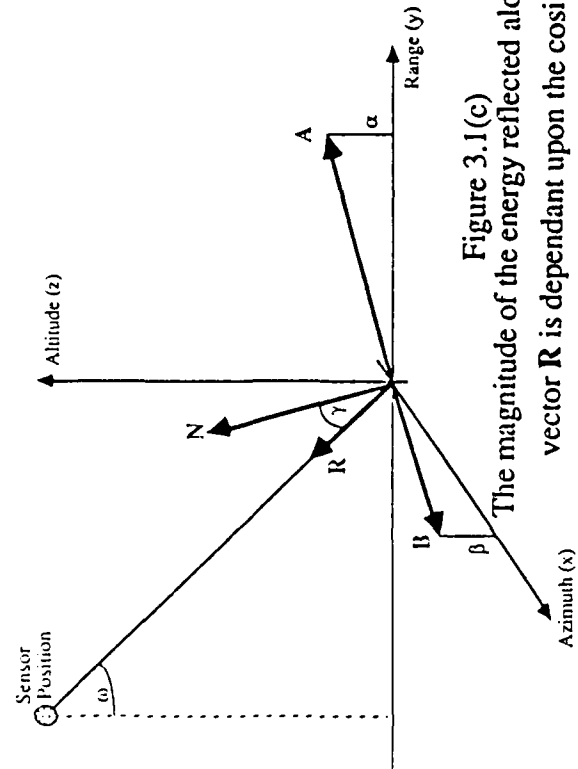
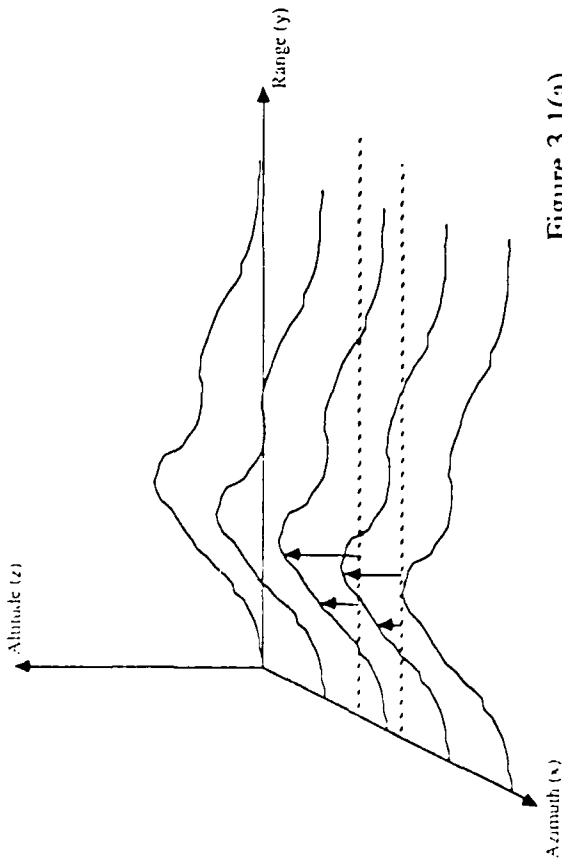
The use of SAR imagery presents some differences from the case reported in [Horn,78]. SAR imagery has more artifacts such as noise and speckle than optical imagery, and radar backscatter has a more directional dependency. Also, SAR imagery is side-looking rather than down-looking.

However, the above approach can still be used for selected regions in the SAR case with some modification. Step (2) of the algorithm in the previous section 3.2.2 used region-based correlation to approximately identify corresponding shadowed regions previously extracted in step (1). By using the model, an algorithm could select other favorable terrain for matching. This is an example of "model-based" matching.

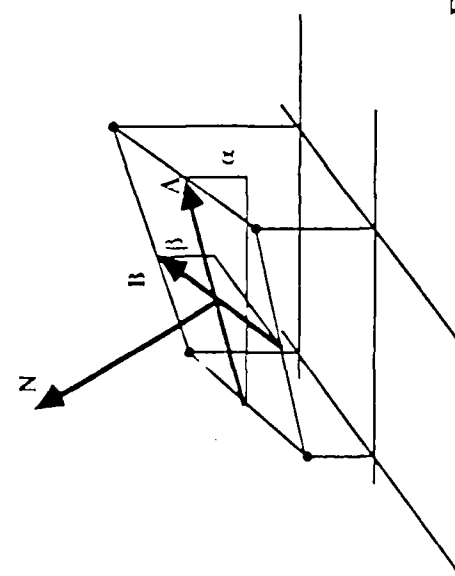
For example, fairly level regions which are near the tops of elevated terrain would not cause range compression, and may have good contrast with possible shadows on the other side of the crest.

Some local histogram re-mapping may also be useful when matching candidate regions to reduce the effect of variations in scattering cross sections.

This approach may also be investigated in the subsequent Options.



46



$$\begin{aligned}
 \mathbf{N} &= \text{surface normal} & \mathbf{A} \times \mathbf{B} &= -\alpha \mathbf{a}_x - \beta \mathbf{a}_y + \mathbf{a}_z \\
 \mathbf{R} &= \text{unit range vector} & &= -\sin \omega \mathbf{a}_y + \cos \omega \mathbf{a}_z \\
 \mathbf{N} \cdot \mathbf{R} &= |\mathbf{N}| |\mathbf{R}| \cos(\gamma) \\
 \text{reflected energy} &= \frac{\mathbf{N} \cdot \mathbf{R}}{(|\mathbf{N}| |\mathbf{R}|)} = \frac{\beta \sin \omega + \cos \omega}{\sqrt{\alpha^2 + \beta^2 + 1}}
 \end{aligned}$$

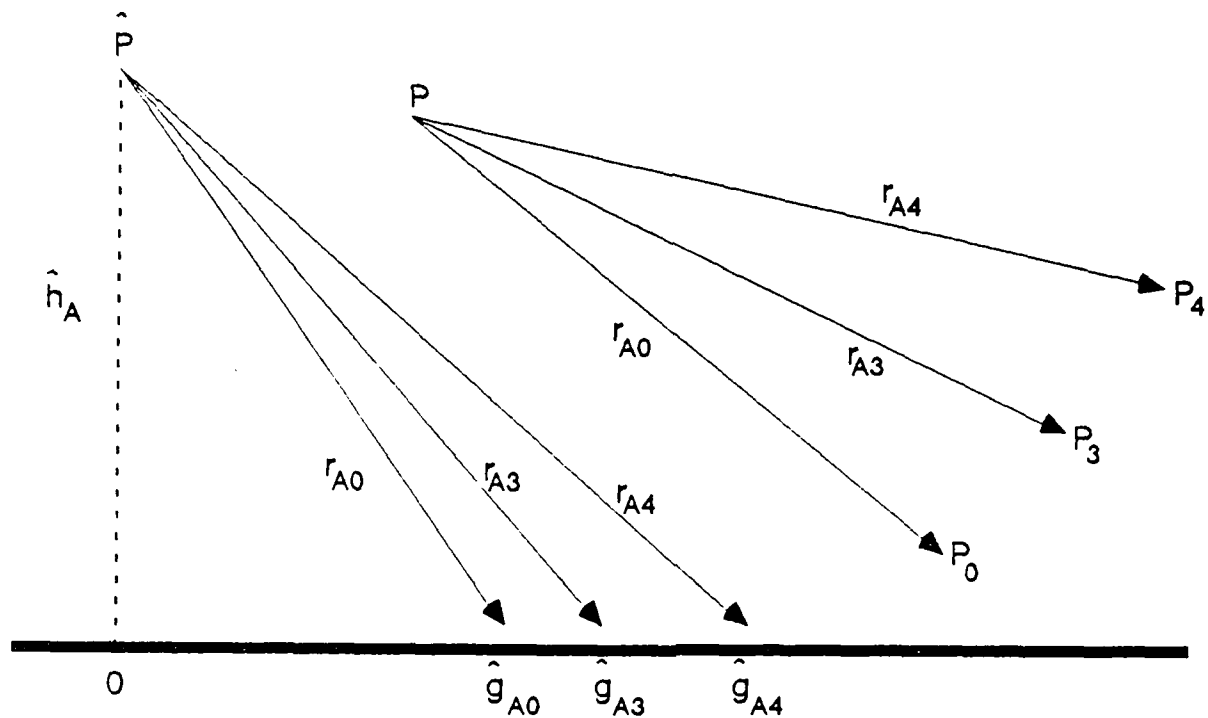


Figure 3.2
The Actual Imaging Scenario

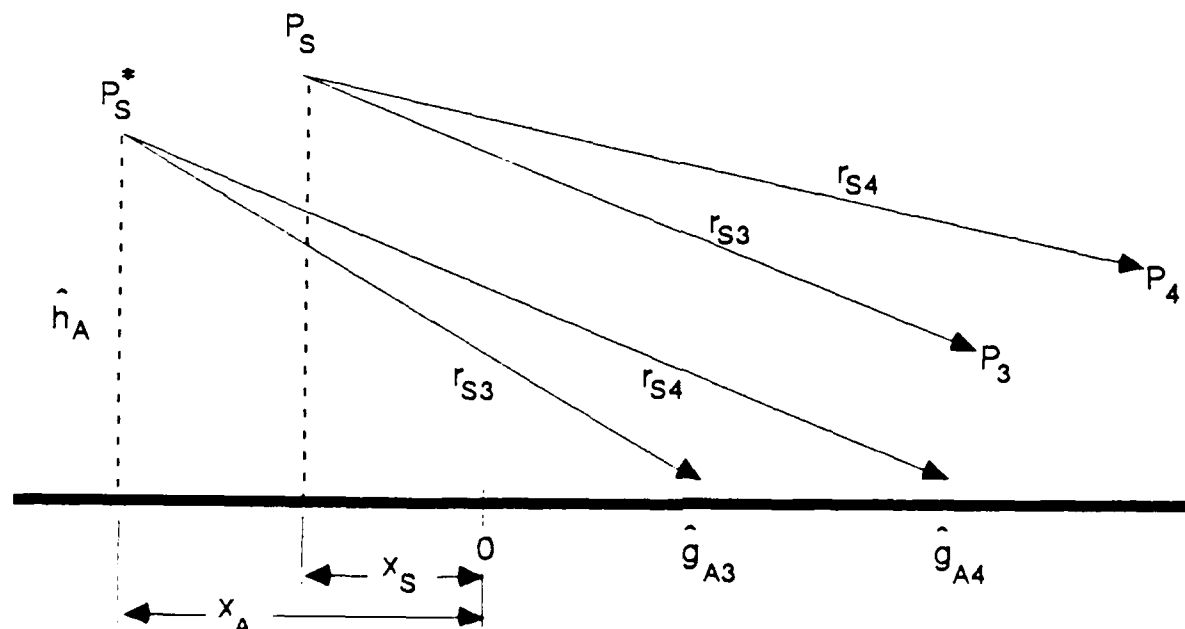
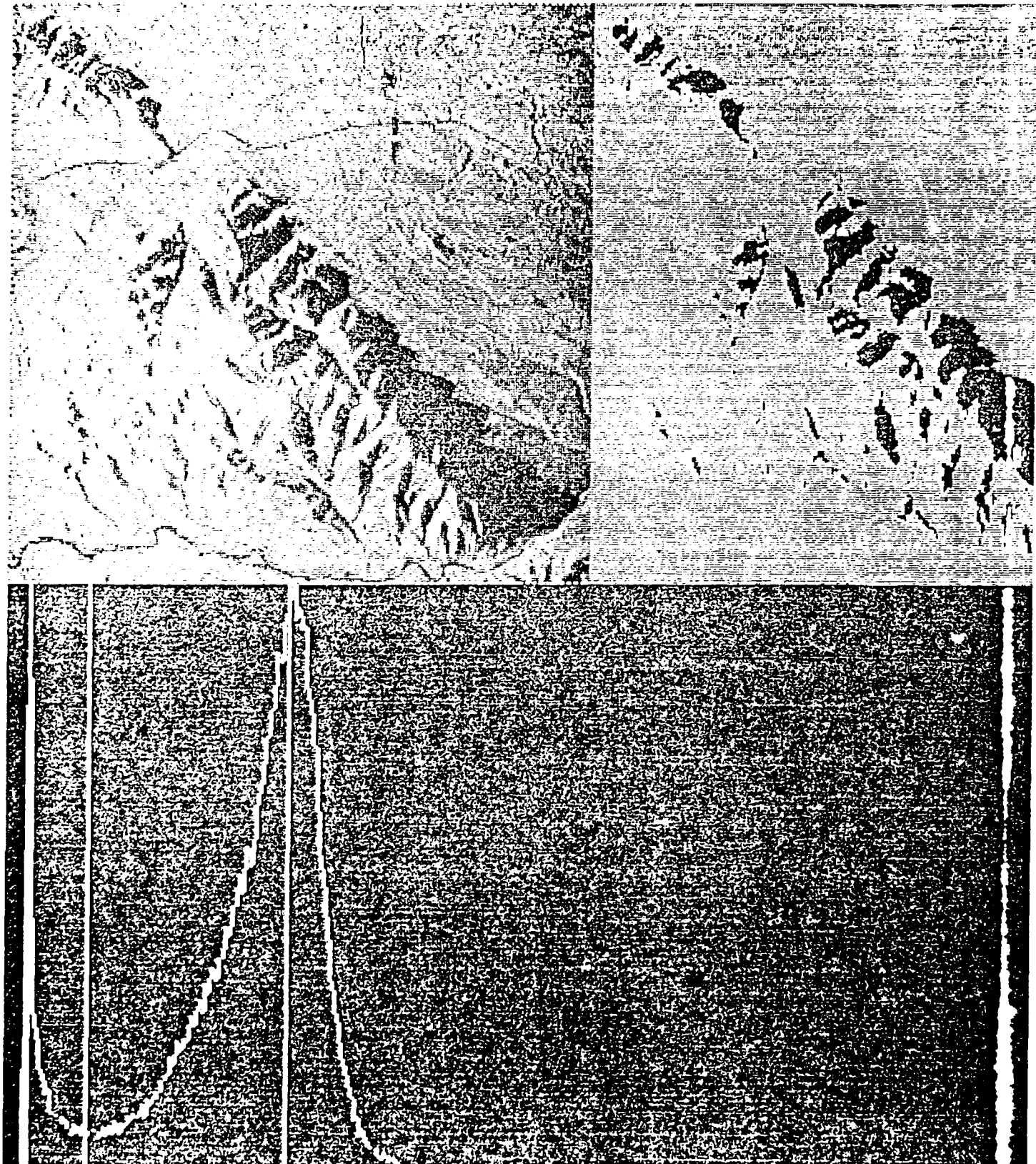


Figure 3.3
The Simulated Imaging Scenario





1990-1991

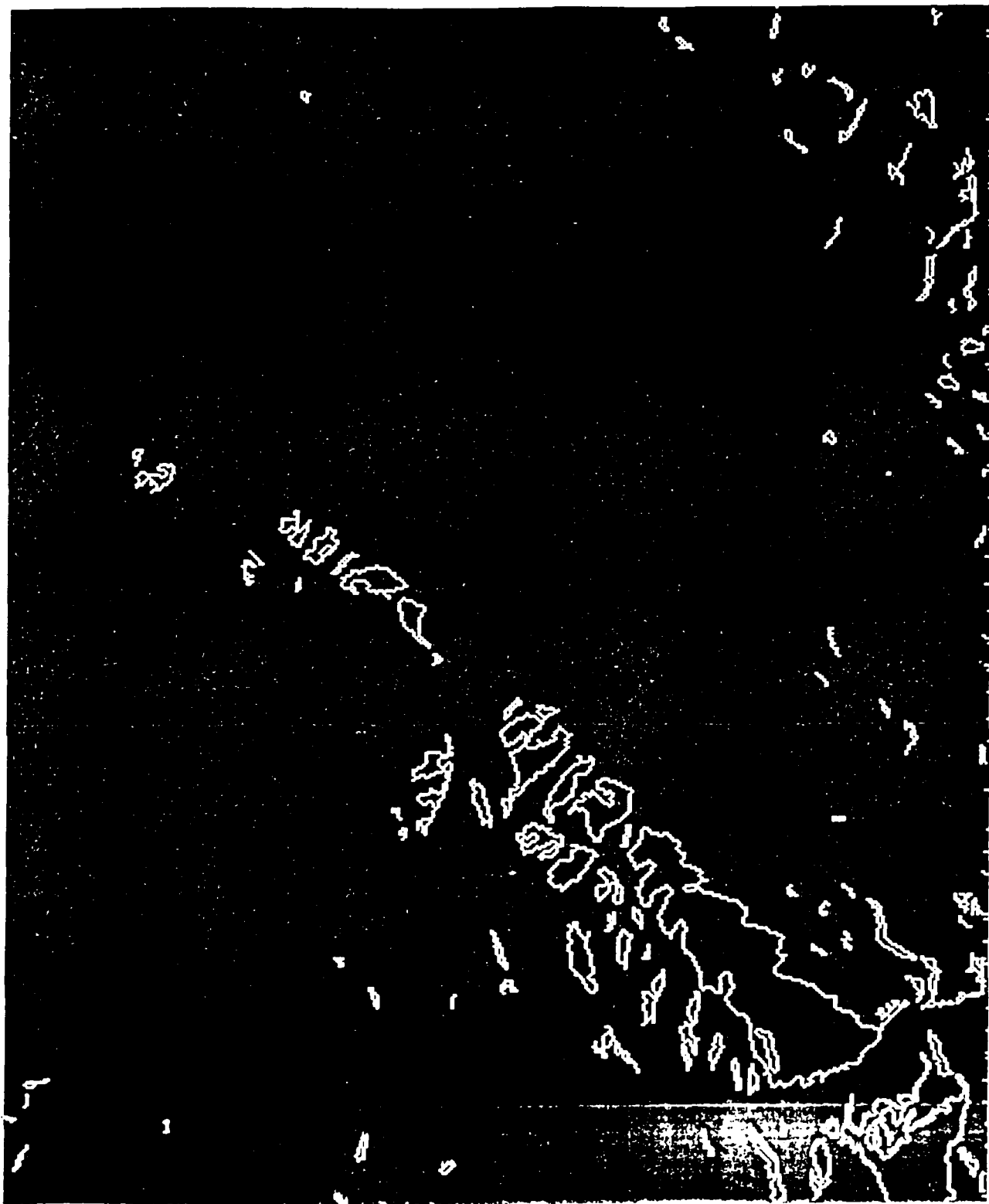


Vectorized Shadow Boundaries of SAR image, Brazeau Range Area

Minimum contour length: 10 pixels

Threshold for shadow boundaries: 46

Figure 3.6

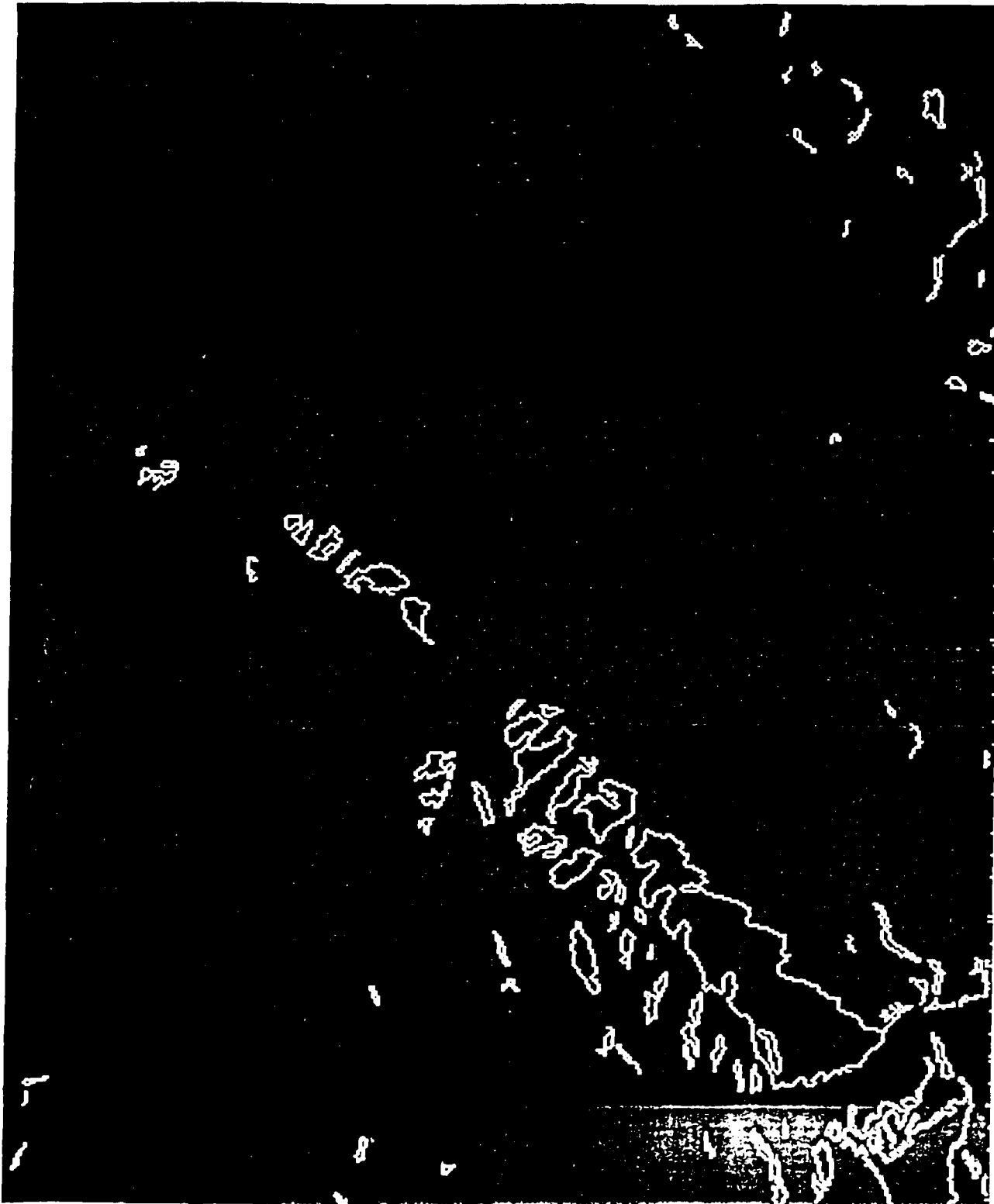


Vectorized Shadow Boundaries of SAR Image, Bruneau Range Area

Minimum contour length: 10 pixels

Threshold for shadow boundaries: 13

Figure 3.7

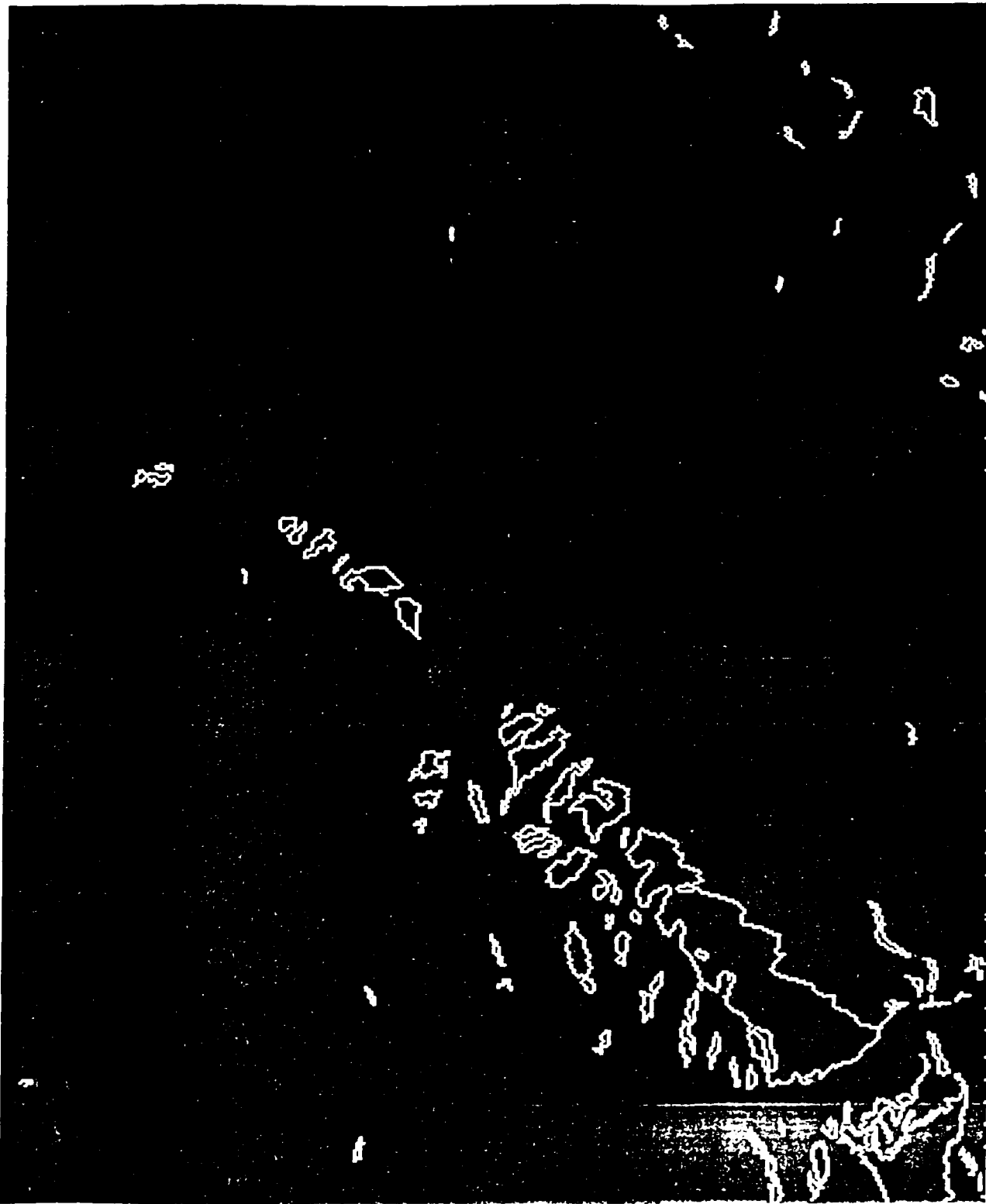


Vectorized Shadow Boundaries of SAB image, Bristow Range Area

Minimum contour length: 10 pixels

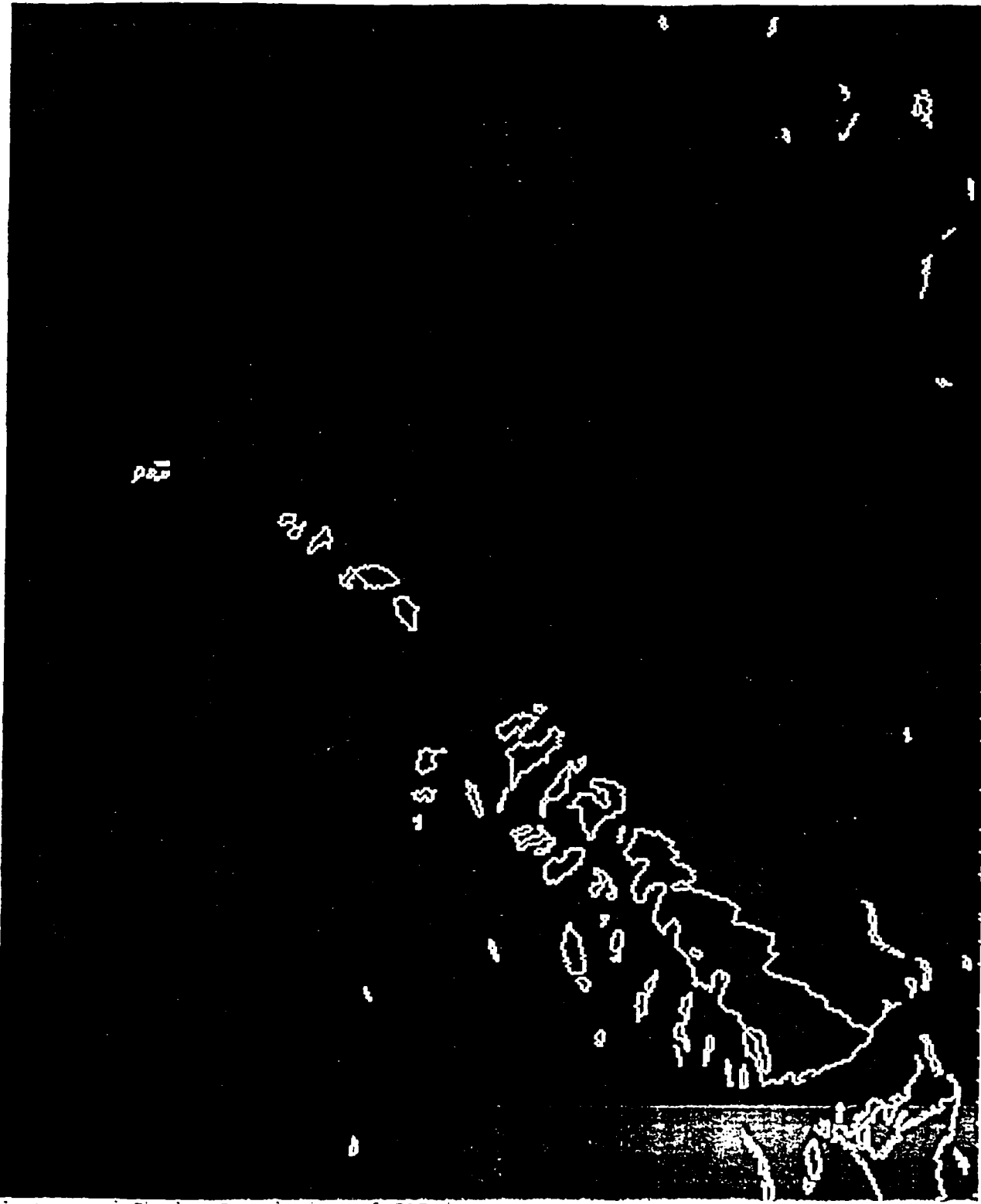
Threshold for shadow boundaries: 37

Figure 3.3



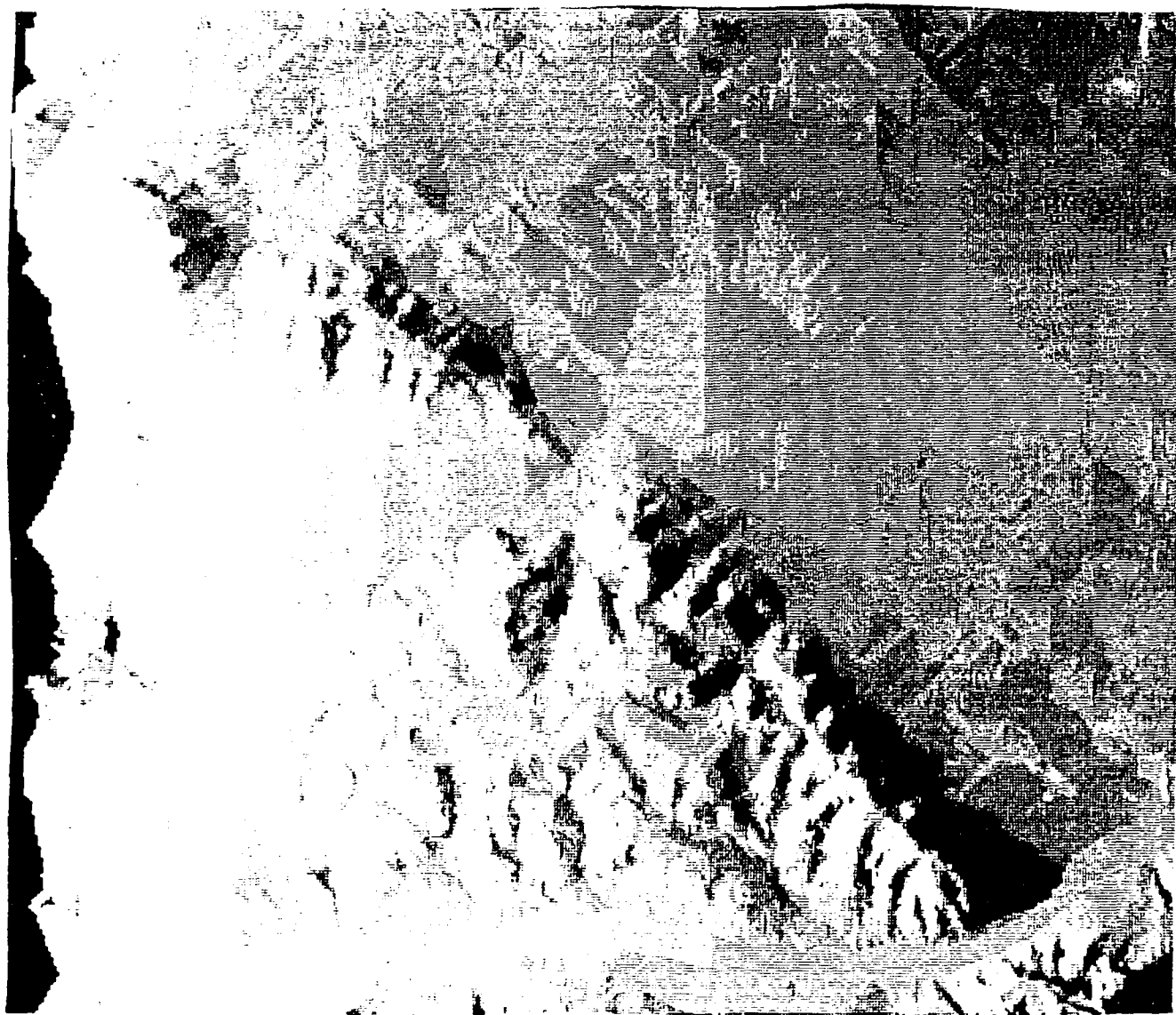
Vectorized Shadow Boundaries of SAR image, Brazeau Range Area
Minimum contour length: 10 pixels
Threshold for shadow boundaries: 32

Figure 3.3

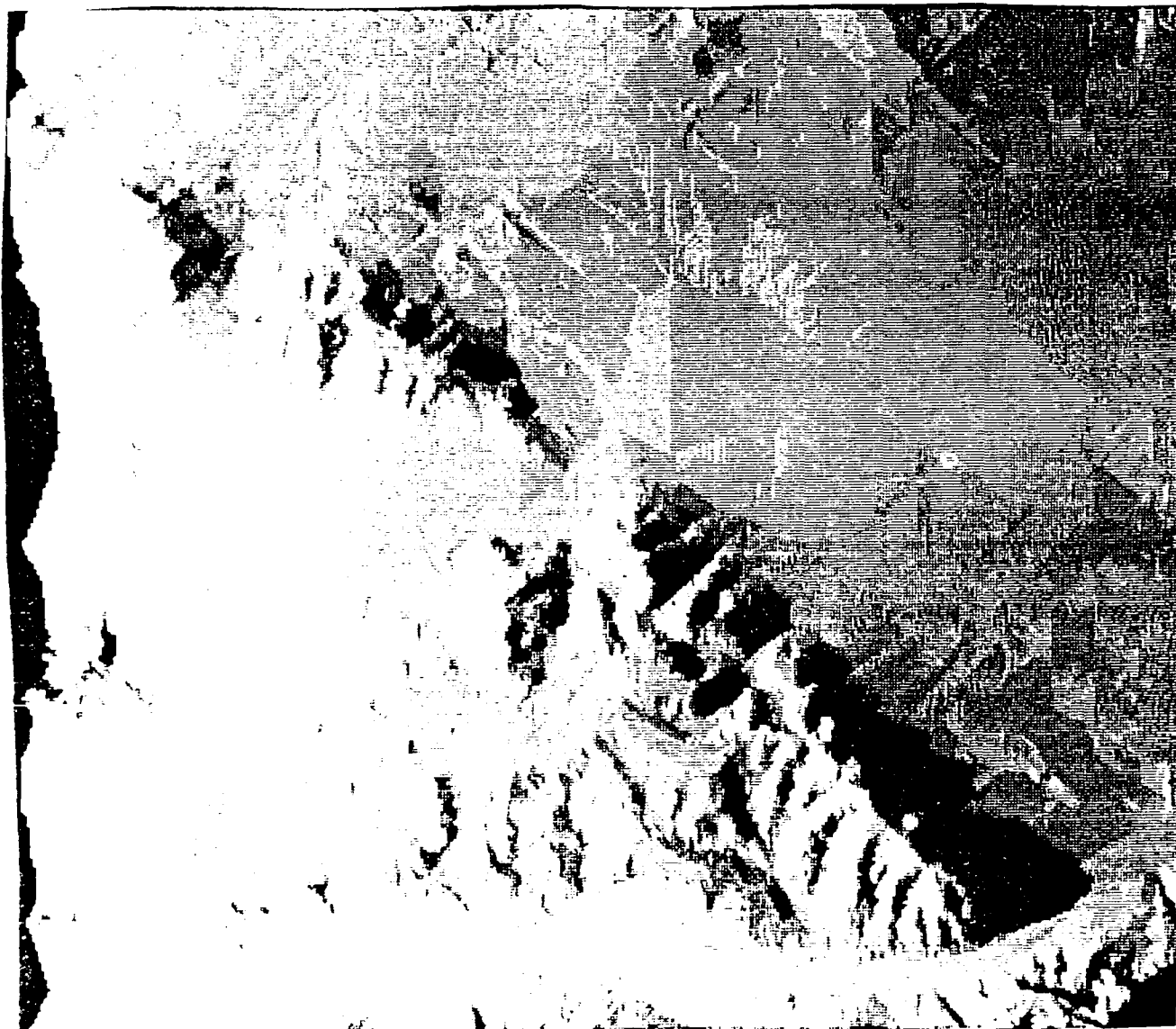


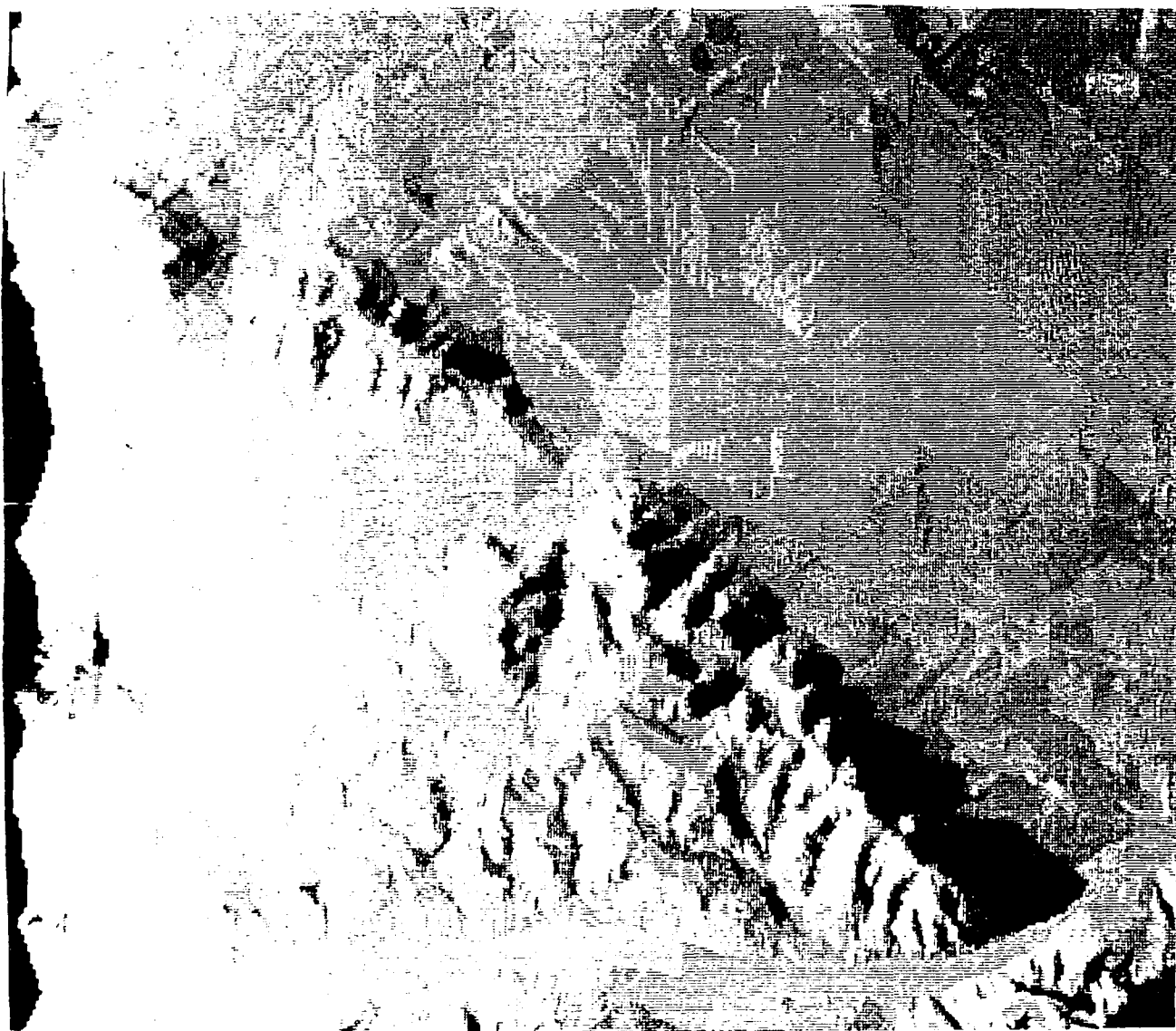
Vectorized Shadow Boundaries of SAR image, Brazeau Range Area
Minimum contour length: 10 pixels
Threshold for shadow boundaries: 35

Figure 3.10



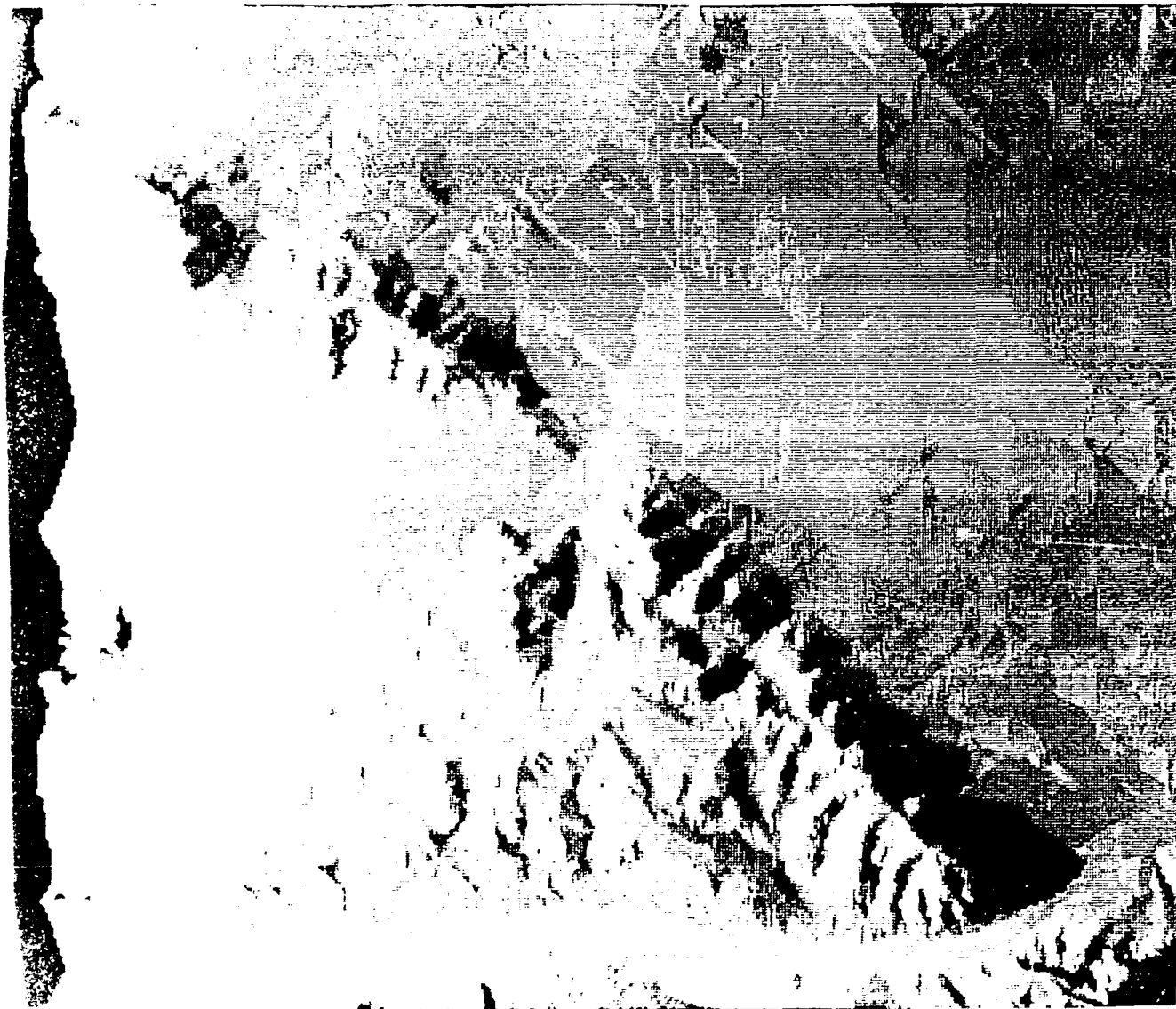
1960-1961
1961-1962
1962-1963
1963-1964
1964-1965
1965-1966
1966-1967
1967-1968
1968-1969
1969-1970
1970-1971
1971-1972
1972-1973
1973-1974
1974-1975
1975-1976
1976-1977
1977-1978
1978-1979
1979-1980
1980-1981
1981-1982
1982-1983
1983-1984
1984-1985
1985-1986
1986-1987
1987-1988
1988-1989
1989-1990
1990-1991
1991-1992
1992-1993
1993-1994
1994-1995
1995-1996
1996-1997
1997-1998
1998-1999
1999-2000
2000-2001
2001-2002
2002-2003
2003-2004
2004-2005
2005-2006
2006-2007
2007-2008
2008-2009
2009-2010
2010-2011
2011-2012
2012-2013
2013-2014
2014-2015
2015-2016
2016-2017
2017-2018
2018-2019
2019-2020
2020-2021
2021-2022
2022-2023
2023-2024
2024-2025
2025-2026
2026-2027
2027-2028
2028-2029
2029-2030
2030-2031
2031-2032
2032-2033
2033-2034
2034-2035
2035-2036
2036-2037
2037-2038
2038-2039
2039-2040
2040-2041
2041-2042
2042-2043
2043-2044
2044-2045
2045-2046
2046-2047
2047-2048
2048-2049
2049-2050
2050-2051
2051-2052
2052-2053
2053-2054
2054-2055
2055-2056
2056-2057
2057-2058
2058-2059
2059-2060
2060-2061
2061-2062
2062-2063
2063-2064
2064-2065
2065-2066
2066-2067
2067-2068
2068-2069
2069-2070
2070-2071
2071-2072
2072-2073
2073-2074
2074-2075
2075-2076
2076-2077
2077-2078
2078-2079
2079-2080
2080-2081
2081-2082
2082-2083
2083-2084
2084-2085
2085-2086
2086-2087
2087-2088
2088-2089
2089-2090
2090-2091
2091-2092
2092-2093
2093-2094
2094-2095
2095-2096
2096-2097
2097-2098
2098-2099
2099-20100
20100-20101
20101-20102
20102-20103
20103-20104
20104-20105
20105-20106
20106-20107
20107-20108
20108-20109
20109-20110
20110-20111
20111-20112
20112-20113
20113-20114
20114-20115
20115-20116
20116-20117
20117-20118
20118-20119
20119-20120
20120-20121
20121-20122
20122-20123
20123-20124
20124-20125
20125-20126
20126-20127
20127-20128
20128-20129
20129-20130
20130-20131
20131-20132
20132-20133
20133-20134
20134-20135
20135-20136
20136-20137
20137-20138
20138-20139
20139-20140
20140-20141
20141-20142
20142-20143
20143-20144
20144-20145
20145-20146
20146-20147
20147-20148
20148-20149
20149-20150
20150-20151
20151-20152
20152-20153
20153-20154
20154-20155
20155-20156
20156-20157
20157-20158
20158-20159
20159-20160
20160-20161
20161-20162
20162-20163
20163-20164
20164-20165
20165-20166
20166-20167
20167-20168
20168-20169
20169-20170
20170-20171
20171-20172
20172-20173
20173-20174
20174-20175
20175-20176
20176-20177
20177-20178
20178-20179
20179-20180
20180-20181
20181-20182
20182-20183
20183-20184
20184-20185
20185-20186
20186-20187
20187-20188
20188-20189
20189-20190
20190-20191
20191-20192
20192-20193
20193-20194
20194-20195
20195-20196
20196-20197
20197-20198
20198-20199
20199-20200
20200-20201
20201-20202
20202-20203
20203-20204
20204-20205
20205-20206
20206-20207
20207-20208
20208-20209
20209-20210
20210-20211
20211-20212
20212-20213
20213-20214
20214-20215
20215-20216
20216-20217
20217-20218
20218-20219
20219-20220
20220-20221
20221-20222
20222-20223
20223-20224
20224-20225
20225-20226
20226-20227
20227-20228
20228-20229
20229-20230
20230-20231
20231-20232
20232-20233
20233-20234
20234-20235
20235-20236
20236-20237
20237-20238
20238-20239
20239-20240
20240-20241
20241-20242
20242-20243
20243-20244
20244-20245
20245-20246
20246-20247
20247-20248
20248-20249
20249-20250
20250-20251
20251-20252
20252-20253
20253-20254
20254-20255
20255-20256
20256-20257
20257-20258
20258-20259
20259-20260
20260-20261
20261-20262
20262-20263
20263-20264
20264-20265
20265-20266
20266-20267
20267-20268
20268-20269
20269-20270
20270-20271
20271-20272
20272-20273
20273-20274
20274-20275
20275-20276
20276-20277
20277-20278
20278-20279
20279-20280
20280-20281
20281-20282
20282-20283
20283-20284
20284-20285
20285-20286
20286-20287
20287-20288
20288-20289
20289-20290
20290-20291
20291-20292
20292-20293
20293-20294
20294-20295
20295-20296
20296-20297
20297-20298
20298-20299
20299-202100
202100-202101
202101-202102
202102-202103
202103-202104
202104-202105
202105-202106
202106-202107
202107-202108
202108-202109
202109-202110
202110-202111
202111-202112
202112-202113
202113-202114
202114-202115
202115-202116
202116-202117
202117-202118
202118-202119
202119-202120
202120-202121
202121-202122
202122-202123
202123-202124
202124-202125
202125-202126
202126-202127
202127-202128
202128-202129
202129-202130
202130-202131
202131-202132
202132-202133
202133-202134
202134-202135
202135-202136
202136-202137
202137-202138
202138-202139
202139-202140
202140-202141
202141-202142
202142-202143
202143-202144
202144-202145
202145-202146
202146-202147
202147-202148
202148-202149
202149-202150
202150-202151
202151-202152
202152-202153
202153-202154
202154-202155
202155-202156
202156-202157
202157-202158
202158-202159
202159-202160
202160-202161
202161-202162
202162-202163
202163-202164
202164-202165
202165-202166
202166-202167
202167-202168
202168-202169
202169-202170
202170-202171
202171-202172
202172-202173
202173-202174
202174-202175
202175-202176
202176-202177
202177-202178
202178-202179
202179-202180
202180-202181
202181-202182
202182-202183
202183-202184
202184-202185
202185-202186
202186-202187
202187-202188
202188-202189
202189-202190
202190-202191
202191-202192
202192-202193
202193-202194
202194-202195
202195-202196
202196-202197
202197-202198
202198-202199
202199-202200
202200-202201
202201-202202
202202-202203
202203-202204
202204-202205
202205-202206
202206-202207
202207-202208
202208-202209
202209-202210
202210-202211
202211-202212
202212-202213
202213-202214
202214-202215
202215-202216
202216-202217
202217-202218
202218-202219
202219-202220
202220-202221
202221-202222
202222-202223
202223-202224
202224-202225
202225-202226
202226-202227
202227-202228
202228-202229
202229-202230
202230-202231
202231-202232
202232-202233
202233-202234
202234-202235
202235-202236
202236-202237
202237-202238
202238-202239
202239-202240
202240-202241
202241-202242
202242-202243
202243-202244
202244-202245
202245-202246
202246-202247
202247-202248
202248-202249
202249-202250
202250-202251
202251-202252
202252-202253
202253-202254
202254-202255
202255-202256
202256-202257
202257-202258
202258-202259
202259-202260
202260-202261
202261-202262
202262-202263
202263-202264
202264-202265
202265-202266
202266-202267
202267-202268
202268-202269
202269-202270
202270-202271
202271-202272
202272-202273
202273-202274
202274-202275
202275-202276
202276-202277
202277-202278
202278-202279
202279-202280
202280-202281
202281-202282
202282-202283
202283-202284
202284-202285
202285-202286
202286-202287
202287-202288
202288-202289
202289-202290
202290-202291
202291-202292
202292-202293
202293-202294
202294-202295
202295-202296
202296-202297
202297-202298
202298-202299
202299-202300
202300-202301
202301-202302
202302-202303
202303-202304
202304-202305
202305-202306
202306-202307
202307-202308
202308-202309
202309-202310
202310-202311
202311-202312
202312-202313
202313-202314
202314-202315
202315-202316
202316-202317
202317-202318
202318-202319
202319-202320
202320-202321
202321-202322
202322-202323
202323-202324
202324-202325
202325-202326
202326-202327
202327-202328
202328-202329
202329-202330
202330-202331
202331-202332
202332-202333
202333-202334
202334-202335
202335-202336
202336-202337
202337-202338
202338-202339
202339-202340
202340-202341
202341-202342
202342-202343
202343-202344
202344-202345
202345-202346
202346-202347
202347-202348
202348-202349
202349-202350
202350-202351
202351-202352
202352-202353
202353-202354
202354-202355
202355-202356
202356-202357
202357-202358
202358-202359
202359-202360
202360-202361
202361-202362
202362-202363
202363-202364
202364-202365
202365-202366
202366-202367
202367-202368
202368-202369
202369-202370
202370-202371
202371-202372
202372-202373
202373-202374
202374-202375
202375-202376
202376-202377
202377-202378
202378-202379
202379-202380
202380-202381
202381-202382
202382-202383
202383-202384
202384-202385
202385-202386
202386-202387
202387-202388
202388-202389
202389-202390
202390-202391
202391-202392
202392-202393
202393-202394
202394-202395
202395-202396
202396-202397
202397-202398
202398-202399
202399-202400
202400-202401
202401-202402
202402-202403
202403-202404
202404-202405
202405-202406
202406-202407
202407-202408
202408-202409
202409-202410
202410-202411
202411-202412
202412-202413
202413-202414
202414-202415
202415-202416
202416-202417
202417-202418
202418-202419
202419-202420
202420-202421
202421-202422
202422-202423
202423-202424
202424-202425
202425-202426
202426-202427
202427-202428
202428-202429
202429-202430
202430-202431
202431-202432
202432-202433
202433-202434
202434-202435
202435-202436
202436-202437
202437-202438
202438-202439
202439-202440
202440-202441
202441-202442
202442-202443
202443-202444
202444-202445
202445-202446
202446-202447
202447-202448
202448-202449
202449-202450
202450-202451
202451-202452
202452-202453
202453-202454
202454-202455
202455-202456
202456-202457
202457-202458
202458-202459
202459-202460
202460-202461
202461-202462
202462-202463
202463-202464
202464-202465
202465-202466
202466-202467
202467-202468
202468-202469
202469-202470
202470-202471
202471-202472
202472-202473
202473-202474
202474-202475
202475-202476
202476-202477
202477-202478
202478-202479
202479-202480
202480-202481
202481-202482
202482-202483
202483-202484
202484-202485
202485-202486
202486-202487
202487-202488
202488-202489
202489-202490
202490-202491
202491-202492
202492-202493
202493-202494
202494-202495
202495-202496
202496-202497
202497-202498
202498-202499
202499-202500
202500-202501
202501-202502
202502-202503
202503-202504
202504-202505
202505-202506
202506-202507
202507-202508
202508-202509
202509-202510
202510-202511
202511-202512
202512-202513
202513-202514
202514-202515
202515-202516
202516-202517
202517-202518
202518-202519
202519-202520
202520-202521
202521-202522
202522-202523
202523-202524
202524-202525
202525-202526
202526-202527
202527-202528
202528-202529
202529-202530
202530-202531
202531-202532
202532-202533
202533-202534
202534-202535
202535-202536
202536-202537
202537-202538
202538-202539
202539-202540
202540-202541
202541-202542
202542-202543
202543-202544
202544-202545
202545-202546
202546-202547
202547-202548
202548-202549
202549-202550
202550-202551
202551-202552
202552-202553
202553-202554
202554-202555
202555-202556
202556-202557
202557-202558
202558-202559
202559-202560
202560-202561
202561-202562
202562-202563
202563-20256

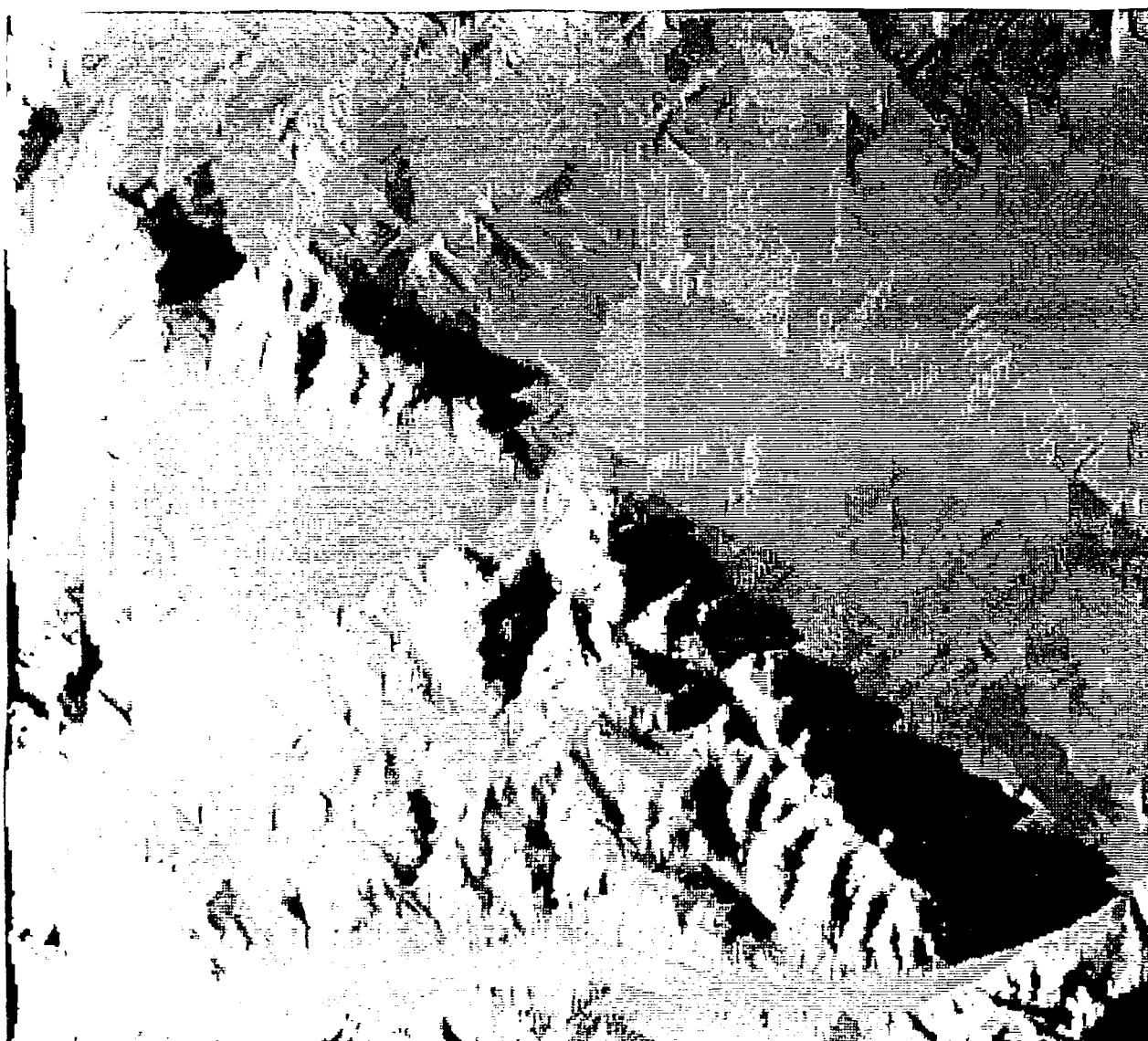


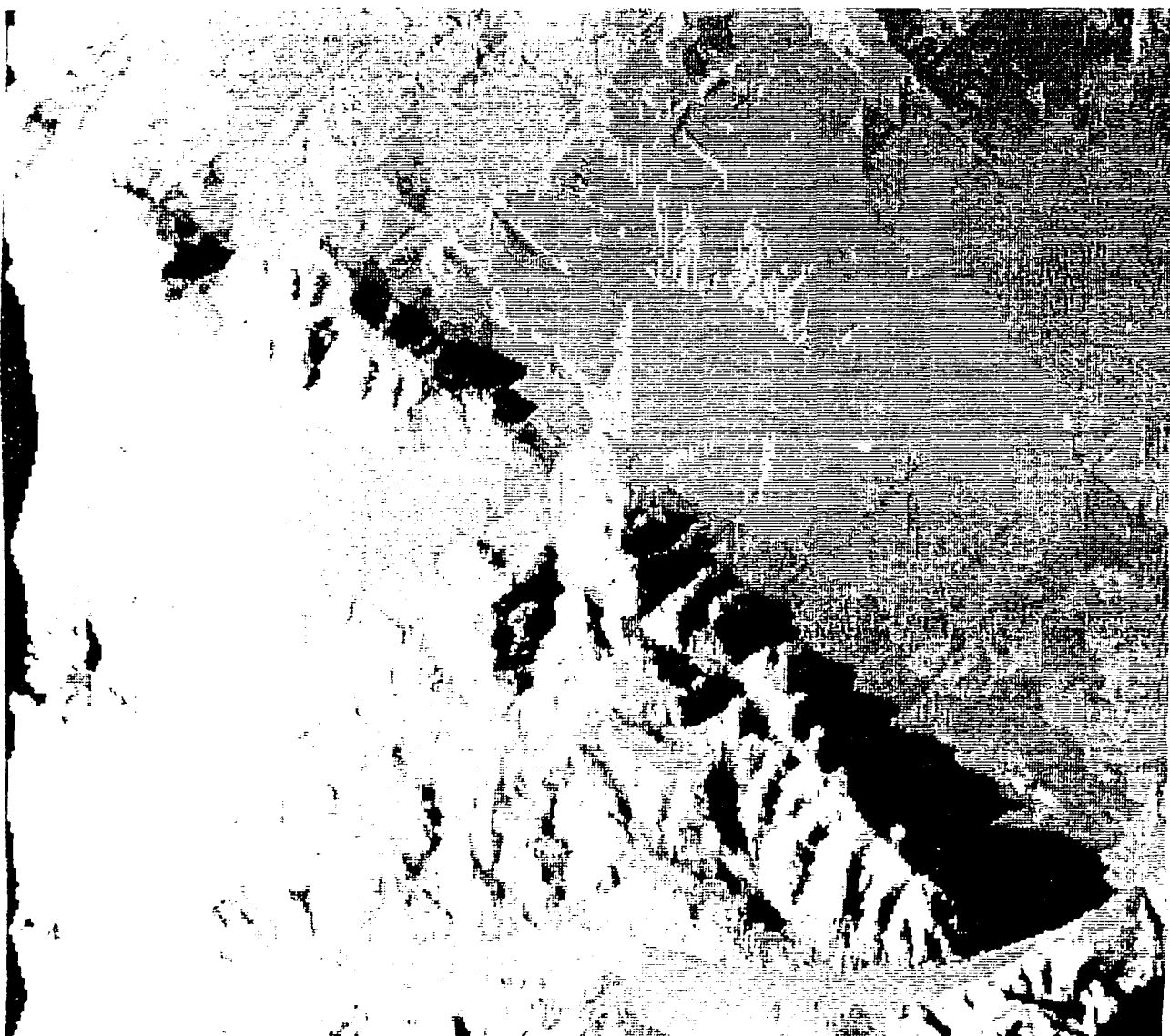


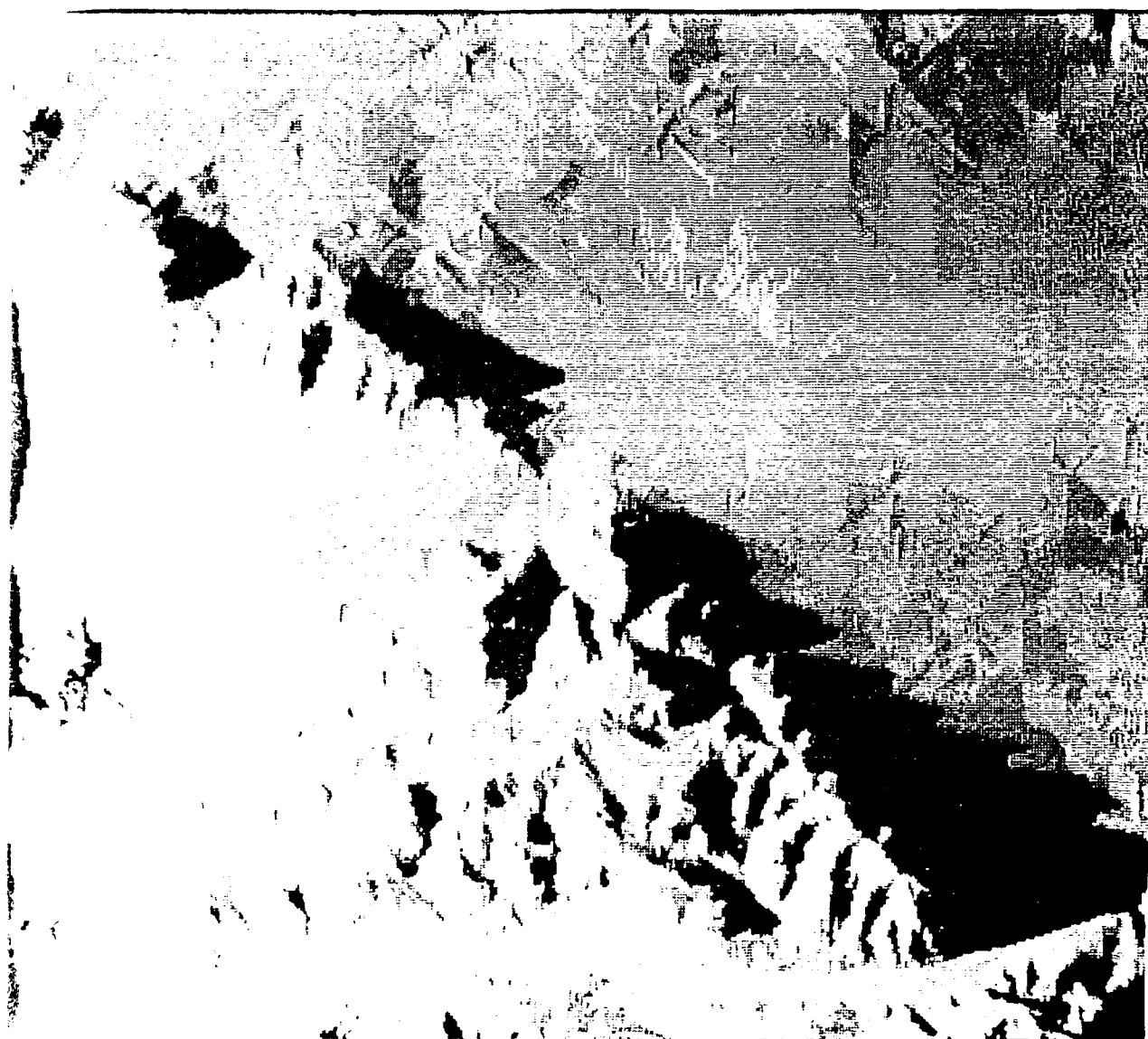
1. *Acta Cryst. B* 1973, **30**, 1000-1002
© 1973 International Union of Crystallography

2. *Acta Cryst. B* 1973, **30**, 1003-1005

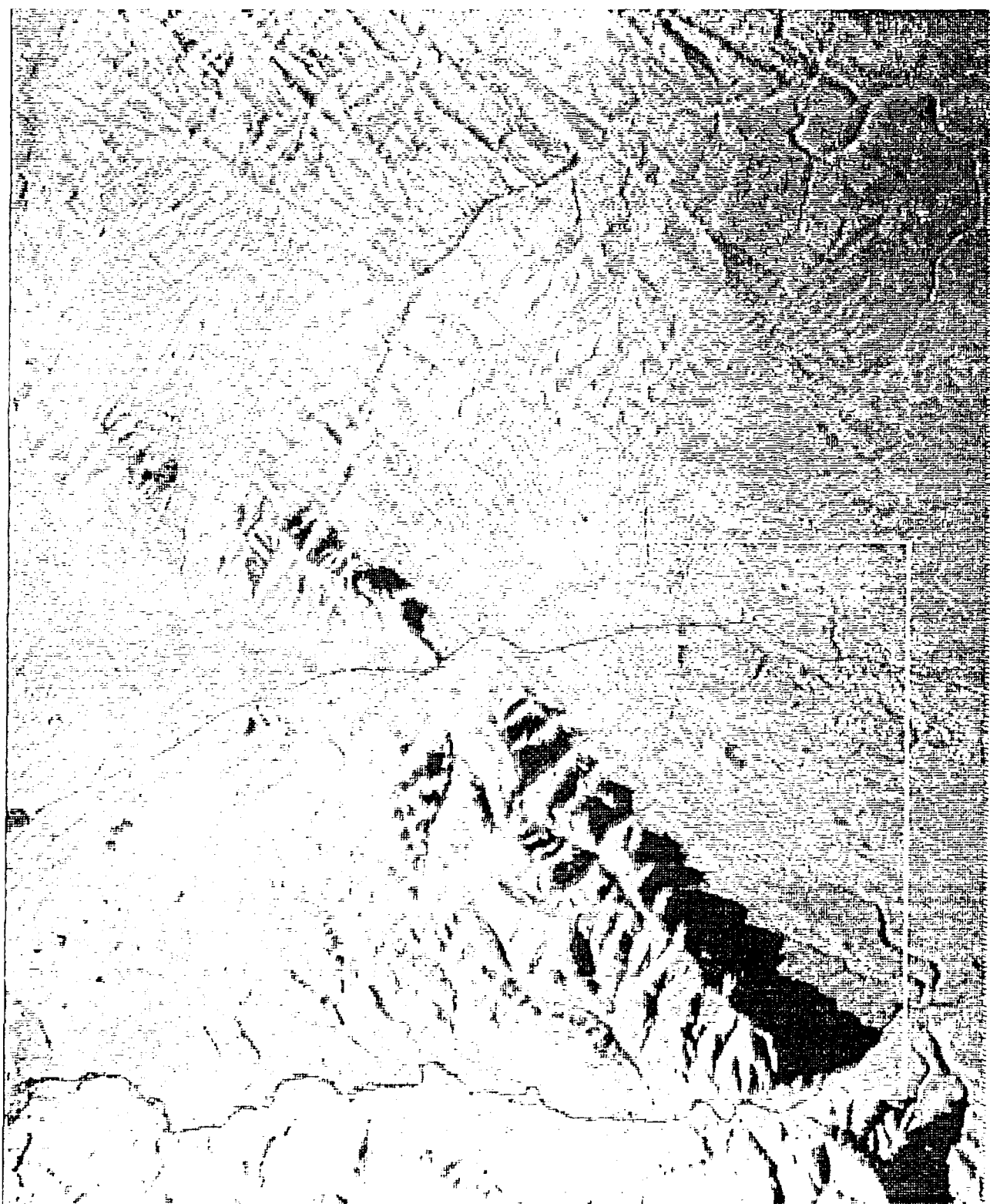




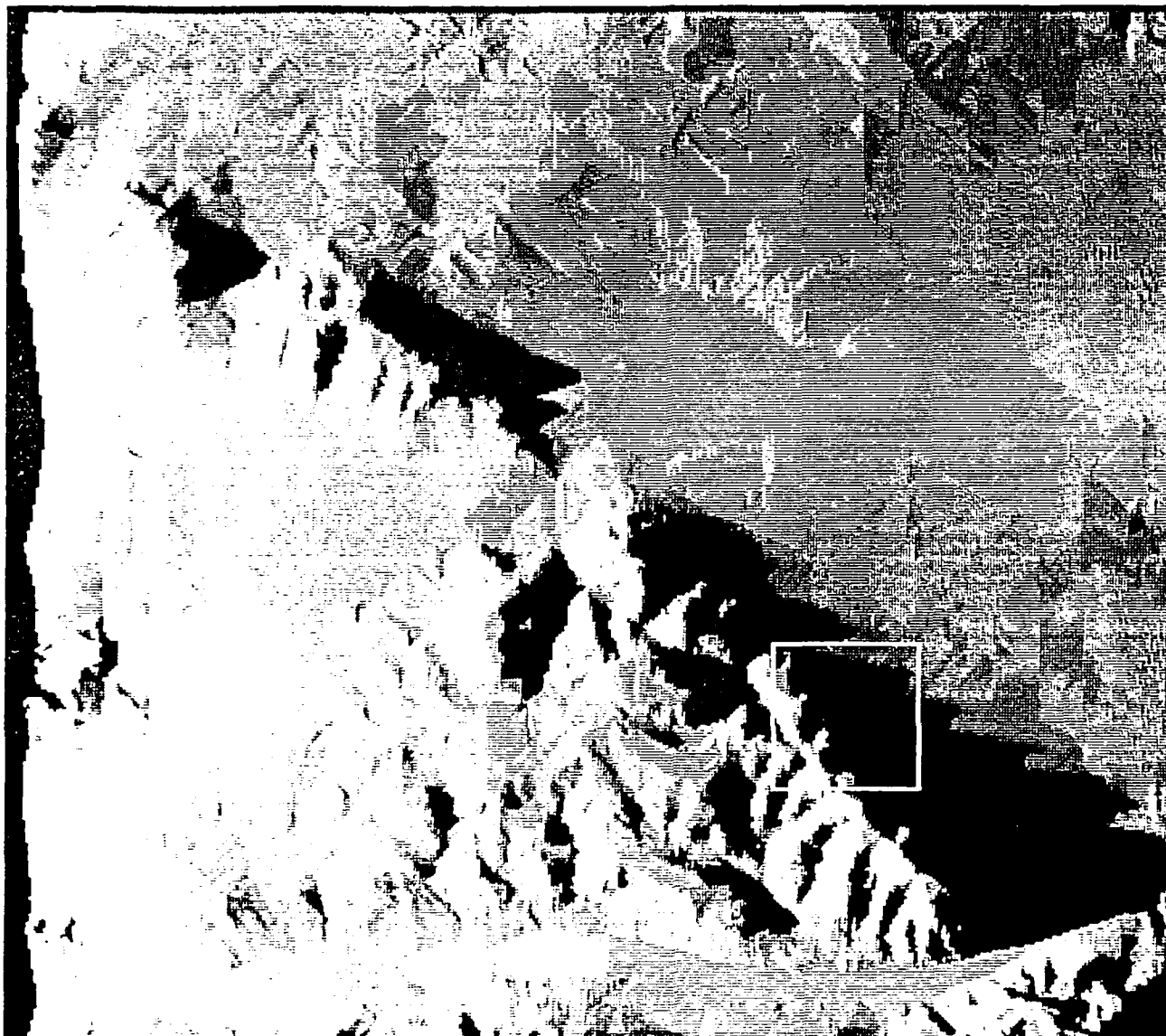




LASER SCAN: STARTUP: 001.DAT, cols 3 to 404, rows 27 to 512, 19-JAN-88 20:00:
FORMAT: PBMQ 1000; 1



LASER_GRAF Source: 008.DA, cols 24 to 423, rows 92 to 450, 19-JAN-88 20:22:
parms: 400x 359y ;



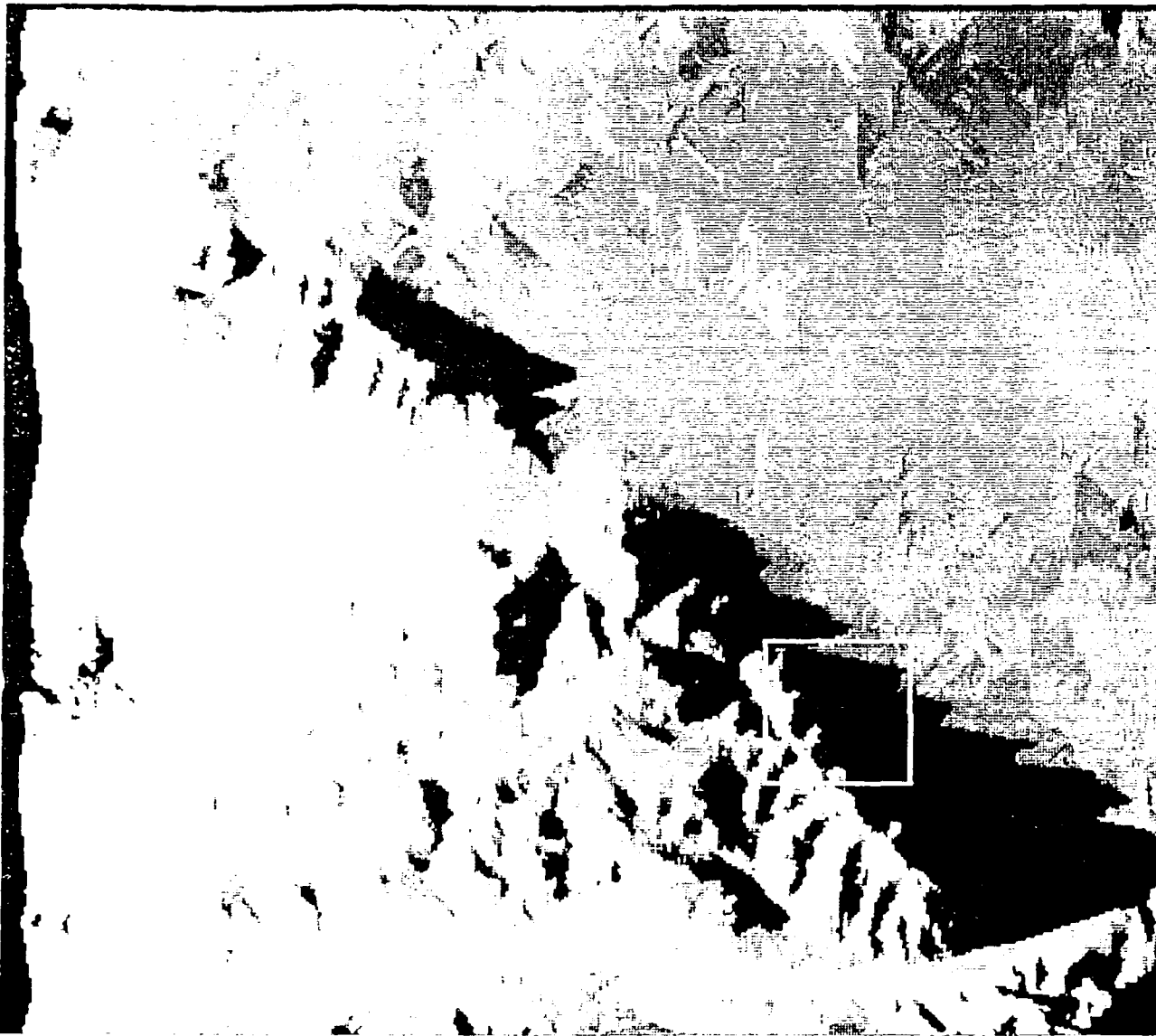
Simulated Pulsar Image - 6km flight altitude
51 x 50 box to be correlated with large box
in SAR Gray Value Image
Window Coordinates: 197,312,30,31

Figure 3.19

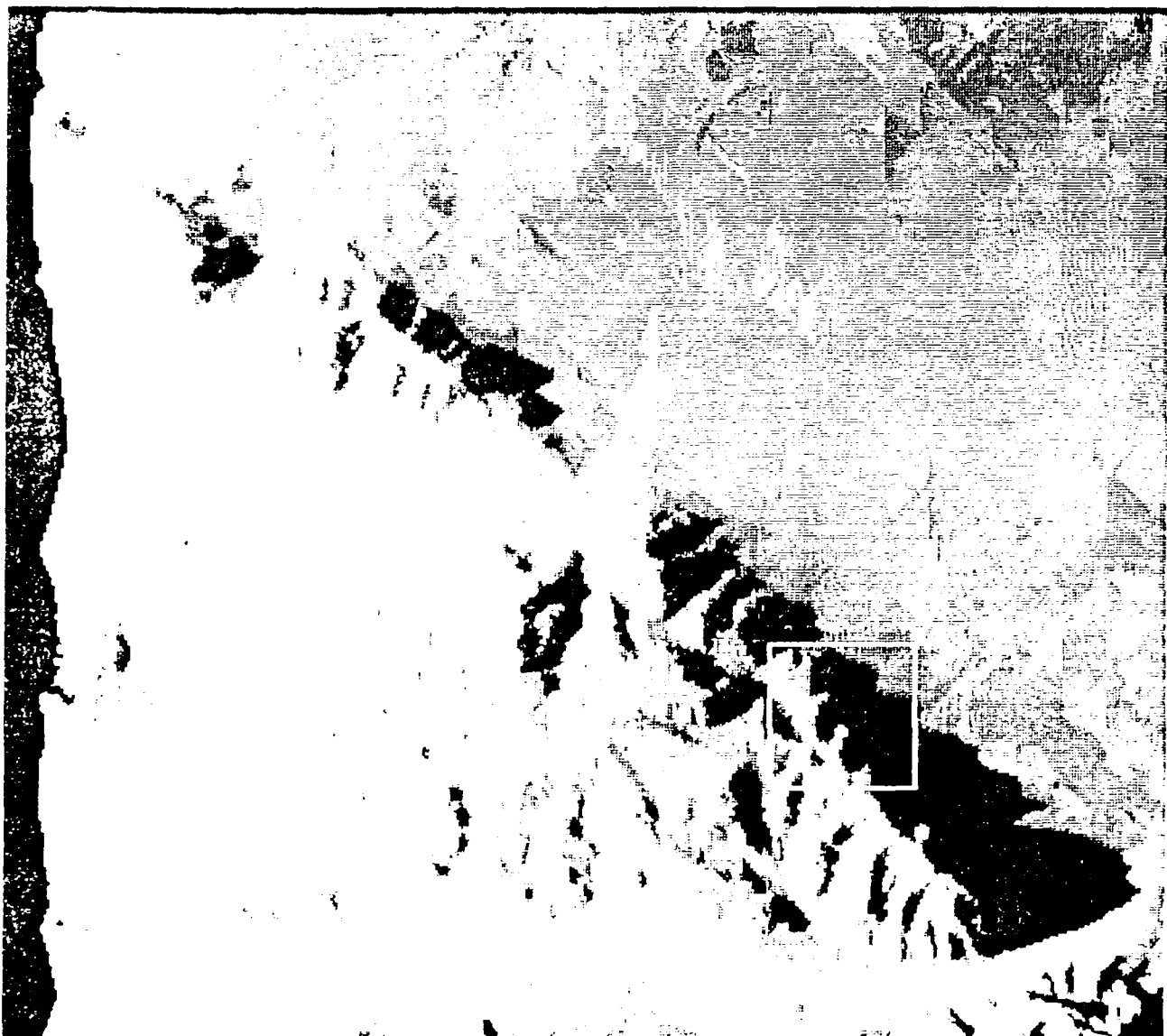
LASEP_GRAF Source: 002.DA, cols 9 to 404, rows 17 to 512, 19-JAN-88 20:01:
pixels: 386x 466y ;



2019-07-11T12:19:30Z 92.0°/150.19°/34.93°/20:23:45Z

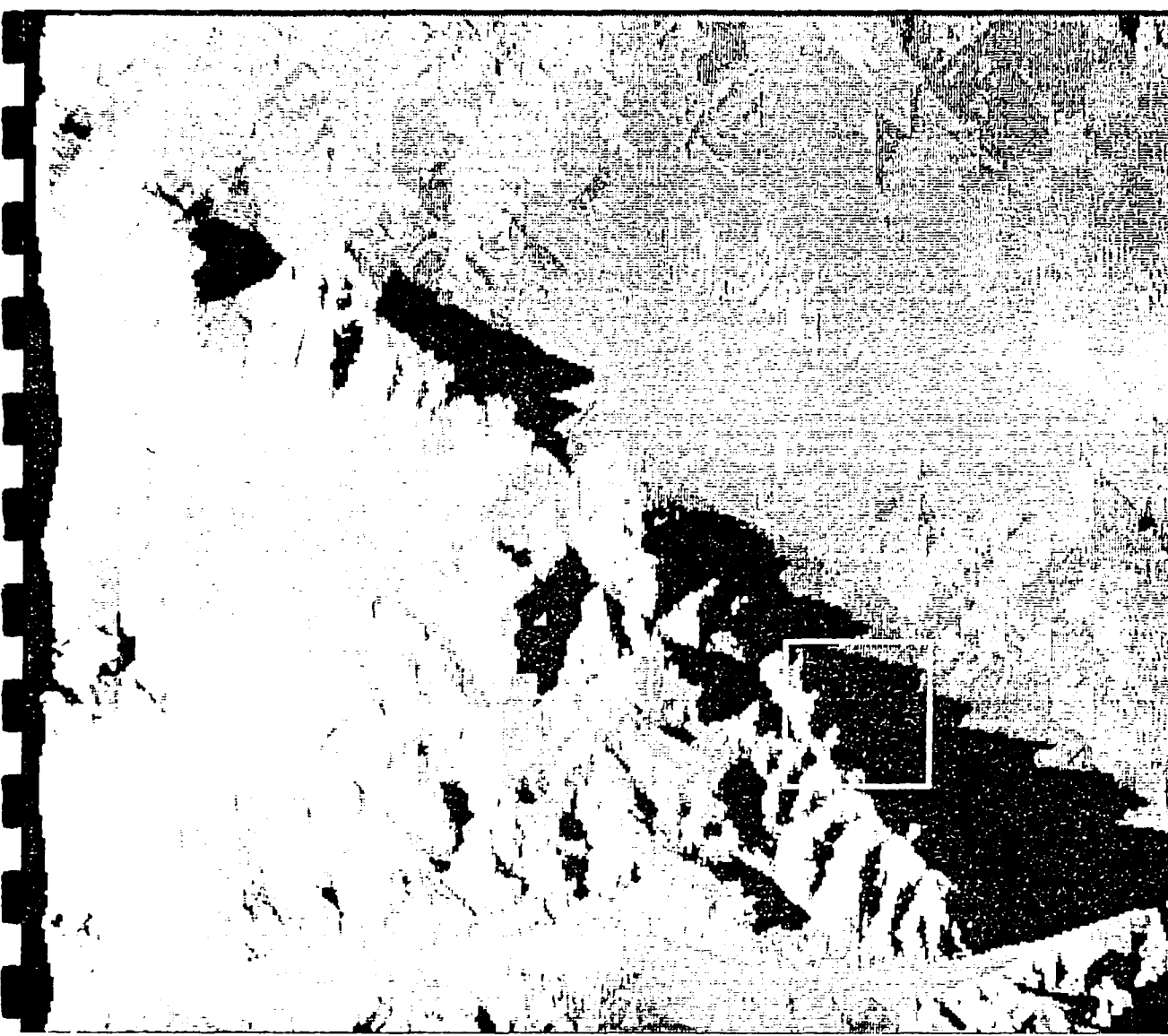






LAJER WIT SOURCE: CIB.CA, file 3 to 414, rows 27 to 312, 19-JAN-88 10:19;
frame: 3684 4864;



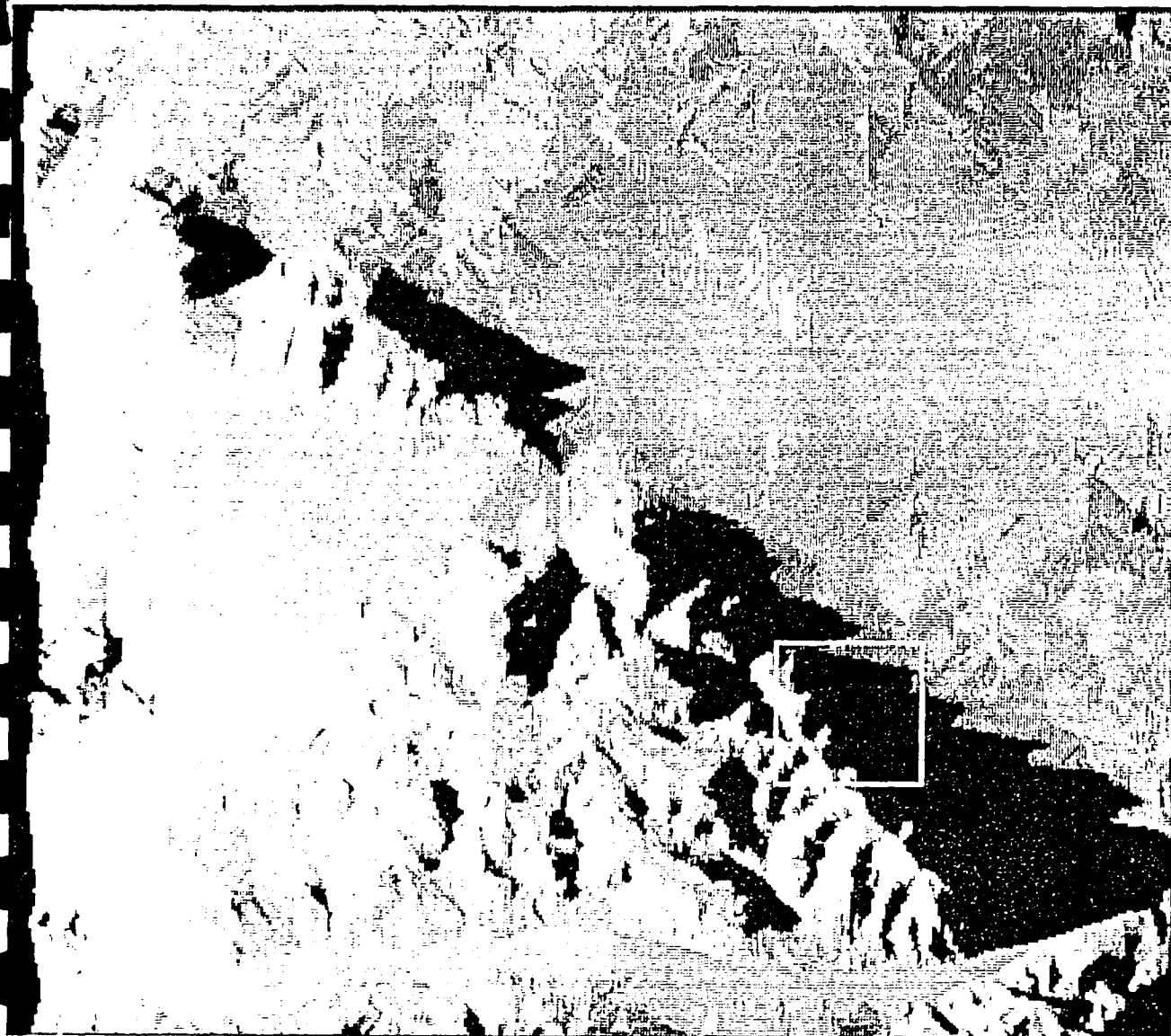


Simulated Radar Image - 5km flight altitude
10x10 box to be correlated with large box
in RF Gray Value Image
Window Correlation: 10, 20, 30, 50

Figure 3.25

LASER DRAFT Source: 103.DA, cols 9 to 404, rows 27 to 512, 19-JAN-88 20:02:
parms: 396x 486y ;



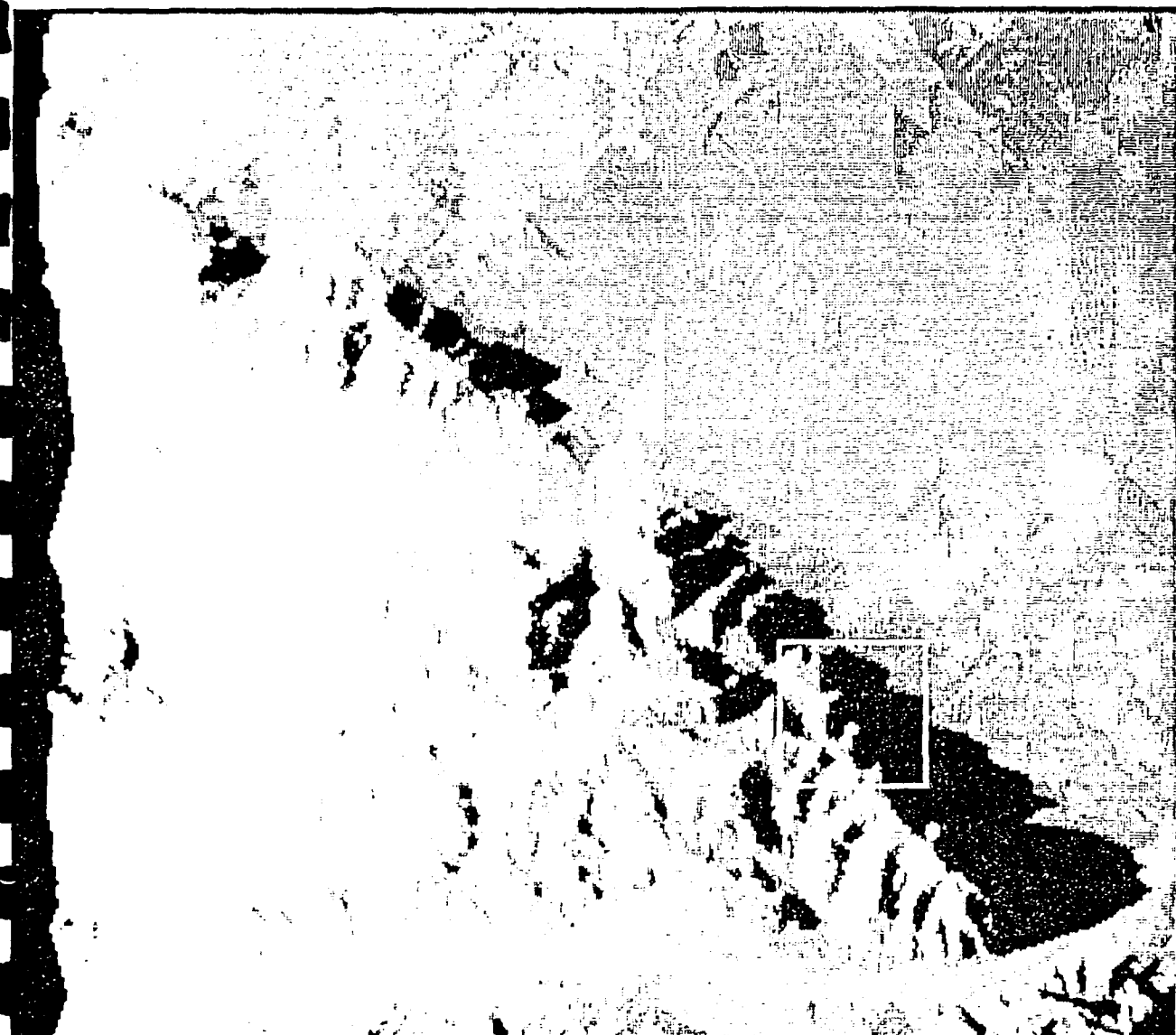


Simulated Radar Image - 8km flight altitude
50 x 50 box to be correlated with large box
in SAR Gray Value Image
Window Coordinates: 237, 313, 30, 50

Figure 3.27

11207 1000 00000: 005.0A, volc 3 to 404, rows 27 to 512, 19-JAN-68 20:04:
parts: 1000 4000;



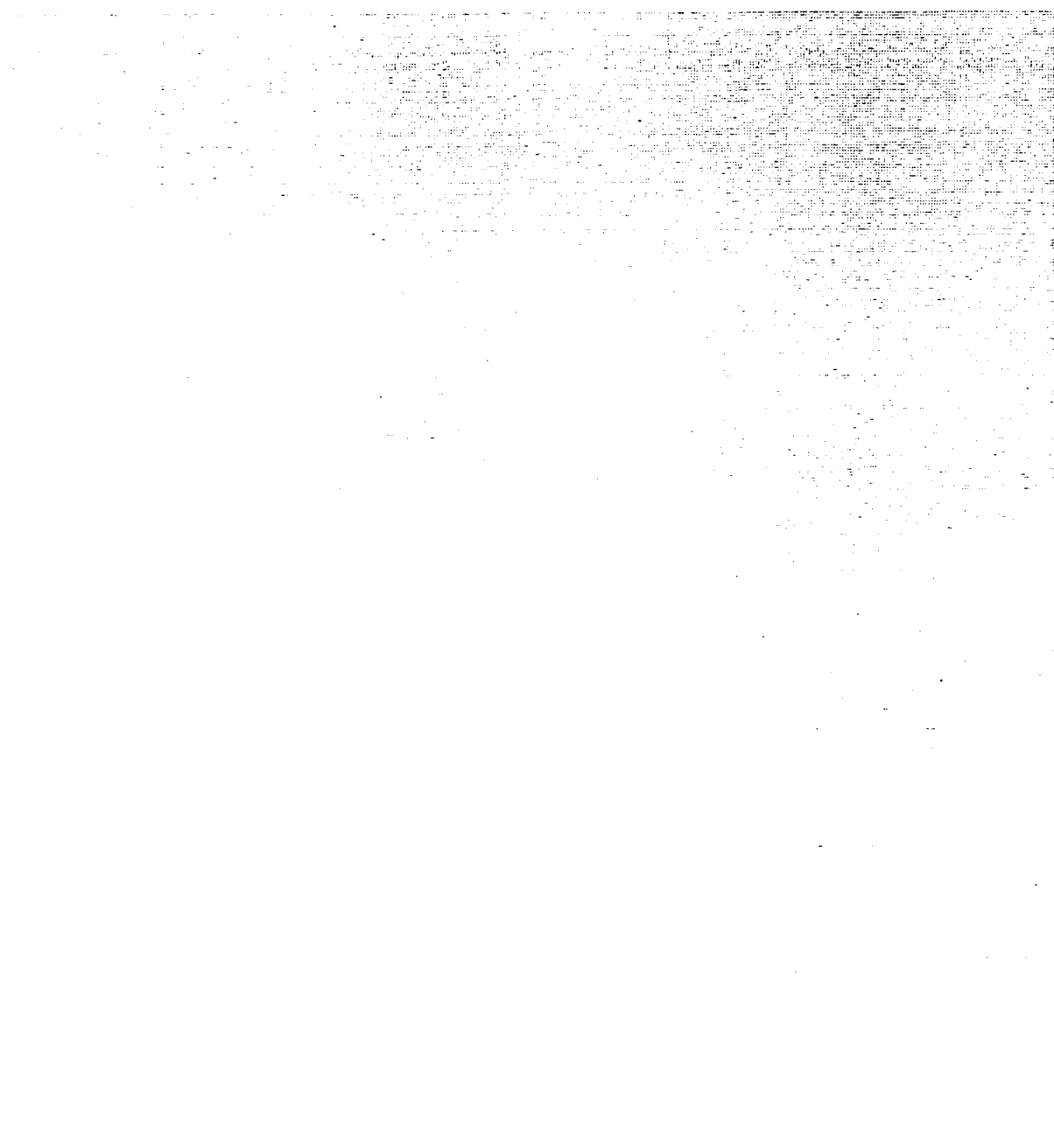


LASER_GRAF Source: 006.DA, cols 9 to 404, rows 27 to 512, 19-JAN-88 20:19:
parms: 396x x 486y ;



LASER_GRAF
Source: 006.DA, cols 9 to 404, rows 27 to 512, 19-JAN-88 20:19:
parms: 396x x 486y ;

Figure 1.60



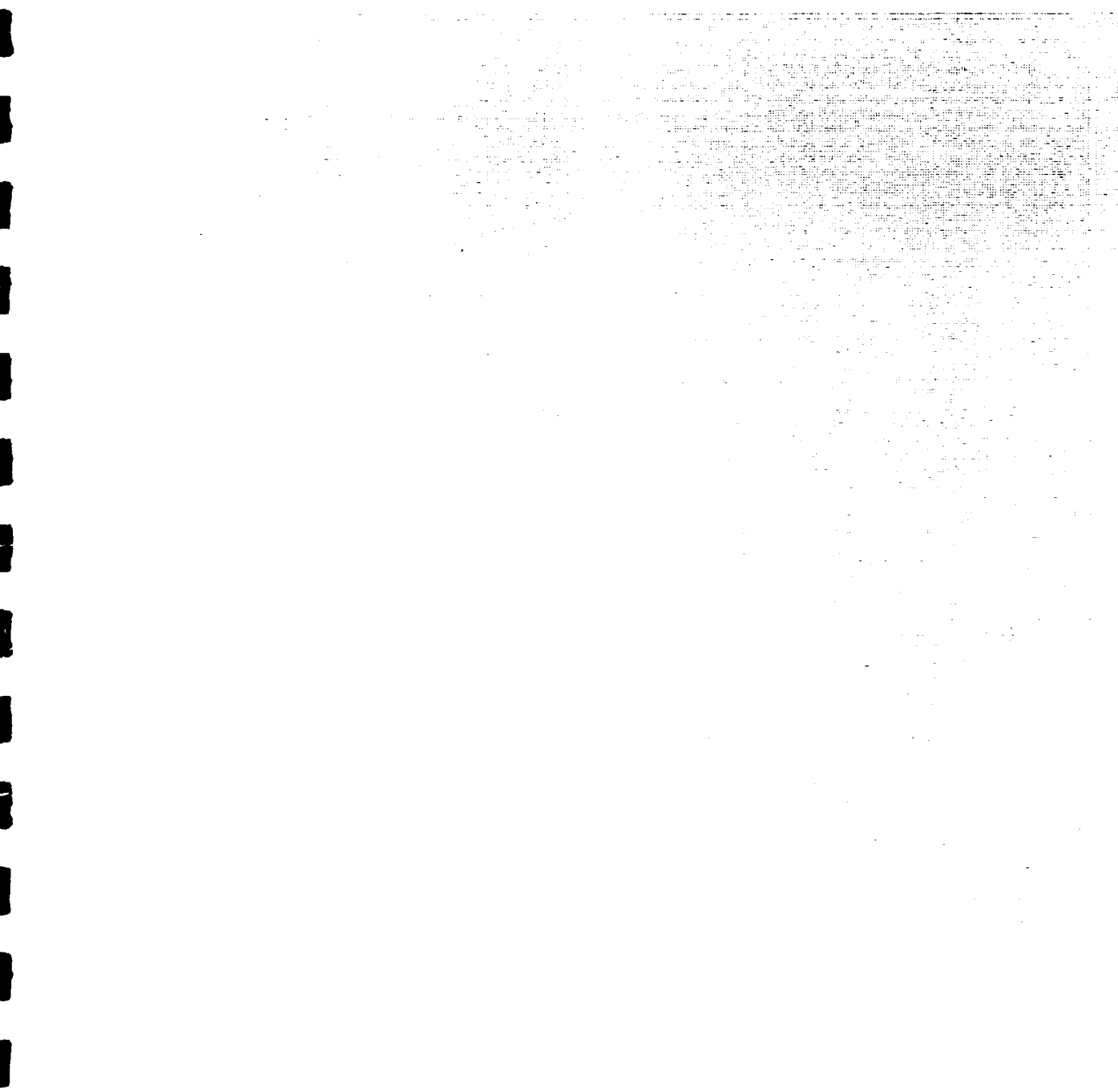
Vectorized shadow boundaries in simulated image
Brûléau Range Area, Alberta, Canada
Sensor Height: 6km
Range: 11.11km
Maximum Height in model: 2.5km
DEM Resolution: 60m x 60m x 1m

Figure 3.11

Montane and subalpine landscapes in simulated image
of eastern Banff Park, Alberta, Canada
D. J. H. Smith, D. R.
P. M. Smith
Montane and subalpine landscapes in simulated image
of eastern Banff Park, Alberta, Canada

Figure 12

LASER_GRAF Source: WENSPR, cols 26 to 452, rows 93 to 451, 10-DEC-87 20:00:
parms: 427x 359y ;



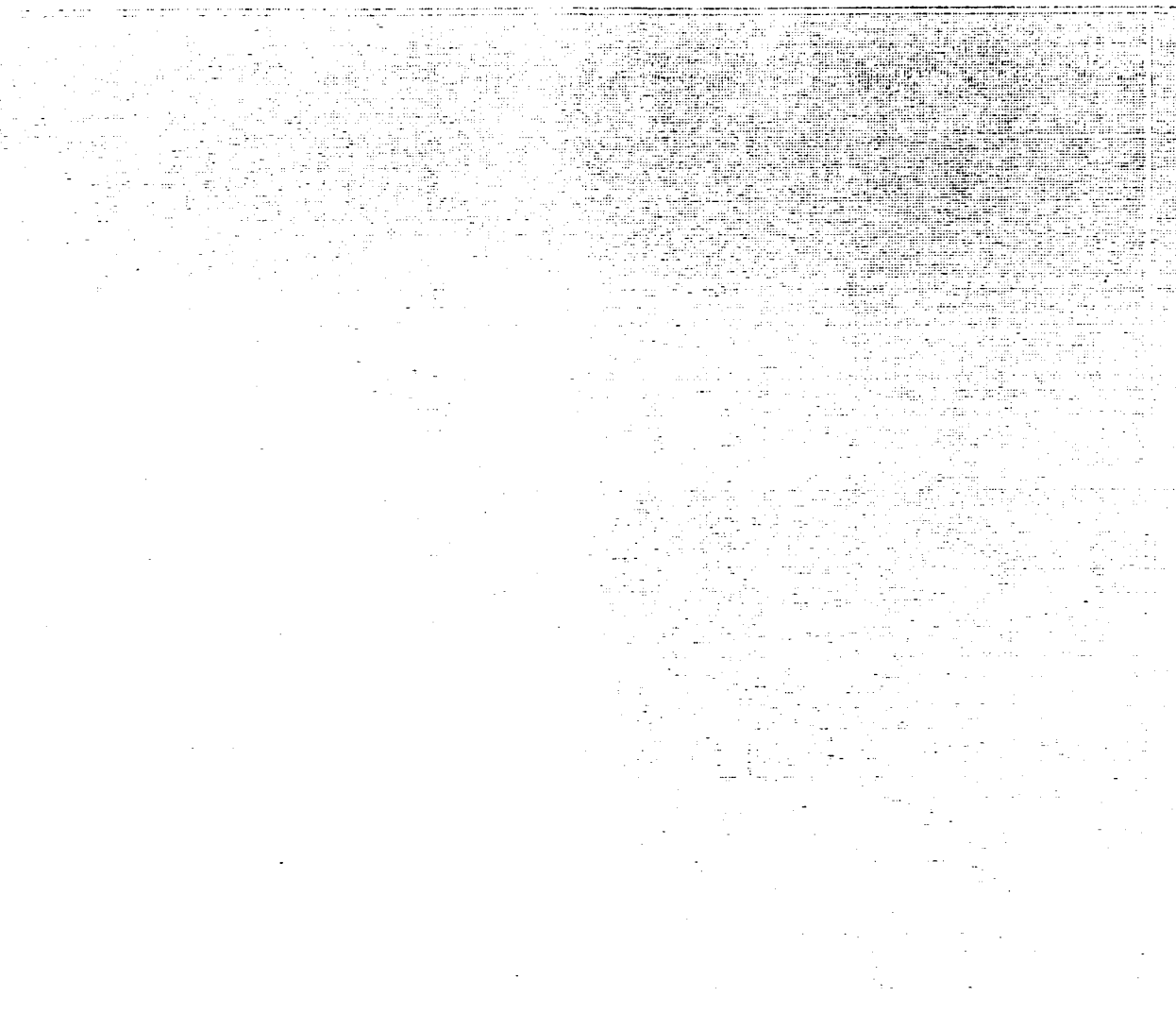
Interference pattern from a single laser beam. The image is a scan of a photograph taken with a Polaroid camera. The image is oriented vertically, with the horizontal axis representing the direction of the interference fringes.

Scanned with a Polaroid camera.

Modeling of building boundaries in simulated image
Michael R. Banks, Alberta, Canada
Michael H. Gottschalk
University of Alberta
Department of Geomatics Engineering
7444 170 Street, Edmonton, Alberta, T6G 2R3
E-mail: mgbanks@ualberta.ca

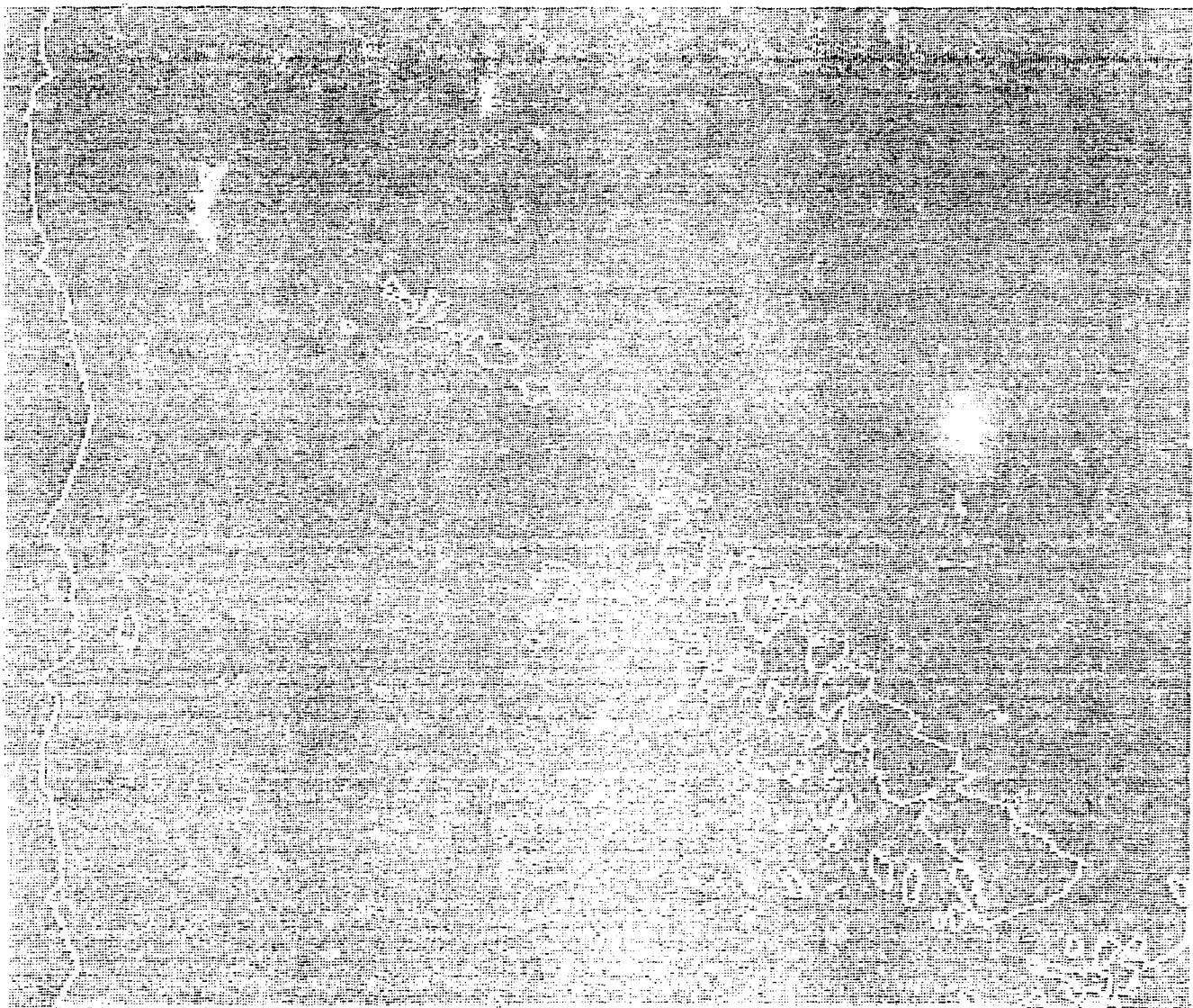
1000000000

LASER_GRAF Source: VEX\$PR, cols 26 to 452, rows 93 to 451, 10-DEC-87 20:00:
parms: 427x / 359y ;



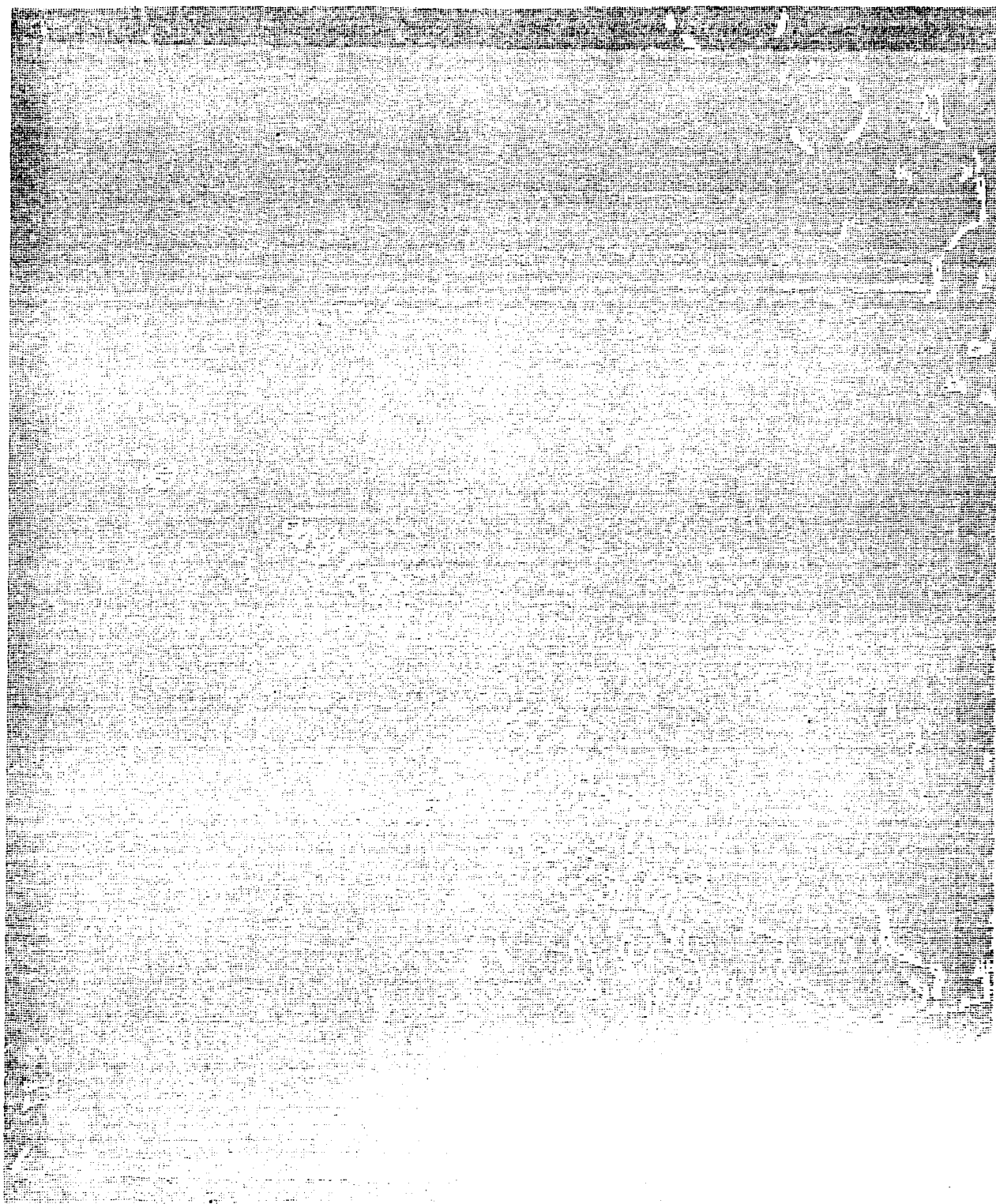
Vectorised Shadow Boundries in Simulated Image
Braceau Range Area, Alberta, Canada
Sensor Height: 10.25km
Range: 14.18km
Maximum Height in Model: 2.5km
DEM resolution: 60m x 60m x 1m

Figure 3.15



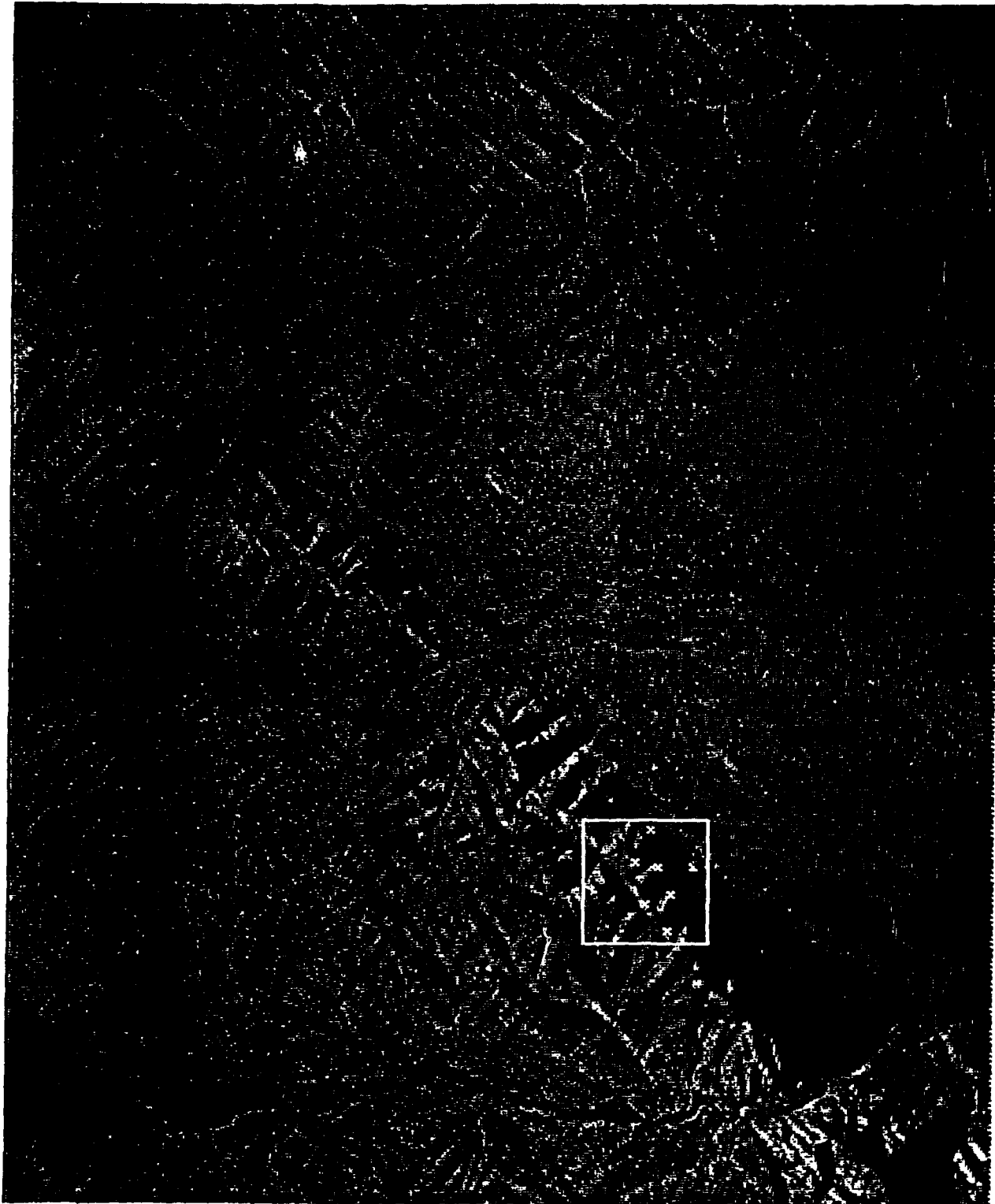
Vectorized shadow boundaries in simulated image
Brazeau Range Area, Alberta, Canada
Sensor Height: 12km
Range: 15.49km
Maximum Height in model: 2.5km
DEM Resolution: 60m x 60m x 1m

Figure 3.36



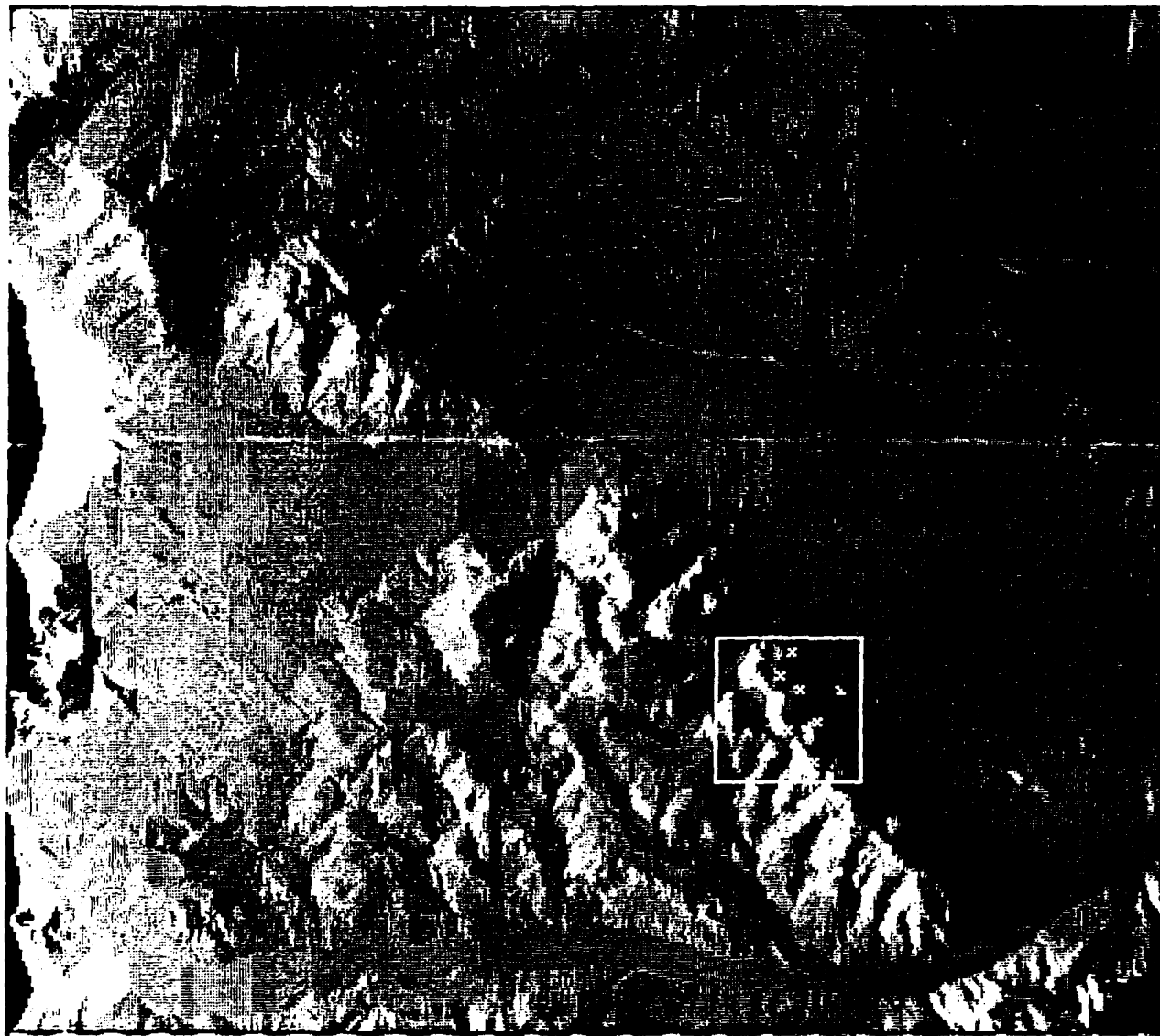
Vectorized Shadow Boundaries in actual SAR image
Brazeau Range Area, Alberta, Canada
Approximate Altitude: 10km
Approximate Range: 14km
SAR imagery by INTERA Technologies

Figure 3.37



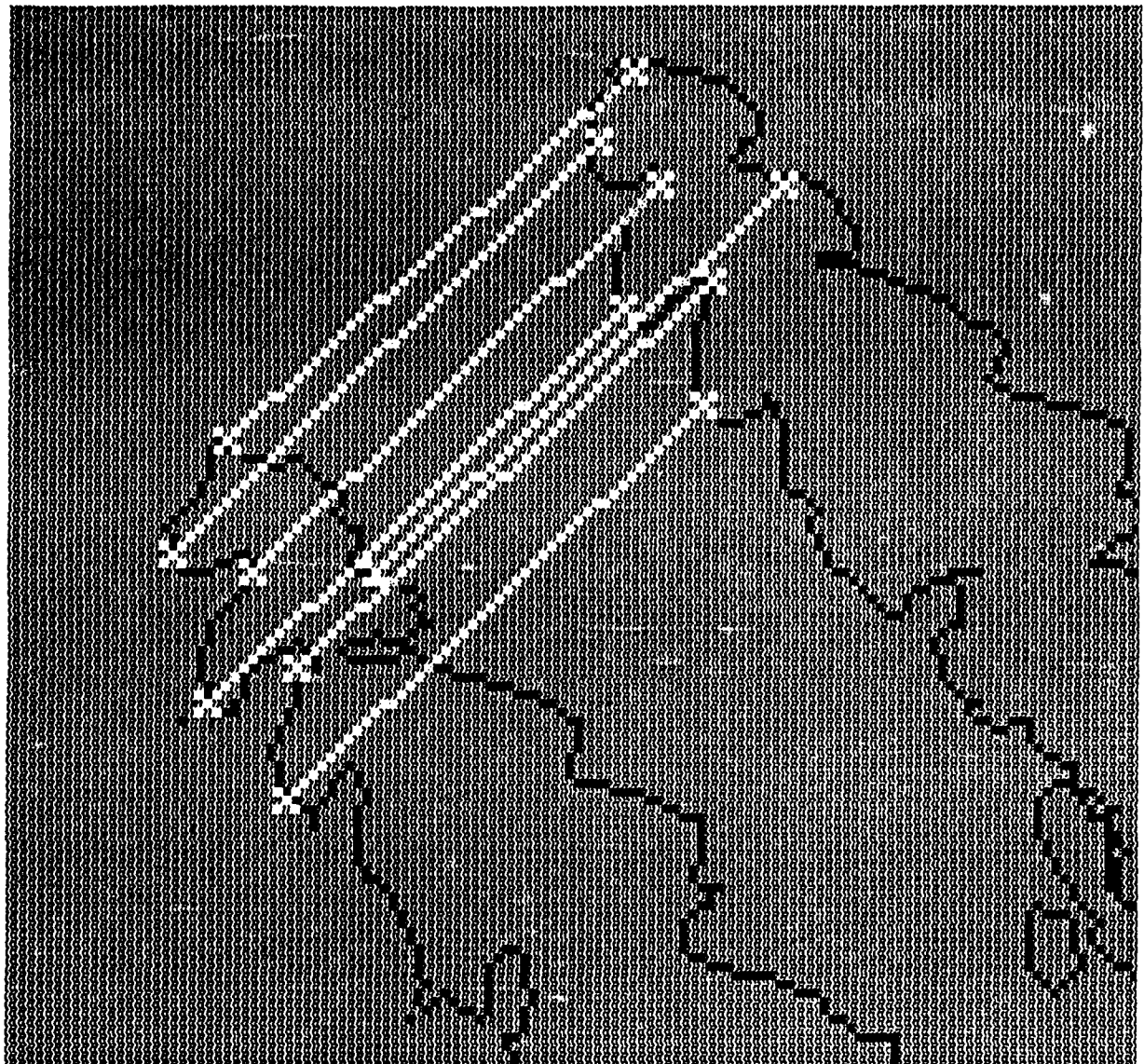
Matched Output Points in Brazeau Range SAR image
Binarization Threshold: 37
Correlation Window: 240,356,50,50

Figure 3.38



Matched Points in Brazeau Range Simulated Radar Image
Flight Altitude: 10km
Correlation Window: 287,313,50,50

Figure 3.39



Matched Points on the Vectorized Shadow Boundaries
of the SAR Image (lower) and the Synthetic Radar Image

Figure 3.40

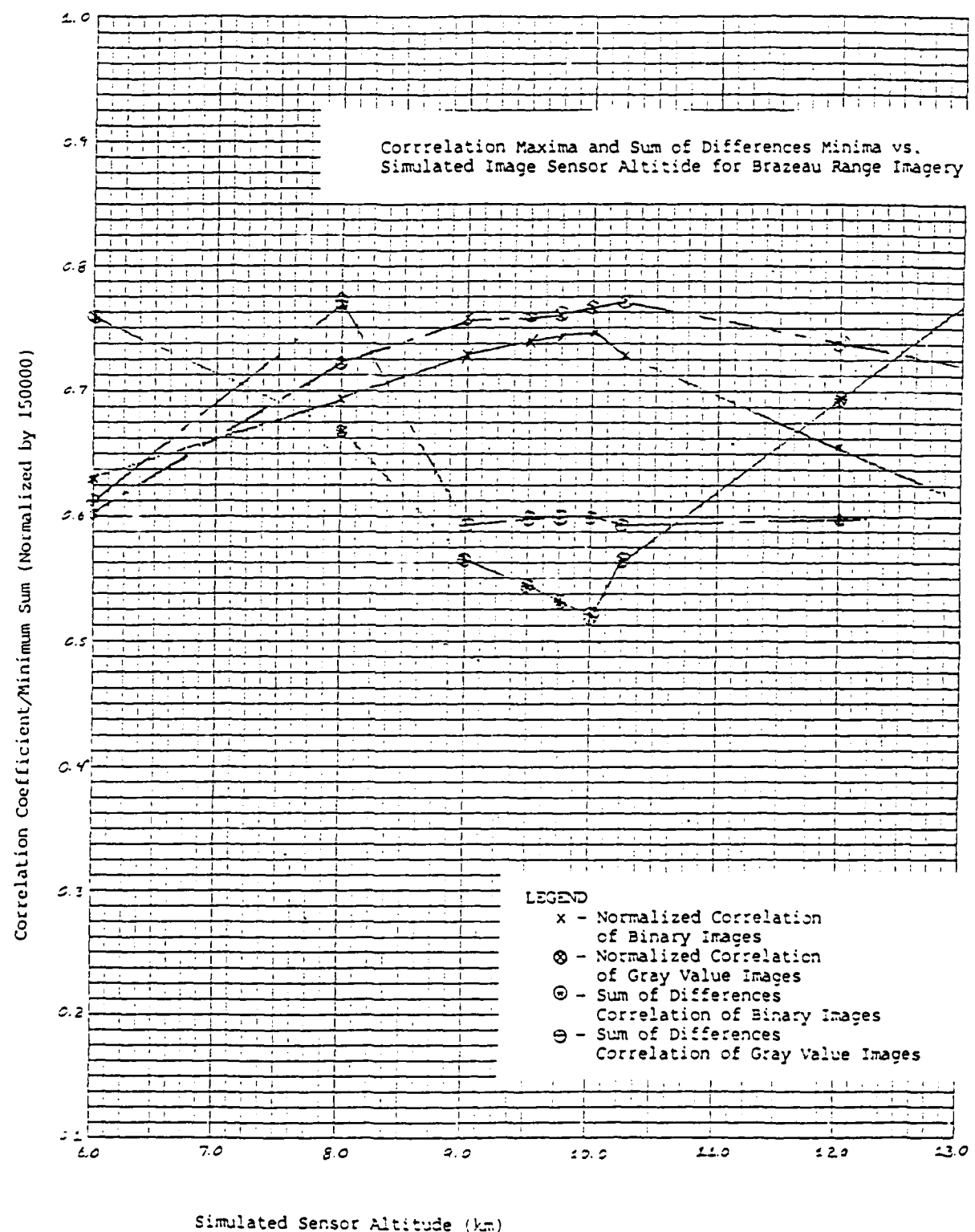
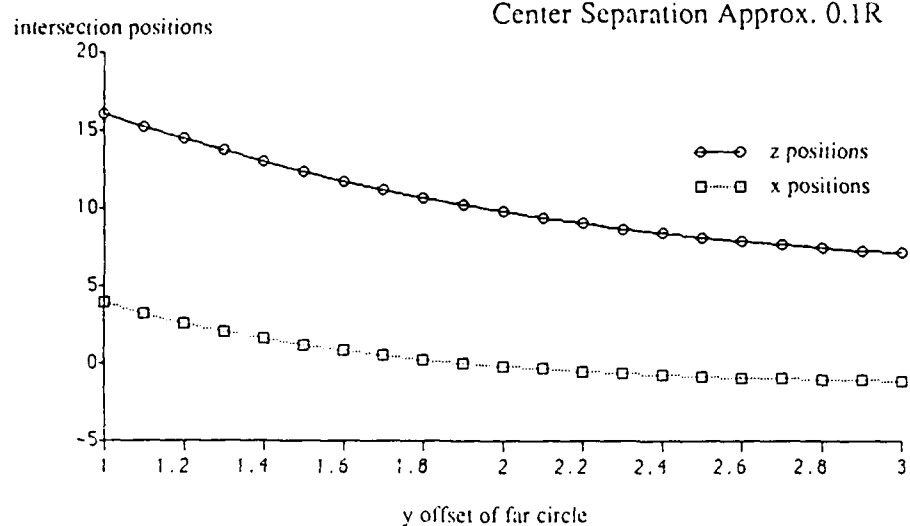


Figure 3.41

Intersections of Two Circles with
Vertical Perturbation to Far Point
Center Separation Approx. 0.1R

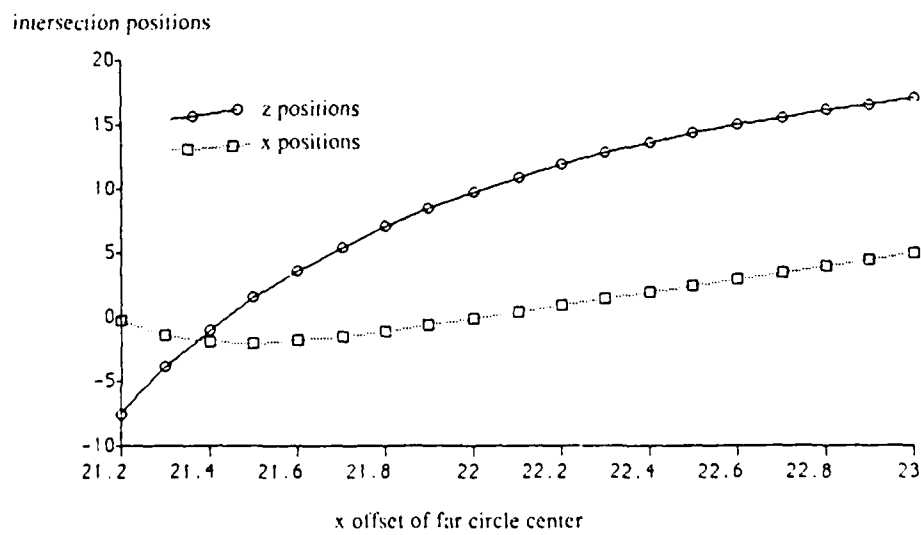


Near Circle
Center: 20,1
Radius: 20

Far Circle
Center: 22,2
Radius: 23.5

Figure 3.42

Intersections of Two Circles with
Horizontal Perturbation to Far Point
Center Separation Approx. 0.1R



Near Circle
Center: 20,1
Radius: 20

Far Circle
Center: 22,2
Radius: 23.5

Figure 3.43

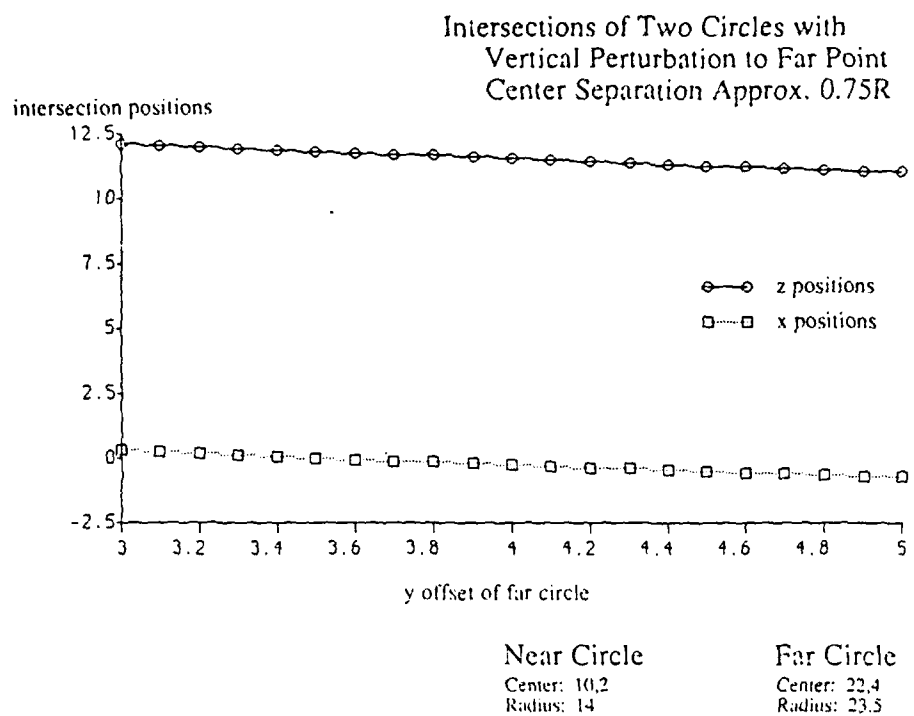


Figure 3.44

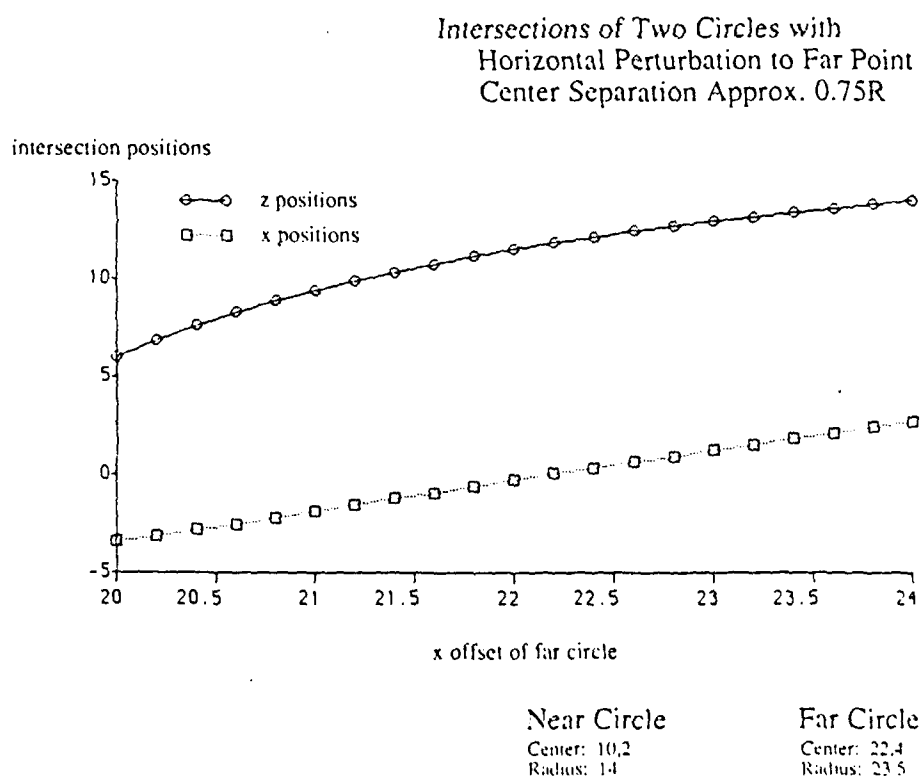


Figure 3.45

Platform Offset

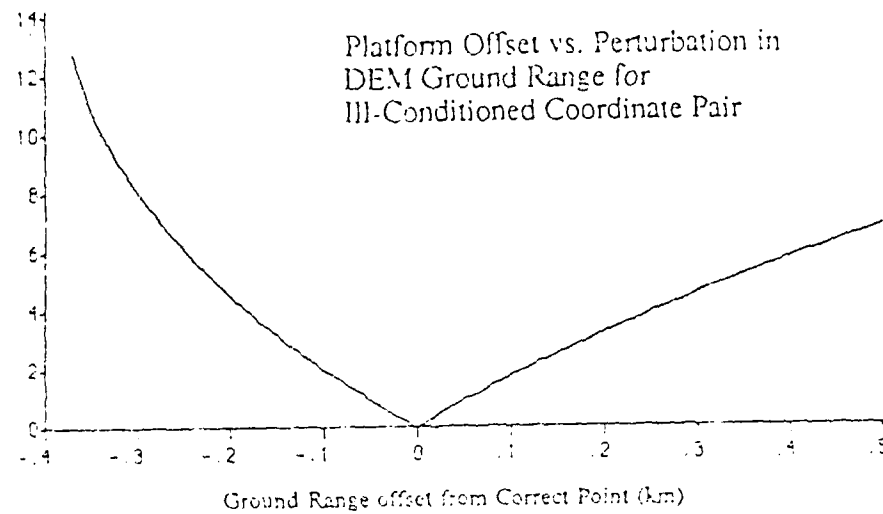


Figure 3.46a

Platform Offset (meters)

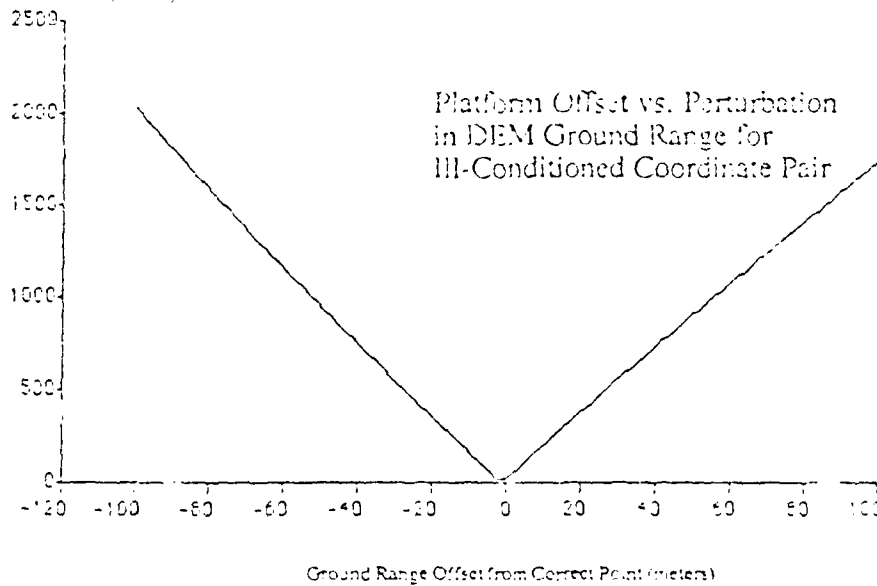


Figure 3.46b

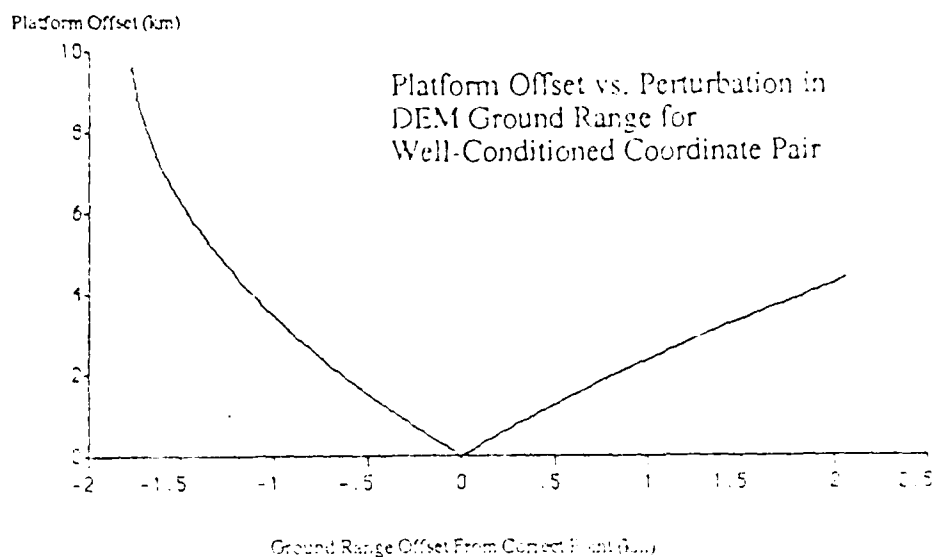


Figure 3.47a

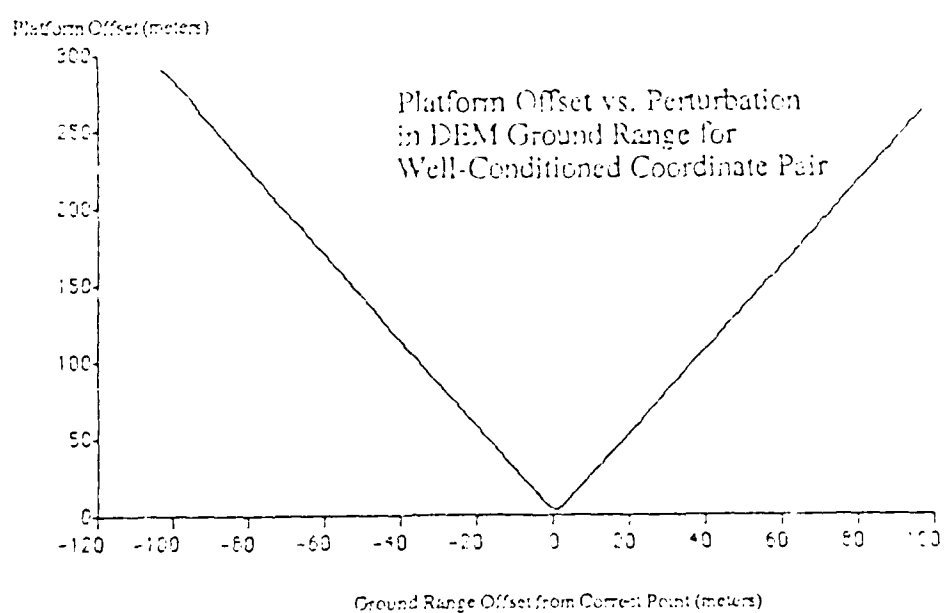


Figure 3.47b

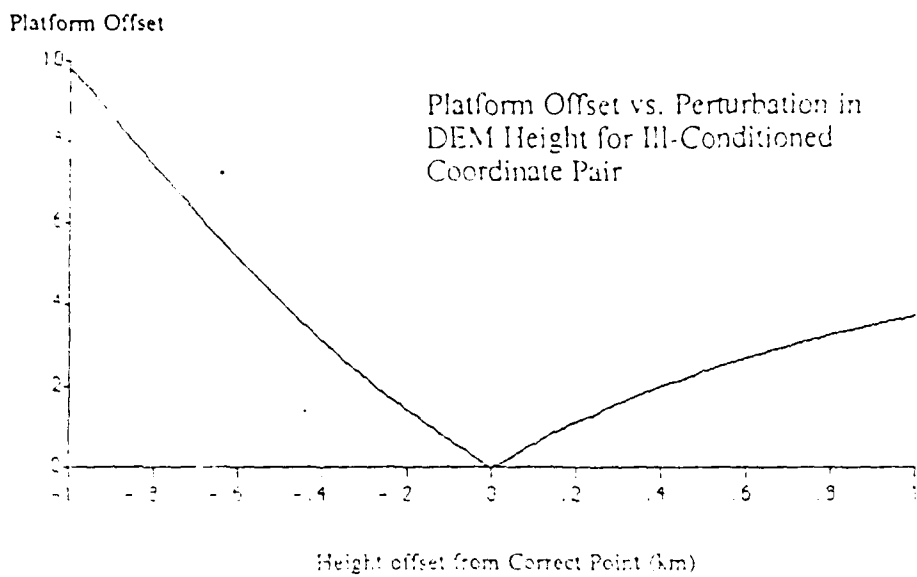


Figure 3.48a

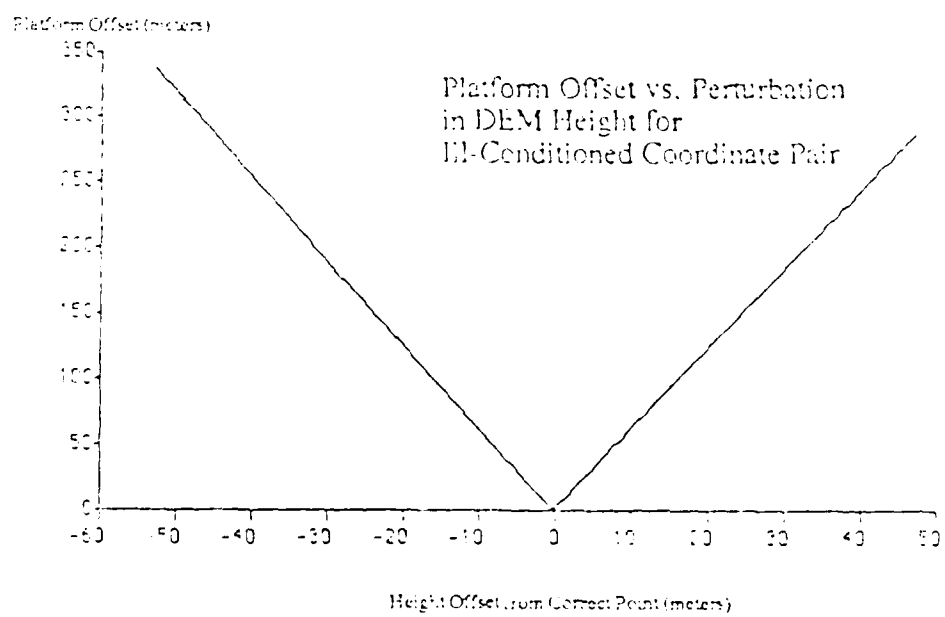


Figure 3.48b

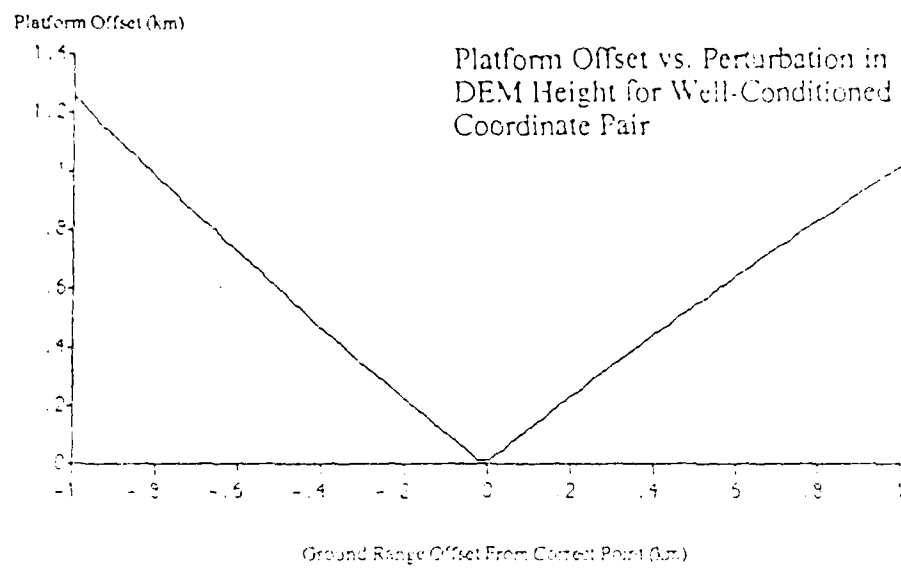


Figure 3.49a

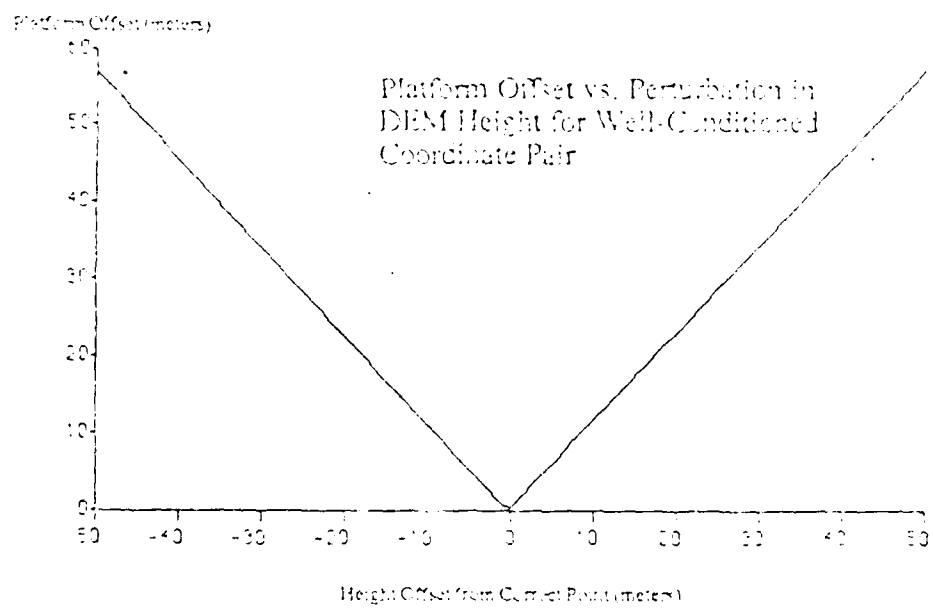


Figure 3.49b

4.0 Generation of Control Information Using Feature Data

Some of the methods described in section 1.3.3.2 on boundary matching are relevant to matching the outlines and shapes corresponding to feature data. Region matching methods may also be applicable, but may suffer some performance problems if intensity distortions are not predictable. Of course, the descriptions of feature data will be the coordinates of the endpoints of polygonal approximations.

The appearance in an optical image of such a polygonal approximation will be modified by a perspective transformation. A ground range SAR image will have some distortions if such features lie on terrain relief.

However, if these features are not distorted by terrain, then the matching techniques described in section 1.3.3.2 are applicable. Because flight path orientation is expected to be known within a degree, only translation must be estimated for a ground range SAR image.

Perspective must be estimated and accounted for in an optical image. Of course, the perspective distortion for an object at a hypothesized distance from the optical sensor is predictable from this hypothesized offset distance. Knowing the approximate height of the sensor platform, the sensor orientation, and a region of pixels that is being searched for a given feature, one can approximate the distance of the feature from the sensor. Then one can approximately predict the perspective distortion. This distortion should not vary appreciably over the field of view.

Searching for a particularly distinctive feature in the feature database is a plausible strategy, as is discussed in section 7 concerning rules for choice of features. However, another strategy is to extract features from the imagery and try to very efficiently find the corresponding features in the database. This latter approach will be discussed for future work.

The procedure that was initially explored for feature matching involved searching efficiently for one particular feature. The steps involved in using the NHAP photography were pre-processing the image to reduce the amount of micro-edges due to noise and micro-structure, and using a partial matching scheme to reduce the computational complexity of examining trial positions of the feature (see Fig. 4.16).

A more detailed summary of the steps follows:

1. Apply Sobel edge operator [Pratt,78] to image.
2. Threshold result at $+2$ sigma distributional gray value (see Fig. 4.17) to retain major edges.
3. Delete isolated pixels.
4. Convert selective feature point coordinates from UTM to image coordinates.
5. Subsample the rasterized feature (see Fig. 4.16).

6. Correlate subsampled feature pixels with pre-processed image derived at step (3), skipping offsets where a first pixel of the subset does not overlay a bright pixel.
7. Retain locations of top three correlation maxima, and test the full feature pattern at these points to obtain best estimate.
8. Use localized edge detection to obtain better estimates for tie points in feature and original image.
9. Use tie points to determine resection.

Various combinations of pre-processing steps will be investigated. Included among these will be resolution reduction to reduce amount of microstructure, edge detection, and thresholding. Some of these steps are shown in Fig. 4.2-4.15.

SAR image feature matching used STAR-2 imagery of the same general Brazeau region as for shadow matching, described in sec. 3, with reduction of resolution to 512 x 512 pixels.

Again, various combinations of pre-processing operations can be used to improve the efficiency of the feature matching process for a particular selected feature. Combinations of the following steps will be explored:

R = resolution reduction

L = Lee's sigma filter (see sec.3.2.1.1)

S = Sobel edge detection

T = thresholding using bimodality of processed image histogram

n (digit) = thresholding at $+n$ std. dev. gray value

V = vectorization of binary image boundaries

The following combinations of these steps are expected to be examined:

LS1	LS2	LS3	LTS	LTS1
LTS2	LTS3	LTV		
RS1	RS2	RS3	RTS	RTV
RLS1	RLS2	RLS3	RLTS	RLTV
LTVR	LTSR			

Another approach that will be explored involves major edge extraction from the image to obtain significant boundaries that will be used to selectively search the feature database. Relaxation methods have been used to some extent for obtaining such major contours [Rosenfeld,82], and will be explored in the next effort.

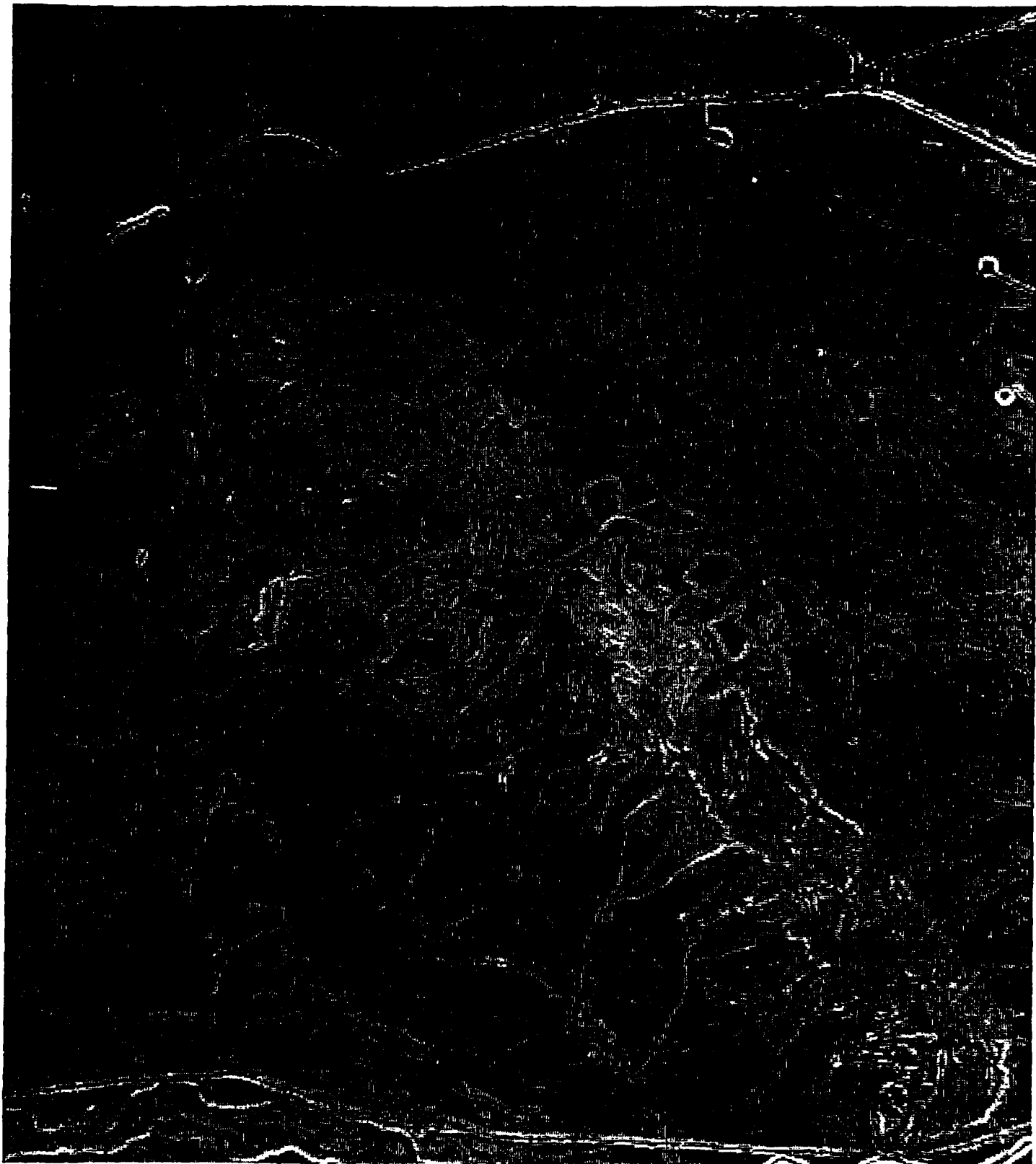
In this approach, the feature database is only selectively searched because the database has been organized in geometric feature groupings offline. Such geometric groupings are analogous to hash coding addresses in ordinary databases, and thus the term "geometric hashing" [Schwarz,86], [Kalvin,87] (see sec. 1.3.3). Another unexplored representation uses fractals for feature representation [Barnsley,88]. This representation has been used for image compression, but not for model-based recognition. Such approaches for reducing database search will be investigated in the follow-on Options.

The approach just described is distinct from the previous approach which first selects a feature from the database and then searches the image for it.



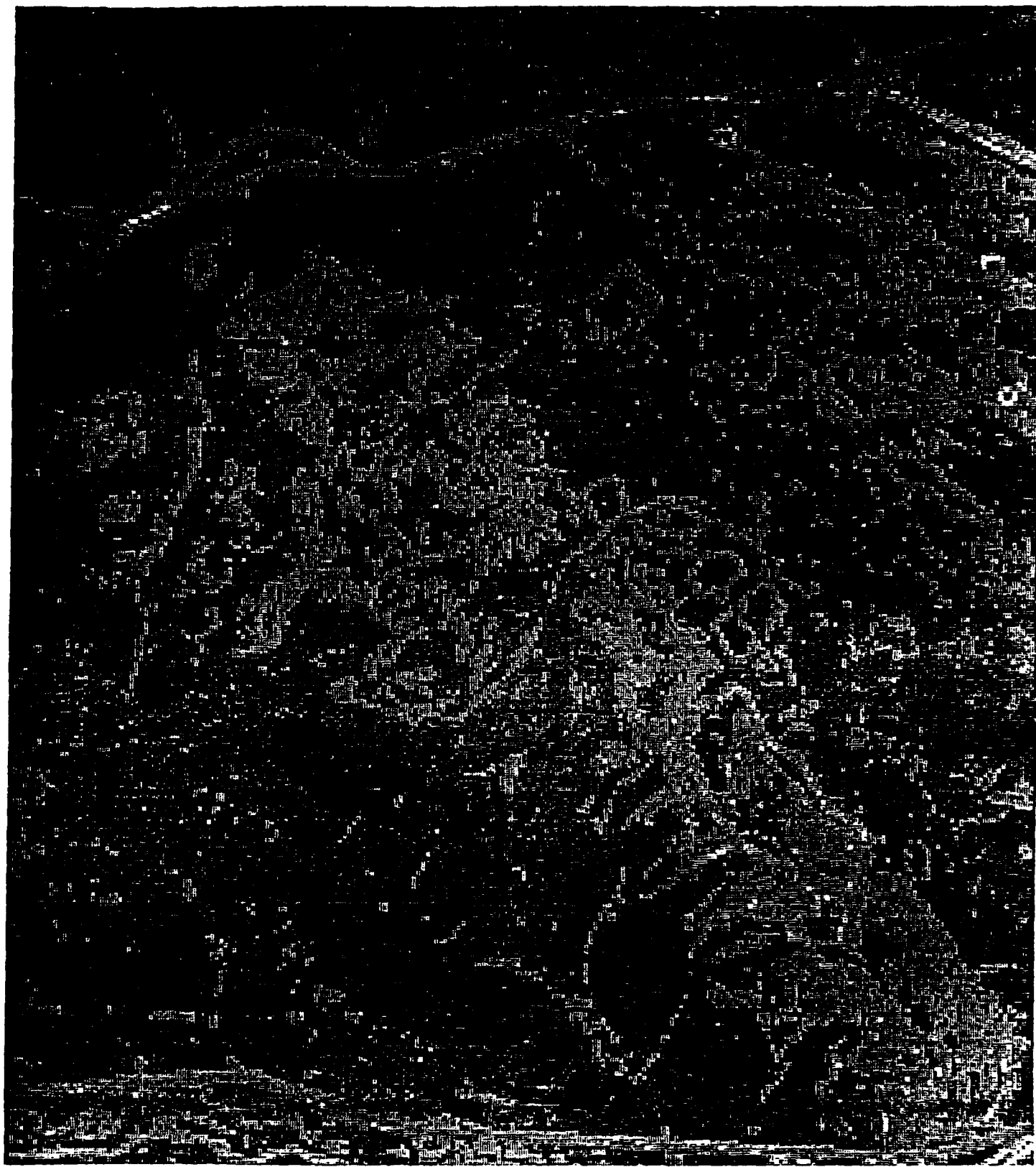
Brazeau Range Aerial Image, Alberta, Canada
NHAP Photography Digitized at USC
Frame 176

Figure 4.1



Sobel Edge image of NHAP Frame 176, Original Histogram
Brazeau Range Aerial Photography, Alberta, Canada

Figure 4.2



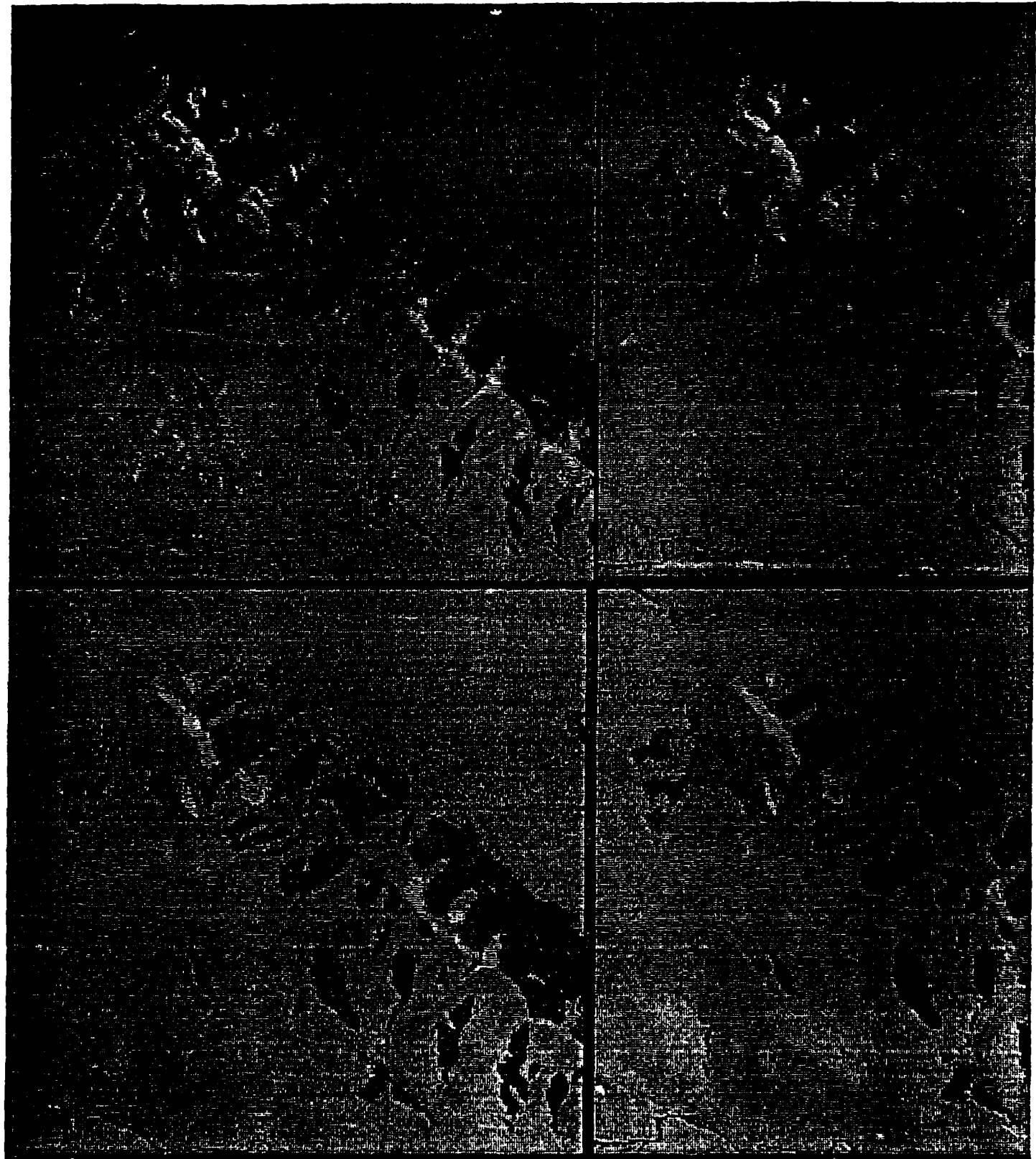
Reduced resolution Sobel Image of Frame 176, Original Histogram
Braceau Range Aerial Photography, Alberta, Canada

Figure 4.3



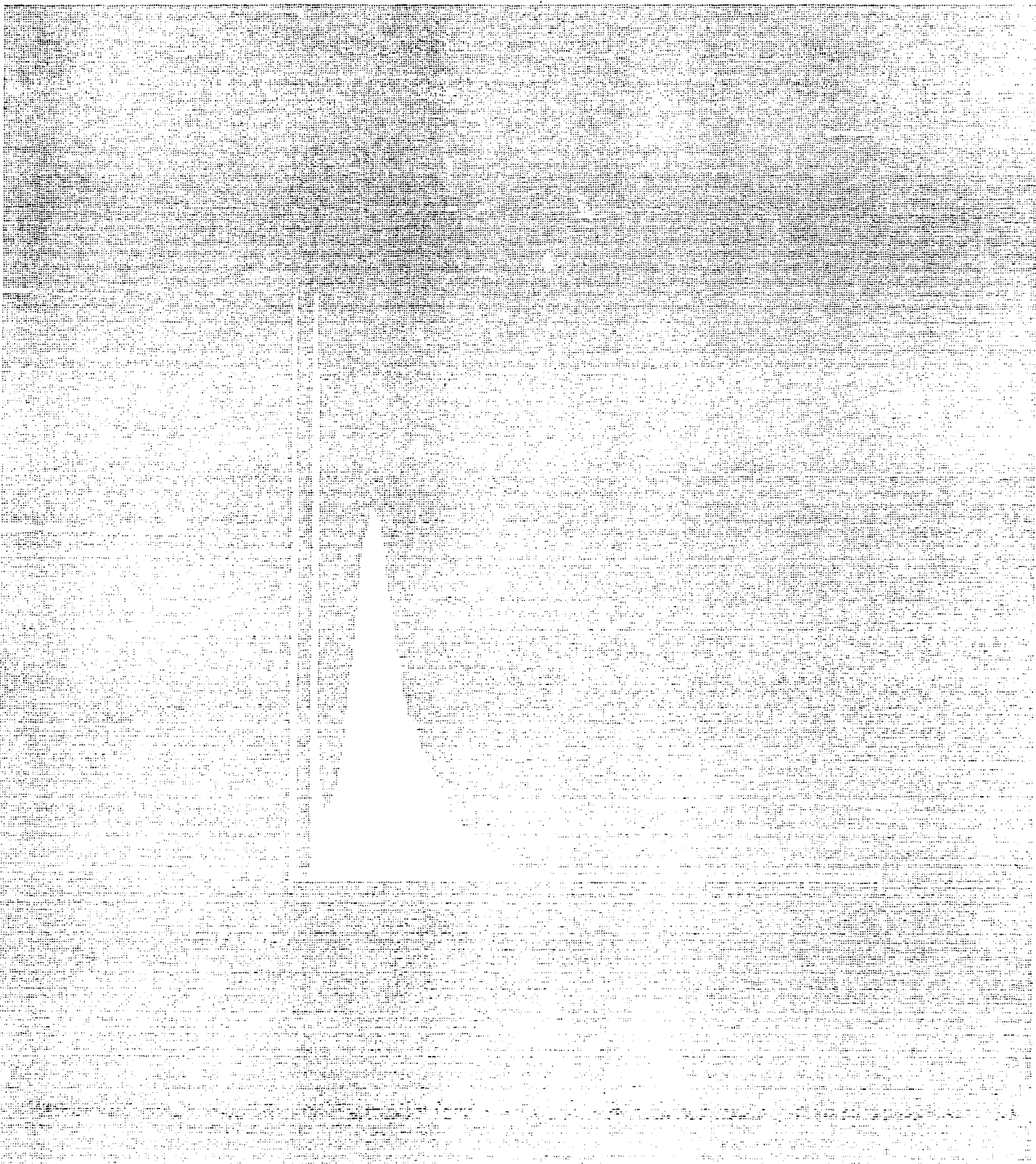
STAR-2 Radar Image of Brazeau Range Area
STAR-2 Airborne Radar, Intera Ltd.

Figure 4.4



Comparison of Lee Sigma Filtered Versions of
STAR-2 Radar Imagery. (Left to right) Sigma = 0, 15, 30, 45

Figure 4.5



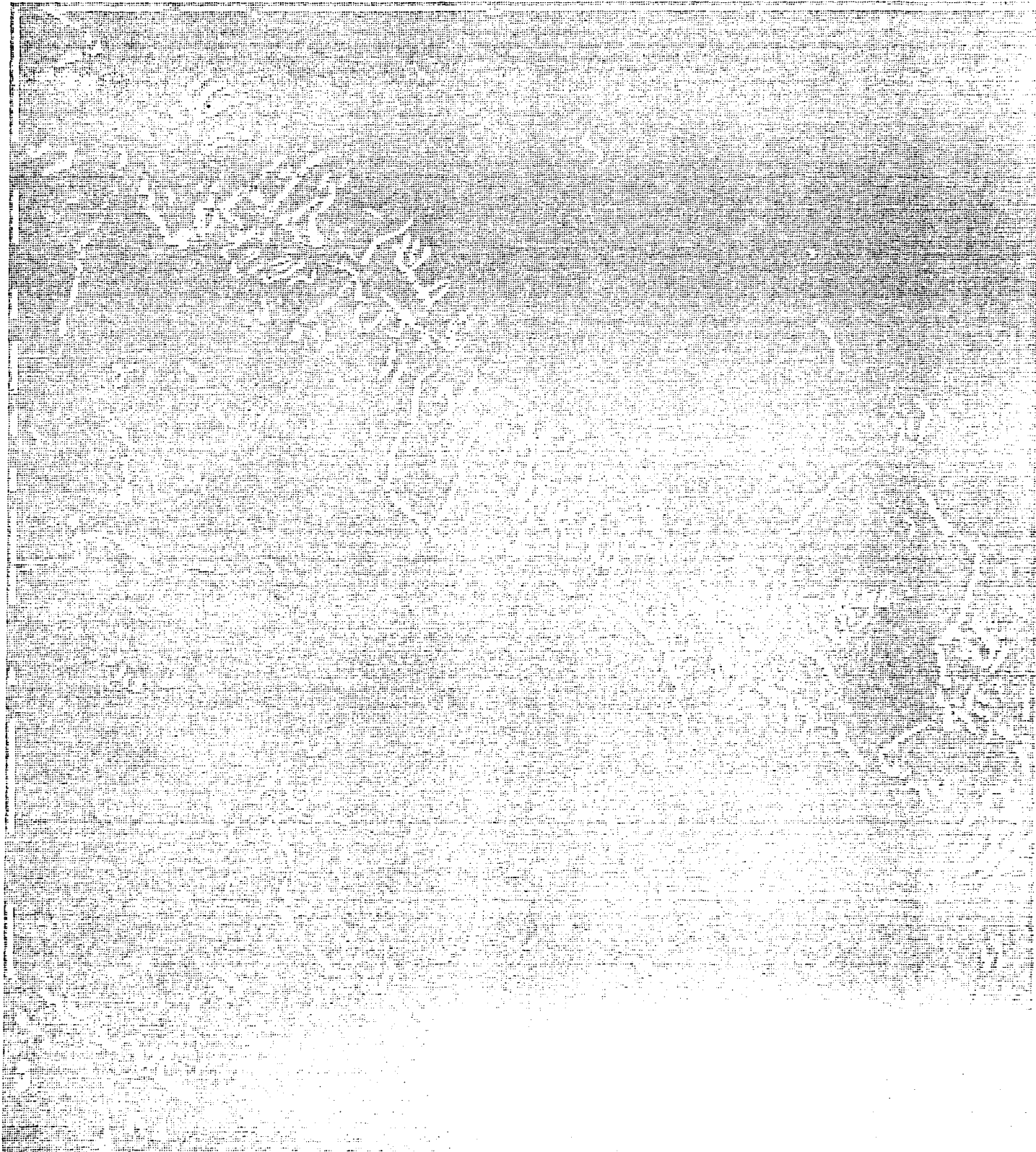
Histogram of STAR-2 radar image

Figure 4.6



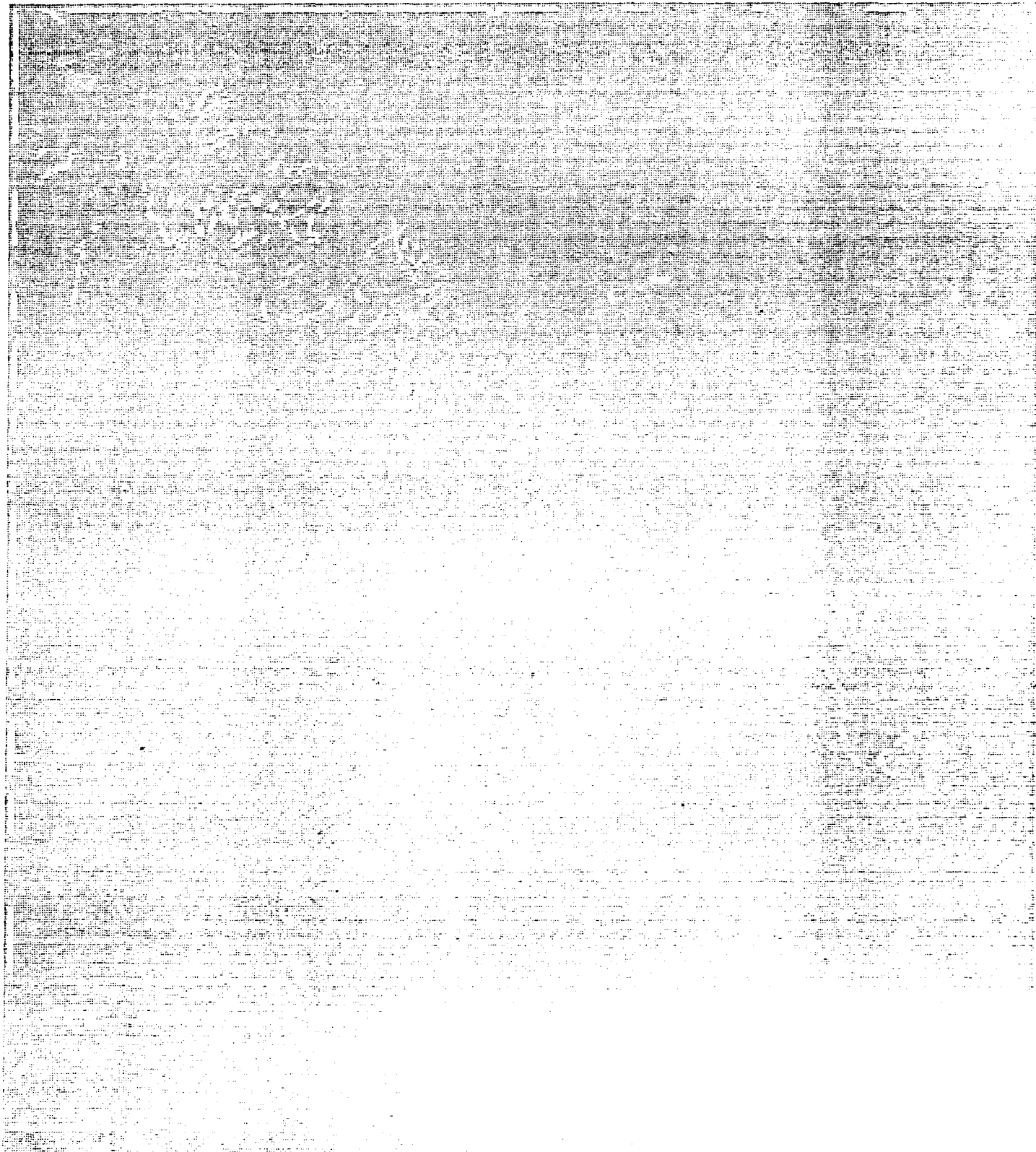
STAR-2 Image of Brazeau Range Area
Preprocessing: Lee sigma filter
Sobel edge image
Threshold at mean + sigma

Figure 4.7



STAR-2 Image of Brazeau Range Area
Preprocessing: Lee sigma filter
Sobel edge image
Threshold at mean + 2 * sigma

Figure 4.8



STAR-2 Image of Brazeau Range Area
Preprocessing: Lee sigma filter
Sobel edge image
Threshold at mean + 3 * sigma

Figure 4.9



STAR-2 Image of Brazeau Range Area
Preprocessing: Lee sigma filter
Threshold by bimodal histogram
Sobel edge image

Figure 4.10



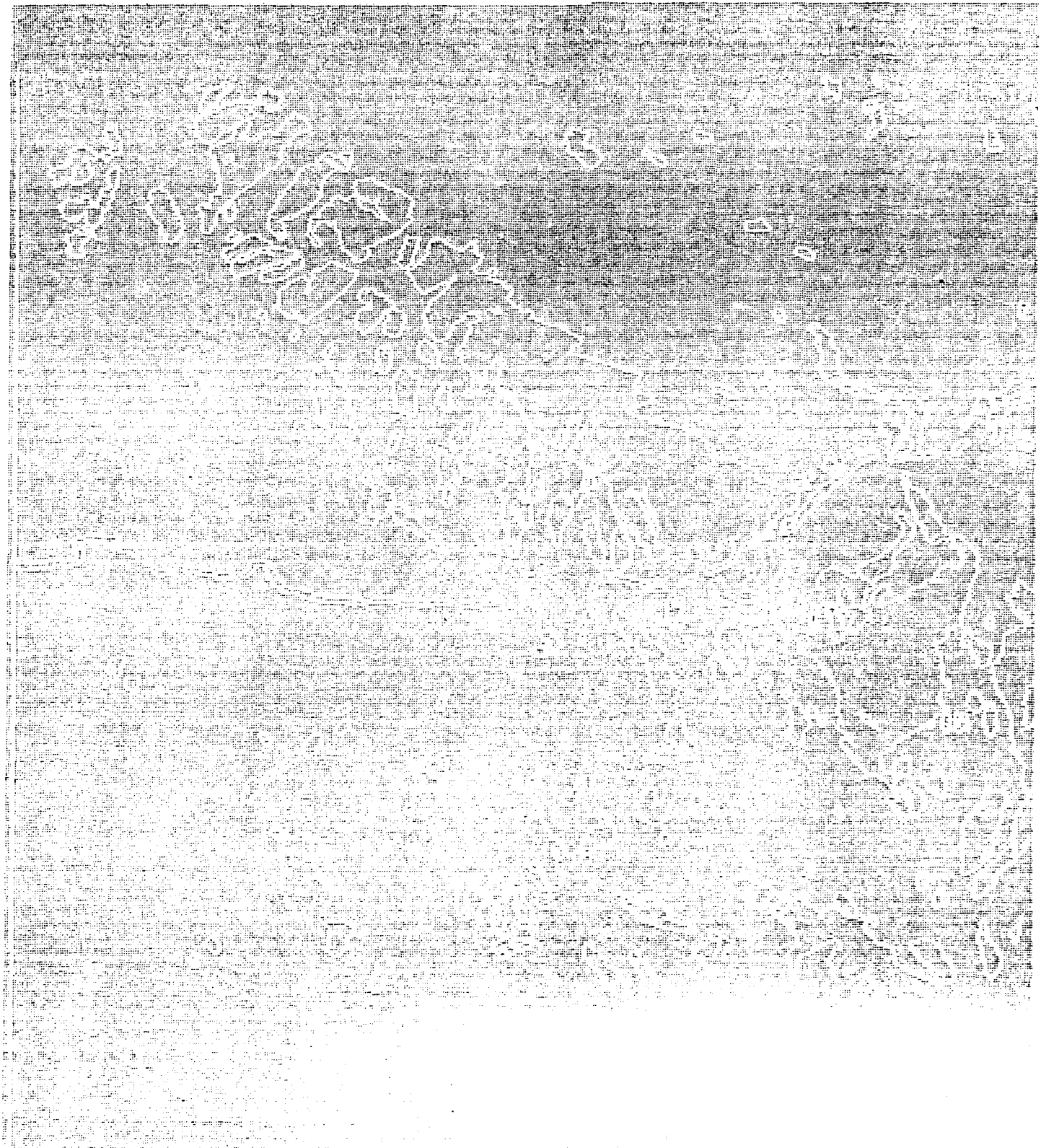
STAR-2 Image of Brazeau Range Area
Preprocessing: Lee sigma filter
Threshold by bimodal histogram
Sobel edge image
Threshold at mean + sigma

Figure 4.11



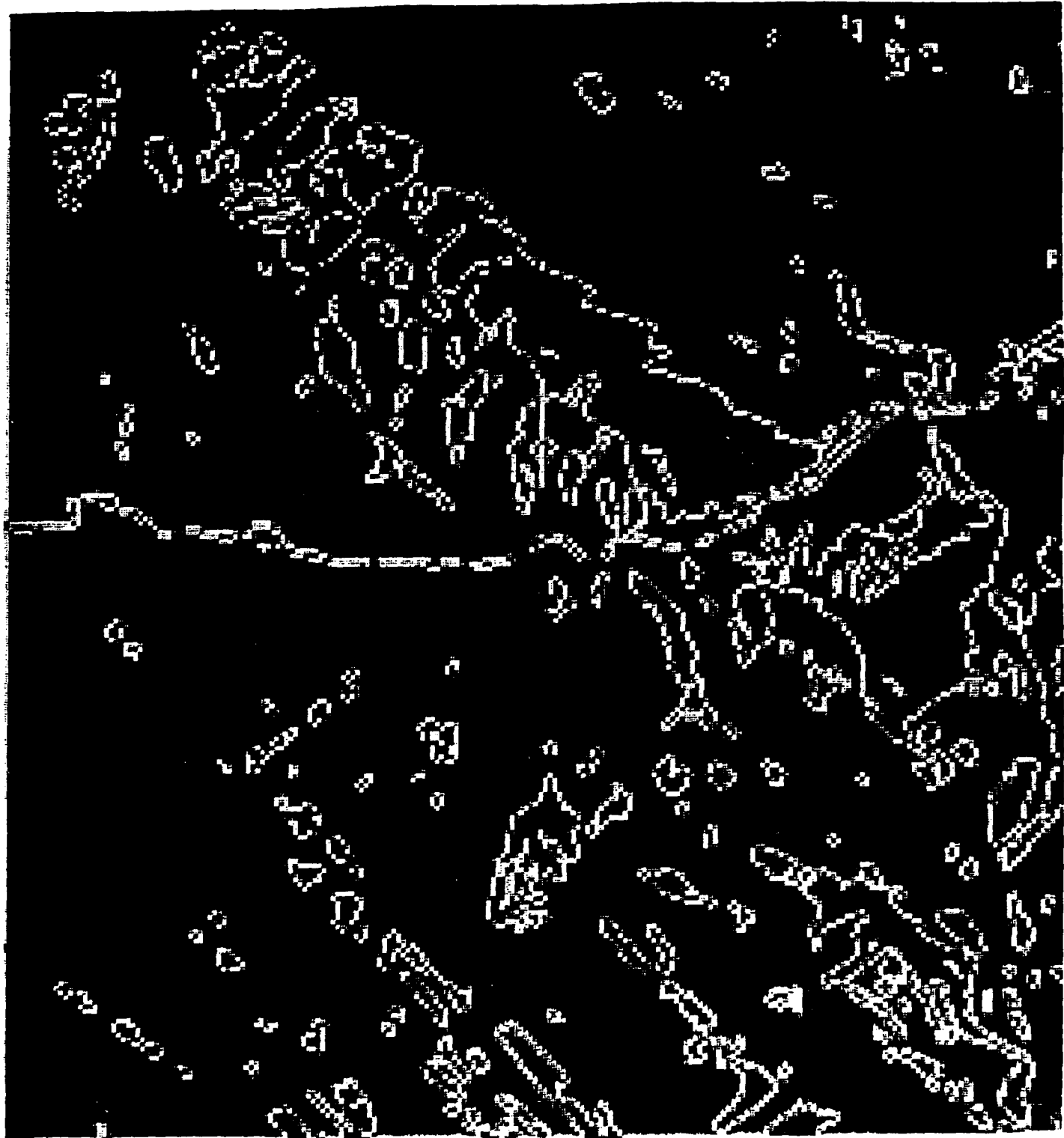
STAR-2 Image of Brazeau Range Area
Preprocessing: Lee sigma filter
Threshold by bimodal histogram
Sobel edge image
Threshold at mean + 2 * sigma

Figure 4.12



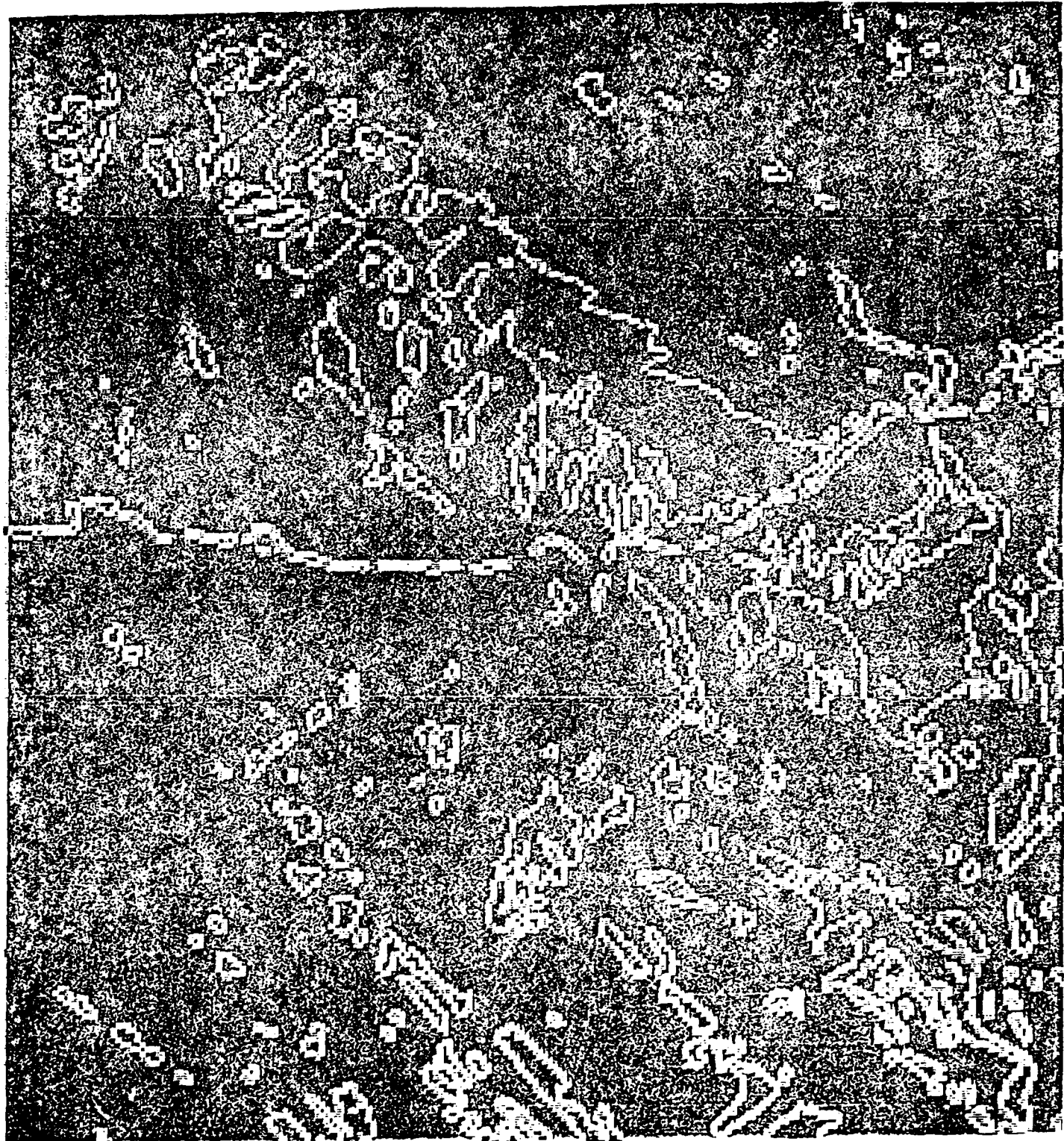
STAR-2 Image of Brazeau Range Area
Preprocessing: Lee sigma filter
Threshold by bimodal histogram
Vectorization of edges

Figure 4.13



STAR-2 Image of Brazeau Range Area
Preprocessing: Lee sigma filter
Threshold by bimodal histogram
Vectorization of edges
2X resolution reduction

Figure 4.14



STAP-2 Image of Bradeau Range Area
Preprocessing: 10x sigma filter
Threshold by bimodal histogram
Vectorization of edges
2X resolution reduction

Figure 4.15

Subsampling the Feature Mask

Digital Feature Analysis Data

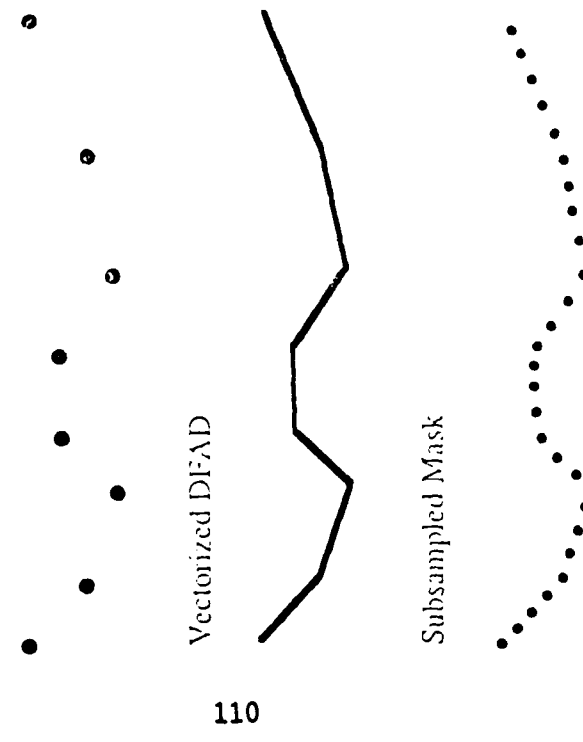


Figure 4.16

Threshold Selection

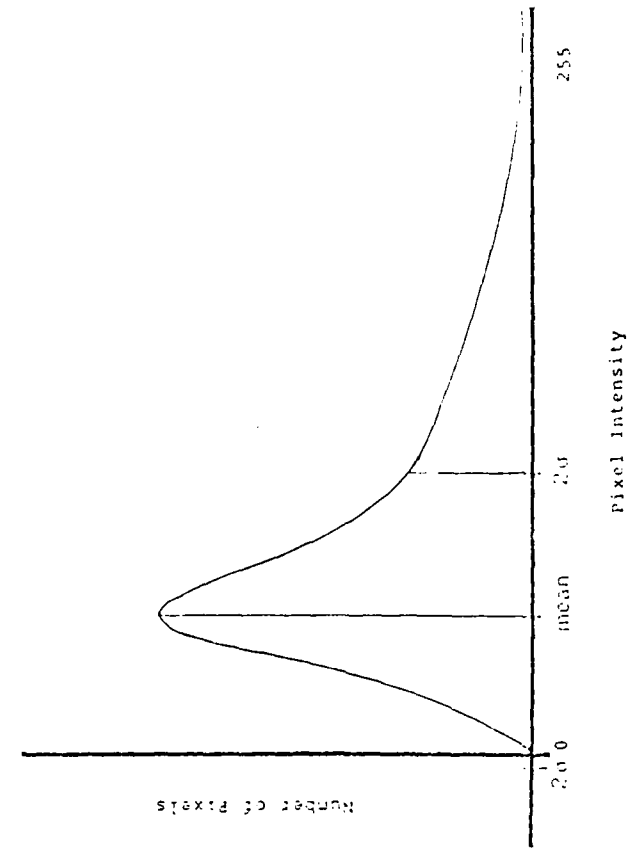


Figure 4.17

5.0 Generation of Control Information Using Image Segment Data

Image segments or "chips" are another way to describe a map feature. Such a segment is an image of the given feature as well as some of the surrounding area. One way to find the given feature in the sensed image is to attempt to register the segment with some region of the sensed image.

Another way would be to also have a description of the given feature, such as a polygonal approximation, along with the image segment. Then a combined boundary match and regional match approach would be possible.

VEXCEL has created a particularly efficient algorithm to estimate relative translations of a pair of opposite-side satellite SAR images. VEXCEL has also developed a boundary-based algorithm for registering objects which have undergone translation and rotation between two images. These two algorithms are described in section 1.3.3.2.

Another approach for estimating relative translation of one image relative to another is similar to phase correlation, but is possibly more efficient. Briefly, this proposed method is as follows:

- (1) Perform some type of high-pass filtering of both images to enhance the edges and de-emphasize the slowly varying regional content.
- (2) Compute the FFT of both images.
- (3) For each complex frequency $f_k^{(1)}$ in image 1 and the corresponding complex frequency $f_k^{(2)}$ in image 2, form the normalized difference $(\phi_k^{(1)} - \phi_k^{(2)})/(2\pi i f_k^{(1)})$ where $\phi_k^{(1)}$, $\phi_k^{(2)}$ are the corresponding phases (formed from the quotients of the magnitudes of the imaginary and real parts of the complex amplitude of a frequency).
- (4) Analogous to the Hough transform, form clusters of the values of these normalized phase differences. By the Fourier Translation [Champeney, 73] Theorem, a relative phase difference for the same frequency in two images corresponds to a relative translation of this frequency in the two images. Any translation of a substantial amount of feature data will lead to a substantial number of corresponding frequencies shifted by a common phase difference amount. This common phase difference will be observable as a cluster of values in the list of corresponding phase differences.

This method has potential for sub-pixel registration, since the phases arise as quotients of the magnitudes of imaginary and real frequency amplitudes. These quotients are not limited to integral values.

This method, along with other image-image matching schemes, will be investigated during the Options to the Base Contract.

6.0 Generation of Control Information Using Satellite Ephemeris Data

Registration of orbital SAR imagery to maps is difficult because of range distortions due to terrain relief and azimuthal distortions due to earth rotation and pointing errors. In the past, pointing errors have involved a linear skew for imagery such as SEASAT and SIR-B. This skew was removable by the use of control points and rubber sheet interpolation. However, these pointing errors will be a problem for SIR-C and X-SAR imagery because of the nonlinear distortions associated with their associated larger doppler shifts [Curlander,87].

Other errors and their sources for satellite SAR are [Curlander,82]:

- o Range errors
 - geoid errors
 - undetected delays in data collection hardware
 - ground range nonlinearities
 - incidence angle varies across swath, so ground resolution of each time sample is not uniform
 - incidence angle is function of terrain
- o Azimuth errors
 - synchronization errors between ephemeris data and returning radar echoes
 - GSFC tapes have ephemeris data for 1 m intervals
 - SEASAT SAR processing interpolates these for 1 ms intervals
 - missing azimuthal lines
 - azimuth skew because doppler shift is function of latitude and position within swath

Azimuth skew can be dealt with by more complex processing with respect to zero doppler, or by post-processing deskewing using control points.

Also, the look angle tends to amplify ground location errors, since:

$$\Delta E_r = \Delta R / \sin \alpha$$

where:

α = radar angle of incidence from vertical

ΔR = range offset

ΔE_r = location error on ground in range direction

Therefore, reducing this look angle will reduce this ground range error effect.

Some of the refinements to the process of associating an earth location with pixels are used in a process called "geocoding" [Curlander,87]:

- o More accurate geoid.
- o More accurate accounting of delays in timing calibration of range measurements.
- o Taking into account the SAR processing-induced skewing of iso-range lines to more correctly compute slant range for a given pixel.
- o Use of doppler function that takes into account earth rotation
- o Use of doppler plane at center of radar beam as a function of time instead of pointing direction of antenna.
- o Use of terrain model.

More accurate analysis of the doppler function for the satellite case is described in [Li,85], where it is shown that there are two dominant terms for the matched filter doppler function: doppler centroid and doppler frequency rate.

The doppler centroid term is:

$$f_{DC} = (-2_r \cdot \bar{R}_r \bar{v}_r) / (\lambda R)$$

Errors in performing the SAR correlation with errors in this term of the matched filter will lead to degradations in the signal to noise ratio and the signal to ambiguity ratio.

The doppler frequency rate term is:

$$f_{DR} = 2(\bar{v}_r \cdot \bar{v}_r - \bar{R}_r \cdot \bar{A}_{sc}) / (\lambda R)$$

Errors in this term for correlating the raw SAR data lead to de-focusing.

Here:

$\bar{R}_t(t)$ = position of target on Earth surface at time t

$\bar{R}_{sc}(t)$ = position of spacecraft radar at time t

$\bar{R}_r = \bar{R}_t(0) - \bar{R}_{sc}(0)$

$\bar{v}_t(t)$ = velocity of target on Earth surface at time t

$\bar{v}_{sc.}(t)$ = velocity of spacecraft radar at time t

\bar{v}_r = $\bar{v}_t(0) - \bar{v}_{sc}(0)$

\bar{A}_{sc} = acceleration of spacecraft radar at time t

λ = radar wavelength

Higher quality attitude and ephemeris information can lead to improvements in processing the raw SAR data using these frequency terms. However, methods are also discussed in [Li,85] for estimating these two terms from the raw radar return data.

7.0 Rule-Based Issues for Generation of Control Information

Five sources of control information are described in this report:

- o INS
- o GPS
- o Terrain-induced shadows
- o Terrain-induced shading
- o Planimetric features

What is required is an overall, top-down, coherent strategy for using these various sources and their combinations under the appropriate circumstances. All of these sources have advantages and disadvantages, requirements, and various degrees of achievable control accuracy.

One way to formulate the expertise required to correctly exploit these multiple sources is by the use of a rule-based system. Other options for incorporating heuristic knowledge include the use of frame-based methods [Minsky,75], which use a template approach for representing "typical" situations.

There are some potential problems when dealing with rules. A rule-based approach can be difficult to implement for situations involving complex relationships [Mettrey,87]. Such systems could potentially become difficult to understand when there is a large number of rules, unless the rule set is hierarchically organized.

However, rules do provide a format for incorporating knowledge that is relatively simple and easy to use. Moreover, the approach that will be followed will be to use a top-down approach for creating and organizing the rule set. Therefore, the rule set should be understandable even as it grows.

Such a system would be somewhat misnamed as an "expert system", since an argument may be given that whenever one is operating strictly according to rules, one is really operating at the level of the advanced beginner. A real expert, on the other hand, is able to create new rules based on experience, modify and find appropriate exceptions to existing rules, and can make novel hypotheses.

Nevertheless, the output from such a rule-based system is potentially very helpful in average situations which would not require any extraordinary interpretation by a human expert in radargrammetry. We shall call such a system a "rule-based assistant".

Such an rule-based assistant would decide which procedural modules to execute and would evaluate their outputs using its knowledge base consisting of rules. These rules are based on heuristics and "rules of thumb" commonly employed by practicing experts.

In this sense, the value of a rule should be its applicability in a wide variety of cases. The existence of exceptional cases should not detract from the value of a particular rule.

Rules with negative conclusions are important also. For example, a rule which cautions against picking a certain feature under a particular circumstance is as useful as one which positively chooses it under different circumstances. Such reasoning allows the system to eliminate possibilities.

There is often a "gray area" between positive and negative rules wherein it is not clear that a particular feature is suitable or not. Such ambiguities result because rules that eliminate a candidate feature are not necessarily converses of rules that positively choose a candidate.

The result is that most rules do not give necessary and sufficient conditions for choosing a particular feature for control. Therefore, there is always the possibility of inserting new rules that are inconsistent with the existing knowledge base. This is always a potential problem for large rule-based systems.

However, such occurrences should be relatively rare if the knowledge base is suitably organized in a top-down hierarchy. Then many rules are often partial converses of other rules.

Although the present study is not concerned with the explicit construction of such a rule-based system, the organization and content of the knowledge-base will be discussed. The content of this knowledge is first expressed in meta-rules, which will be subsequently translated into actual coded rules in a non-procedural language. Some of these meta-rules appear in section 7.2.

This rule-based effort has just begun under the last part of the Base Contract, and will continue during the additional Options.

7.1 Overview on Rules for Image Control

Regardless of sensor type, the output of a rule-based system for generation of image control must determine the following (see Fig. 7.1):

- o Choice of control type
- o Computation of control
- o Estimation of control accuracy
- o Conflict resolution

The categories of control information include INS, GPS, terrain-induced shadows, terrain-induced shading, and planimetric features (see Fig. 7.2). A selection of a single type or multiple types of control would be made.

Choices may also be appropriate within a control type. For example, if planimetry is chosen, then the question of which planimetry features to search for first is important. These selections are based on both image formation and image processing considerations. This module is rule-based.

Image Control must be computed from the control type or types selected. This module is entirely procedural, and represents computations such as in sec. 3.2.2.

An estimate is also required to determine the potential accuracy of control given the distribution of control features. This estimate may or may not indicate the necessity for obtaining additional control information. This module is also procedural.

Finally, conflicts or ambiguities may arise. Some capability for resolution of such problems is required for deciding to obtain additional control or for re-evaluating the accuracy of obtained control. This module, shown in Fig. 7.1, would resemble a diagnostic system and is rule-based.

Expanding the planimetry box in Fig. 7.2 shows the organization of how planimetry is chosen and evaluated as shown in Fig. 7.3. Two types of reasoning are used for evaluating a potential feature.

One way is to use "first principles" from the basic physics of electromagnetics which qualitatively evaluate the strength of the signal response. Another way is to use "rules of thumb" from practicing photo-interpreters and image processors.

In the area of image formation, such empirical rules are also ultimately related to physical principles. However, they may be easier or more convenient to state in a single heuristic form, rather than as a consequence of a combination of physical principles.

In the area of image processing, empirical considerations are important also. Some features are computationally easier to locate than others. Rules representing such choices would also be best categorized as "rules of thumb".

Finally, there exists a module for forming composite evaluations of features based on multiple individual evaluations.

Fig. 7.4 shows the organization of the rationale for employing basic physical principles to the evaluation of planimetric features. The relevant physical characteristics clearly pertain either to the object or to the sensor scenario. The sensor scenario, shown in Fig. 7.6, relates to SAR, optical, or IR. In Fig. 7.7, the SAR scenario concerns effects due to wavelength, polarization, spatial resolution, the direction of the flight path relative to the object, and the signal power. The characteristic properties of the feature object important to imaging are shown in Fig. 7.8, and concern size, surface roughness, and dielectric constant.

Rules of thumb are partitioned, as in Fig. 7.5, into considerations involving the imaging formation scenario, as shown in Fig. 7.9, or issues related to the computational complexity of image processing procedures for extracting the feature from the image.

An observation that can be made concerning such a top-down development of rules is that the rules become more specialized and detailed as a function of depth in the structure chart represented by Fig. 7.1 to 7.9.

7.2 Meta-Rules

To organize the development of meta-rules as described above, an indexing scheme will be helpful which immediately identifies the rule as belonging to a particular hierarchical level as shown in Fig. 7.1 to 7.9. Therefore, rules which decide which category of control to select, as in Fig. 7.2, will be labeled with a prefix "2.", followed by an index number which distinguishes rules at that level.

Meta-rules are stated in the form: If (hypothesis) then (conclusion). The notation "HN1.N2" refers to the hypotheses of Rule N1.N2.

The accuracy estimation module, shown in Fig. 7.1, will be denoted by "AM". This module is a procedural function of its inputs. These inputs can be measurements from any combination of control types. Another input would be the required accuracy E. Given these inputs, the function AM will then decide whether or not the input measurements support the required control accuracy.

As an example, we denote whether the estimated accuracy using planimetry, shadow, and accuracy inputs is acceptable or not by $AM(\text{planimetry}, \text{shadows}, E) = \text{Yes or} = \text{No}$.

Another procedural module with inputs is the control computation module, denoted $CT(\)$. The input could be of more than one control type. For example, the notation $CT(\text{planimetry}, \text{shadow})$ indicates that control should be computed for an image with planimetry and shadow data.

Finally, the notation $GPS = \text{Yes or} = \text{No}$ indicates whether or not GPS data is available in a given scenario. However, in order to make the notation tractable, an abuse of notation will be permitted. Terms such as "planimetry" will be used to indicate an input type for a functional module such as AM or CT, as well as to indicate a logical variable (which is either = Yes or No) to indicate availability of that type of data.

7.2.1 Meta-Rules at Level 1.

Meta-Rules at this level correspond to Fig. 7.1 and are concerned with requests for activation of modules for: control selection, control computation procedures, procedures that estimate control accuracy, and resolution of conflicting or ambiguous information.

Some of the possible conclusions at this level are:

C1.1: The required control accuracy cannot be achieved.

C1.2: The required control accuracy can be achieved.

The first rule is a negative result. It simply states that if all available control for SAR imagery has been tried without success, then there is nothing more to be tried.

Rule 1.1:

If (sensor = SAR) and (GPS = No) and
($AM(\text{INS}, \text{planimetry}, \text{shadows}, E) = \text{No}$)), then (C1.1)

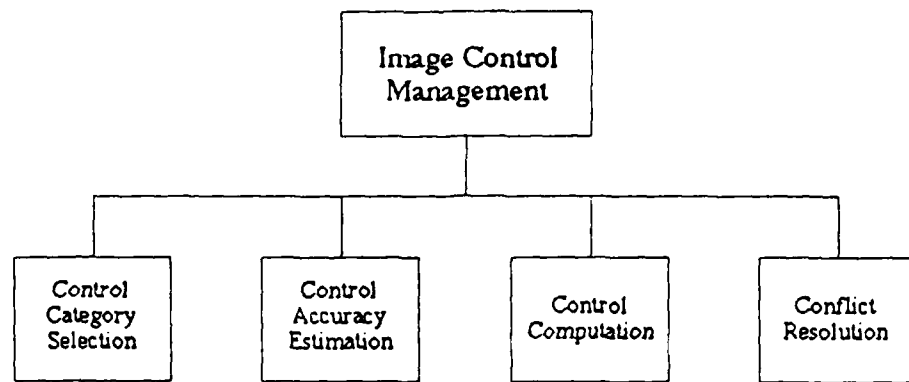


Fig. 7.1
Top-Level View of Image Control

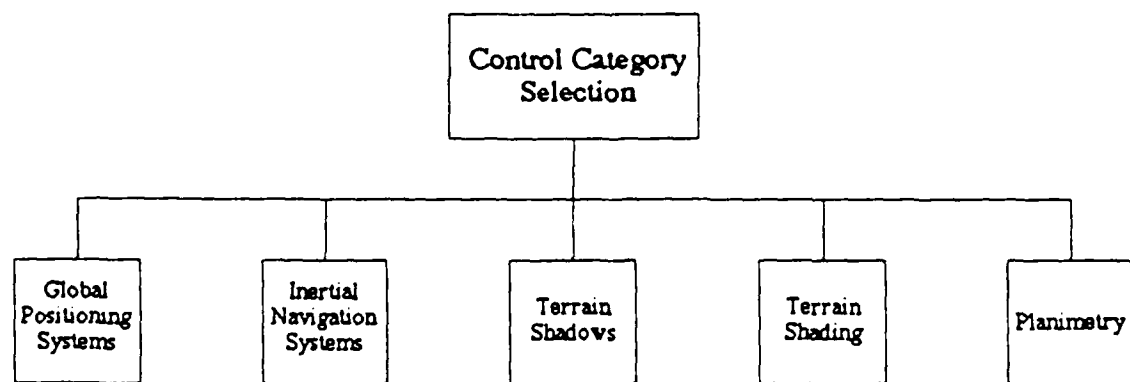


Fig. 7.2
Types of Image Control Information

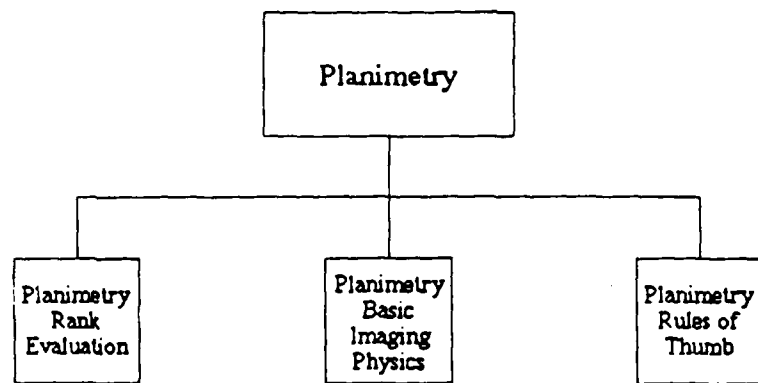


Fig. 7.3
Criteria for Choice and Evaluation of
Planimetry Features for Control

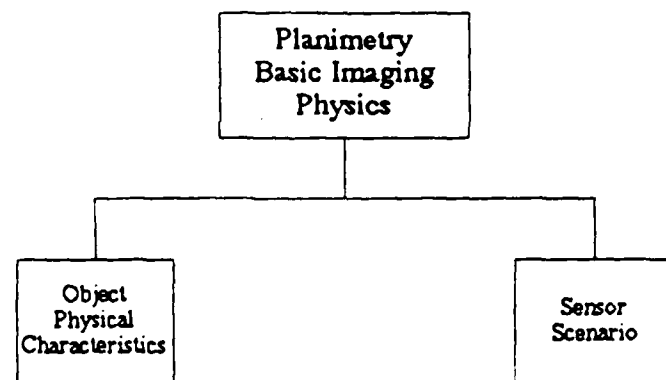


Fig. 7.4
Basic Physics of Received Signal as a
Function of Object and Sensor

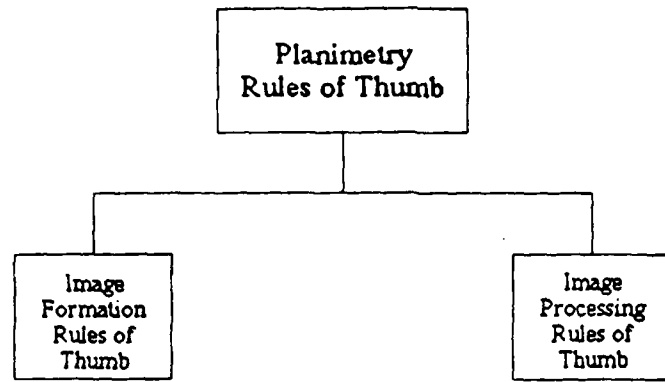


Fig. 7.5
Heuristic "Rules of Thumb" Based on
Imaging and Feature Extraction Considerations

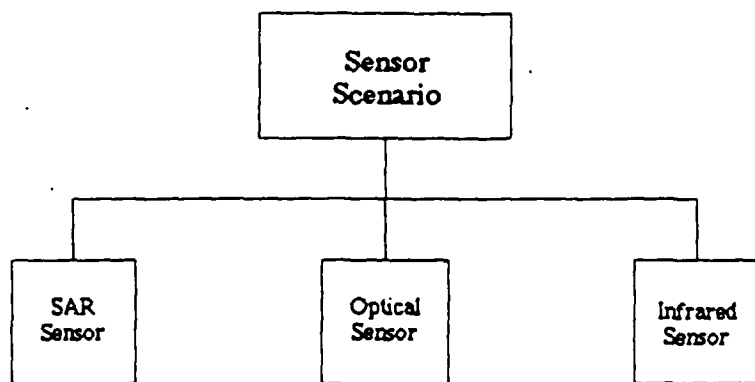


Fig. 7.6
Three Sensor Types Considered

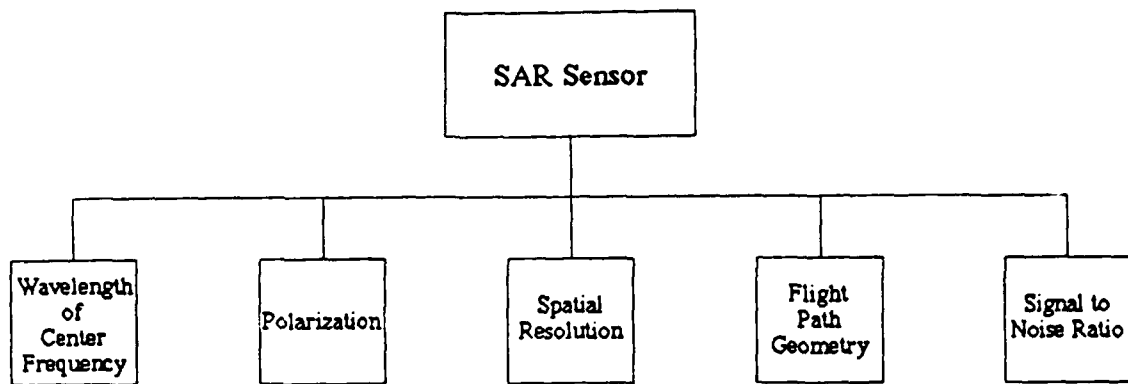


Fig. 7.7
Sensor Physical Determinants for SAR
Feature Detectability

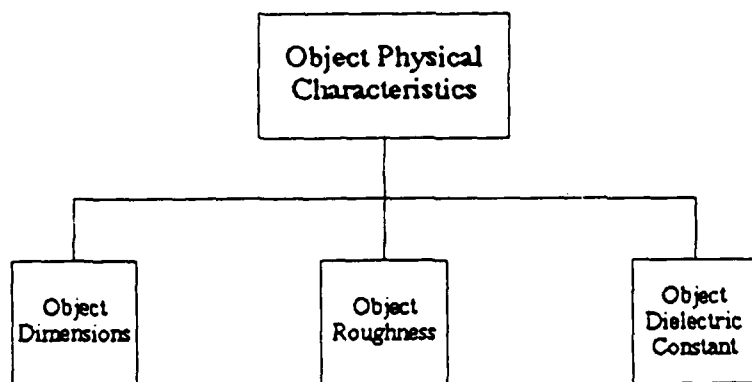


Fig. 7.8
Object Physical Determinants for
SAR Feature Detectability

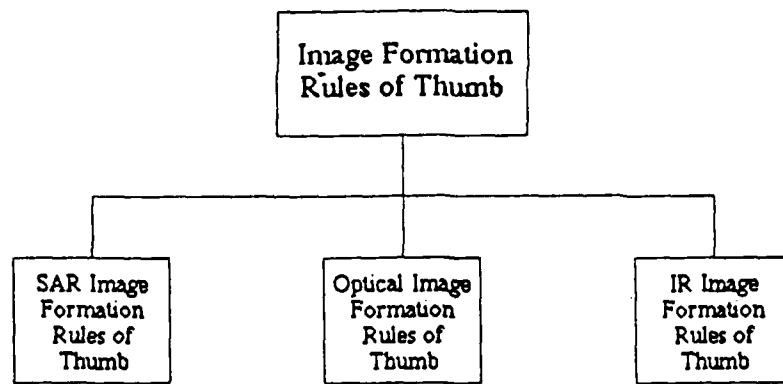


Fig. 7.9
Heuristics Concerning Sensor Characteristics
Influencing Feature Detectability

7.2.2 Meta-Rules at Level 2.

Meta-rules at this level correspond to selections at the level of Fig. 7.2, and are concerned with selecting the most appropriate category of control from the available categories.

The first rule concerns the superior accuracy of GPS.

Rule 2.1:

If (GPS = Yes), then (CT(GPS))

The next rule accepts the high relative accuracy of INS, but requires some additional control for achieving absolute accuracy. A hierarchy of desirable control supplements to INS is now given. The first choice will be the use of planimetric data.

However, the appropriate planimetric data must be available and identified before control computation and evaluation can take place. The precise identification of particular planimetric data will take place by the backward-chaining of rules in the lower levels of the hierarchy. But at this level, all that is required is an indication of whether or not such data is available, and if so, its usage in the functions AM and CT.

Rule 2.2:

If ((GPS = No) and (INS = Yes) and (planimetry = Yes)), then (CT(INS,planimetry) and AM(INS,planimetry,E))

Rule 2.3:

If ((H2.2 = Yes) and (AM(INS, planimetry,E) = Yes)), then (C1.2)

The next rule chooses terrain-induced shadow matching as a supplement for planimetry in the case of SAR imagery.

Rule 2.4:

If ((H2.2 = Yes) and (AM(INS,planimetry,E) = No) and (sensor = SAR) and (shadow = Yes)), then (CT(INS,planimetry,shadow) and (AM(INS,planimetry,shadow,E)))

Rule 2.5:

If ((H2.4 = Yes) and (AM(INS,planimetry,shadow,E) = Yes)), then (C1.2)

The next rule chooses terrain-induced shading to supplement shadow matching.

Rule 2.6:

If ((H2.3 = Yes) and (AM(INS,planimetry,shadow,E) = No)) and (shading = Yes)), then (CT(INS,planimetry,shadow,shading)) and (AM(INS,planimetry,shadow,shading)))

7.2.3 Meta-Rules at Level 3:

The rules at this level correspond to selections within each of the modules in Fig. 7.2 for GPS, INS, SAR shadows, shading, or planimetry.

7.2.3.1 Planimetry

The rules for evaluating planimetry are first partitioned in Fig. 7.3. There, the methods involve basic physical principles and "rules of thumb". A candidate planimetric feature is separately evaluated in terms of each of these two methods, and a composite rank evaluation is then made.

This composite evaluation will also be used to determine whether any feature's score is high enough to merit the declaration: planimetry = Yes. This means that there is at least one feature which is reasonably capable of being detected in the imagery under the circumstances.

7.2.3.1.1 Planimetry Rules of Thumb

The heuristics, or rules of thumb, relevant to the extraction of planimetry involve the capabilities to both sense features and extract these sensed features from imagery, as shown in Fig. 7.5.

7.2.3.1.1.1 Image Formation Rules of Thumb

Some of the heuristics that must be incorporated as rule-based knowledge about imaging features include a list of commonly recognizable objects. For SAR, these include:

- o natural
 - terrain relief
 - lakes
 - rivers
 - tree lines
 - shorelines
- o man-made
 - power lines
 - railway lines
 - pipelines
 - seismic lines
 - roads

- bridges
- dams
- urban areas
- power plants
- airfields
- strip mines
- oil platforms

Other knowledge that must be incorporated are heuristics concerning conditions for visibility and non-visibility in SAR images for such features as those listed above. Such heuristics include:

- o Lakes may or not create specular returns depending on the surface roughness.
- o Lake boundaries may be difficult to distinguish precisely because of water level changes and imaged mud banks.
- o Corner reflections make urban areas visible, but with indistinguishable boundaries. Therefore, such regions are only suitable for very approximate location estimation.
- o Thin objects, such as pipelines and power lines, are sometimes not visible themselves but often lie in visible forest clearings.
- o Roads are often only visible if they are roughly in the direction of the flight line.
- o Features that should be visible could be obscured by other nearby, tall features because of radar layover.
- o Sometimes, near range "striping" is observed that is due to sidelobe effects.
- o A false, linear signature, punctuated by periodic highlights, can be due to imaging a moving aircraft.

It will be important to incorporate these and other "rules of thumb" for evaluating feature matches. They will also be important for giving possible explanations of why certain features which should ordinarily be detectable in computed image locations, based on other feature matches, are not visible in a particular situation.

8.0 Spatial Database Issues

The issues addressed in this section concern appropriate data structures for spatial databases, and the database management functions for interfacing the control generation procedures with a spatial database.

8.1 Data Structures

The following discussion represents a selective overview of data structures suitable for internally representing spatial data in a database. Such structures must be organized to efficiently support the geometrically-oriented queries that are common to spatial database transactions. Typical examples of such geometrical operations are containment, closest point, adjacency, and intersection [McKeown,84]. Additionally, such a database must support the maintenance of various source types of spatial data, such as imagery, maps, terrain models, etc.

A number of such structures representing spatial data have been developed. One approach is via spatial decomposition. Another approach encodes feature information in the form of point coordinates and vectors.

Recursive decomposition of the area or volume to be represented is the basis for methods employing quadtrees, ninetrees, and segments. Hexagonal structures have been used for non-recursive decomposition.

Reviews of the quadtree concept can be found in [Samet,84]. Although quadtrees in their basic form are strictly areal structures, techniques have been developed to encompass the representation of linear features and the boundaries of areal features. Such techniques involve conversion algorithms to place boundary data or vector data into a quadtree representation and vice-versa [Samet,84], [Dyer,80], [Nelson,86]. The use of "linear quadtrees" [Gargantini,82] increases the efficiency with which quadtree data can be manipulated within memory. Another generalization of the quadtree concept is k-d trees [Bently,75], which are based on the correspondence between quadtree representations for point data and multidimensional generalizations of binary search trees [Finkel, 74].

Recursive segmenting decomposition of linear features into smaller and smaller segments, each one represented by an elongated rectangle containing it, is the basis of strip trees [Ballard,81].

Three-by-three areal decomposition is the basis of the nine-tree concept [Raetzsch,85]. This structure offers some computational simplifications over the quadtree.

Hexagonal decomposition leads to an addressing scheme known as the Generalized Balanced Ternary representation [Gibson,84].

Data structures based on point and vector coordinate lists have been examined in [Kropatsch,81]. In this formulation, point coordinates are maintained in lists ordered so that the vectors and polygons defined by those points are represented by the location of those coordinates in the list. Additionally, pointers are

used to link related vectors represented in differing places in the coordinate list. A geographical information system being developed at Kork Systems, Inc. uses such a point/vector format with associated attributes in a layered organization in order to group features by location and size. The design of query languages which efficiently exploit such data structures for efficient search is considered in [Frank,1982].

The greatest advantage of a point/vector format for map database management and the generation of ground control information for registration is the logical similarity between this type of representation and the likely ground control features present in maps and images. Such features are usually line segments, curved boundaries, intersections of segments and boundaries, and centroids of areal features. Areal decomposition representations, such as quadtrees and similar structures, are not as well suited to the representation of such features.

8.2 Database Management Functions

In general, the management of spatial data imposes special requirements on a database management system (DBMS). Moreover, the particular application of control generation must be considered. The type of spatial DBMS which is relevant to this section is one which supports the particular application of control information generation.

To this end, spatial databases must support geometrically and spatially oriented queries, as well as queries which involve non-geometric, relational entities.

Some typical queries to spatial databases that are relevant to the image control problem addressed in this effort involve computations such as: geographical containment as a function of location uncertainties, line-of sight obscuration, existence and usage of sufficient terrain relief, as well as feature type, location, and direction. Moreover queries may often occur as combinations of the above.

A traditional relational organization could, in principle support such non-relational database queries. However, non-spatially oriented relational databases have structural and performance problems associated with handling spatial data. Among them are the variable length records associated with variable length lines, the dispersion of attributes over multiple tables, and a generally awkward link structure between features [Keating,87].

Therefore, to achieve efficient performance, the organizational structure of the database should be compatible with the different types of queries that are expected.

This implies that a spatial database should contain multiple levels of organization to support the different types of queries. Therefore, data must be organized on a geographic and geometric basis, as well as the traditional relational basis.

Further improvements in performance can be achieved if the physical organization of geometric data is closely compatible with its logical organization. In particular, disk file records for geographically clustered items should also be physically clustered. Additionally, memory resident DBMS operations and internal buffering according to entity types and spatial domains will also increase response time efficiencies [Keating,87].

A factor which influences flexibility in the continued use of such databases is object-oriented design. Such an approach would more easily allow the addition and deletion of attributes of geometric and geographic data without requiring changes in the overall logical structure of the database.

9.0 Summary and Conclusions

Some conclusions can be drawn from this preliminary work. A terrain database can be exploited to obtain matching data between a real and synthetic SAR image for the purposes of obtaining image control. However, the resection in space will generally be ill-conditioned if all the matches are within a narrow value for range. Therefore, what is required is rugged terrain features for casting radar shadows at more than one range offset, or the use of another source of control, such as feature matching, at other range offsets. These issues are discussed in sec. 3.

Feature matching also has good potential for computing image control, provided that suitable features can be selected, and that an efficient search process is used to locate them in the image. These issues are discussed in sec. 3 and 7.

10.0 Appendices

This section briefly describes some of the general issues involved in calibrating imagery for registration with maps or for stereo. Especially important is the problem of resection in space, or exterior orientation.

10.1 Photogrammetry

Most frame-based optical camera systems are based on central perspective transformations of 3-D Euclidean space to 2-D Euclidean space. Other sensor types, such as Synthetic Aperture Radar [Leberl,83] or scanned image arrays require a different geometric model. We will assume central perspective as the idealized transformation model in the following discussion.

The full determination of a stereo model also requires knowledge of the relative geometries of the two stereo images, a model of the distortions which are perturbations to the central perspective model, and the relationship of the imaging sensor to a ground coordinate system. In photogrammetry, such relationships are comprised in the determination of four types of orientation: interior, exterior, relative, and absolute.

For a single image, the interior and exterior orientations are relevant. Determining the interior orientation refers to the process of reconstructing the internal geometry of light bundles within the optical system. The relevant parameters to be determined are the focal length, the image coordinates of the principal point, and a model of the lens distortions which cause deviation from a central perspective transformation. Typical of such distortions are symmetric radial distortion and asymmetric lens decentering. Coefficients quantifying these parameters are obtained during the camera calibration process.

Determining an exterior orientation refers to the process of relating the coordinate system of the imaging sensor to a ground coordinate system. This essentially requires the determination of the geographic position of the exposure center and the direction of the optical axis.

For a pair of images, the relevant orientations, neglecting distortions, are the relative and absolute orientations. In principle, one could determine an interior and an exterior orientation for each image separately, and from these also obtain the relative relationship between both images. However, such a procedure would not deal with measurement errors and inconsistencies as well as using both images simultaneously to estimate the relative geometry between them and to relate image coordinates to ground coordinates. Distortions must be accounted for by either an interior orientation separately for both images, or in a bundle adjustment for both images simultaneously.

The relative orientation of a stereo pair is concerned with the relative position and attitude of the image coordinate systems of the two images. The aim of a relative orientation determination is to find that relative orientation of both images such that all light bundles through corresponding image points intersect. Because of the inevitable distortions in the lenses, the atmosphere, and photographic processing, a "best fit" orientation is determined which minimizes some total measure of bundle intersection discrepancy.

The parameters that are sought are two relative position coordinates perpendicular to the line segment joining the perspective centers, and three rotational transformation parameters describing the rotation between the two coordinate systems. The length of the segment joining the perspective centers is usually not computed in the determination of relative orientation, since this parameter influences the scale of the model. Scale is determined in absolute orientation.

Absolute orientation determination involves determining the scale of the model, "leveling" the model, and determining the position of its origin in a ground coordinate system.

Bundle adjustment is a method for integrating the two operations of relative and absolute photo-orientations into a single operation, possibly using a number of images which cover some area. This method can be used for simultaneously estimating distortions in a stereo pair of images. Such a simultaneous estimation method allows for better estimates than are available from individual interior orientation determinations.

In the case of one pair of images, this process would decompose the problem into a non-statistical and a statistical subproblem. The non-statistical portion would involve determining an arbitrary scale and orientation for the model. These can be accomplished by arbitrarily assigning (x,y,z) coordinates to two corresponding points in the image pair, and by specifying a model rotation about the line connecting these two points. These two points and the rotational angle constitute seven degrees of freedom.

The statistical portion would involve identifying some number of corresponding point pairs to estimate the lens distortion coefficients.

10.2 Radargrammetry

"Resection in space" is the photogrammetric term for calculation of the elements of the exterior orientation (see section 9.1) for a central perspective imaging sensor. This orientation is the set of geometric parameters that describe the imaging process. For a central perspective optical camera, it involves the position of the perspective center and the orientation of the focal plane.

For a SAR, it is a description of the flight path, during imaging, as a function of time. Such a flight path for an aircraft would ideally be a straight line of constant altitude. However, because of aerodynamic effects, this is obviously not achievable in practice. Short-term departures from such a straight-line flight path can be estimated from the INS or INS/GPS data. Especially important are the velocity errors and distance offsets from the nominal flight line.

Using such data, real time phase-history and range-gating corrections can be implemented in a real time SAR processor to process the data as if it were being imaged along a nominal straight line flight path with constant velocity (see section 2.3.4). Residual errors still exist, of course, because of imperfect corrections.

Because of these residual errors, however, the radargrammetric formulation of resection in space requires a time-dependent formulation of the flight path parameters. These range-projection equations are [Leberl,83]:

$$r - |\bar{p} - \bar{s}(t)| = 0 \quad (\text{range equation})$$

$$\bar{s}(t) \cdot (\bar{p} - \bar{s}(t)) - \sin \lambda |\bar{s}(t)| |\bar{p} - \bar{s}(t)| = 0 \quad (\text{Doppler equation})$$

where:

\bar{p} is a control point

r is range from sensor to control point at time t

$\bar{s}(t)$, $\bar{v}(t)$ are the instantaneous position and velocity vectors of the sensor platform

λ is the sensor squint angle (squint usually zero for aircraft SAR, nonzero for satellite SAR)

These nonlinear equations are usually linearized using a Taylor's series expansion. The system of equations is then solved for the unknown linear correction for the original estimate. This process is repeated iteratively. Convergence requires good initial estimates.

As described in [Raggam,87], problems of accuracy and convergence remain because of discrepancies between the actual imaging scenario and the initial describing parameters for imaging. Because of these initial inaccuracies, modified procedures have been implemented which attempt to refine the estimates of parameters with the greatest inaccuracies:

- o range offset (constant for azimuthal lines)
- o azimuthal shift (caused by time calibration errors)
- o scaling factors for pixel spacings

Some problems with initial estimates also arise because of correlations among parameters. This seems to be especially a problem in the orbital SAR case, and can involve [Raggam,87]:

- o azimuth shift and squint
- o range offset, pixel spacings, and sensor position

For rugged terrain imaged by satellite SAR imagery, it was found in [Raggam,87] that simultaneous estimation of all parameters was not possible in the orbital case, and that step-wise refinements were required.

11. References

Aho, A. Design and Analysis of Computer Algorithms, Addison Wesley, 1974.

Ayache, N. et al., "A New Method for the Recognition and Positioning of 2-D Objects," ICPR, Montreal Canada, 1984.

Ayache, N. et al., "Efficient Registration of Stereo Images by Matching Graph Descriptions of Edge Segments," Int. J. Comp. Vision, Vol. 1, #2, 1987.

Ballard, D.H., "Strip Trees: A Hierarchical Representation for Curves", Comm. of ACM, Vol. 24, #5, 1981.

Ballard, D. et al., Computer Vision, Prentice Hall, 1982.

Barnea, D.I., et al., "A Class of Algorithms for Fast Digital Image Registration," IEEE Trans. Comp., C-2, #2, 1972.

Barrows H., et al., "Parametric Correspondence and Chamfer Matching: Two New Techniques for Image Matching," Proc. DARPA Image Understanding Workshop, May 1978.

Bentley, J., "Multidimensional Binary Search Trees Used for Associative Searching," Comm. of ACM, Vol. 18, #9, 1975.

Beser, J., "Highly Accurate Hydrographic Surveys Using Differential GPS," IEEE Position, Location and Navigation, 1986.

Bierman, G., "Fixed Interval Smoothing with Discrete Measurements," Int. J. Control, Vol. 18, #1, 1973.

Binford, T., "Survey of Model-Based Image Analysis Systems," Int. J. Rob. Res., Vol. 1, #1, Spring 1982.

Bolles, R. et al., "Recognizing and Locating Partially Visible Objects: The Forms Feature Method," Intl. J. Robot. Res., Vol. 1, #3, 1982.

Bose, S., "GPS/PLRS Aided Inertial Land Navigation System Performance," IEEE Position, Location and Navigation, 1986.

Champeney, D., Fourier Transforms and their Physical Applications, Acad. Press, 1973.

Curlander, J., "Location of Spaceborne SAR Imagery," IEEE Trans. Geosc. Rem. Sens., GE-20, #3, July 1982.

Curlander, J. et al., "A Post-Processing System for Automated Rectification and Registration of Spaceborne SAR Imagery," Int. J. Rem. Sens., Vol. 8, #4, 1987.

De Castro, E. et al., "Compensation of Random Eye Motion in Television Ophthalmoscopy: Preliminary Results," IEEE Trans. on Med. Image., MI-6, #1, Mar 1987.

Divakaruni, et al., "Ring Laser Gyro Inertial and GPS Integrated Navigation System for Commercial Aviation," IEEE Position, Location and Navigation Symposium, 1986.

Dunn, S. et al., "Local Estimation of the Uniform Error Threshold," IEEE Trans. Patt. Anal. Mach. Intell., PAMI-6, #6i, Nov. 1984.

Dyer, C.R. et al., "Region Representation: Boundary Codes from Quadtrees," Comm. of ACM, Vol. 23, #3, 1980.

Farrell, J., Integrated Aircraft Navigation, Acad. Press, 1976.

Finckel, R.A. et al., "Quad Trees: A Data Structure for Retrieval on Composite Keys," Acta Inf., Vol. 4, #1, 1974.

Fischler, M. et al., "Detection of Roads and Linear Structures in Low-Resolution Aerial Imagery using a Multisource Knowledge-Integration Technique," Comp. Graph. Image Proc., Vol. 15, 1981.

Frank, A.U., "MAPQUERY: Database Language for Retrieval of Geometric Data and Their Graphical Representation," Proc. 1982 SIGGRAPH Conf., Boston, MA, 1982.

Gelb, A. ed., Applied Optimal Estimation, MIT Press, 1974.

Gibson, L. et al., Hexagonal DataBase Study (Phase II), Rep. No. ETL-360, U.S. Army Engineer Topographic Labs, 1984.

Goodenough, D. et al., "An Expert System for Remote Sensing," IEEE Trans. Geosc. Rem. Sens., GE-25, #3, May 1987.

Horn, B., Robot Vision, MIT Press, 1986.

Horn, B., et al., "Using Synthetic Images to Register Real Images with Surface Models," CACM, Vol. 21, Nov. 1978.

Huang, T. ed. Image Sequence Analysis, Springer, 1981.

Kalvin, A., et al., "Two-Dimensional Model-Based Boundary Matching using Footprints," Intl. J. Rob. Res., Vol. 5, #4, Winter 1986.

Kleusberg, A. et al., "High Precision Differential GPS Navigation," IEEE Position, Location and Navigation, 1986.

Kropatsch, W. et al., "Automated Registration of Scanned Satellite Imagery with a Digital Map Data Base," DIBAG Publ. #1, Res. Center, Univ. of Graz, Austria, 1981.

Kropatsch, W. et al., Automated Registration of Scanned Satellite Imagery with a Digital Map DataBase, Dept. for Image Processing and Computer Mapping, Graz Research Center, Graz Austria, 1981.

Kuglin, C.D. et al., "The Phase Correlation Image Alignment Method," Proc. IEEE 1975 Conf. on Cyber Soc., Sept. 1975.

Kuglin, C.D. et al., "Map Matching Techniques for Terminal Guidance Using Fourier Phase Information," Proc. SPIE: Digital Processing of Aerial Images, Vol. 186, 1979.

Kwok, R. et al., "Rectification of Terrain Induced Distortions in Radar Imagery," Photog. Eng. Rem. Sens., Vol. 53, #5, May 1987.

Lahart, M.J., "Optical Area Correlation with Magnification and Rotation," J. Opt. Soc. Amer., Vol. 6D, May 1970.

Leberl, F. et al., "Registration of Digitized Aerial Photography with a Digital Map Database," Final Report DAJA37-80-C-0020, USARDSG-UK, 1982.

Leberl, F., "Photogrammetric Aspects of Remote Sensing with Imaging Radar," Remote Sensing Reviews, Vol. 1, 1983.

Lee, J., "Speckle Suppression and Analysis for Synthetic Aperture Radar," Optical Eng., Vol. 25, #5, May 1986.

Li, F. et al., "Doppler Parameter Estimation for Spaceborne Synthetic Aperture Radars," IEEE Trans. Geosci. Rem. Sens., GE-23, #1, Jan. 1985.

Loper, E. et al., "Projected Performance of Smaller Hemispherical Resonator Gyros," IEEE Position, Location and Navigation Symposium, 1986.

Lundberg, J., "A Study of Autonomous Navigation Systems," Final Report POFE 706005, Center for Space Research, Univ. of Texas at Austin, April 1987.

Massatt, P., et al., "2-D and 3-D Characterizations of GPS Navigation Service," IEEE Position, Location and Navigation, 1986.

Maybeck, P., Stochastic Models, Estimation, and Control, Acad. Press, 1982.

McConnell, R., "Matching of Dissimilar Radar Images Using Marr-Hildreth Zero Crossings," Proc. Amer. Soc. Photog. Rem. Sens., Balt. MD, April 1987.

McKeown, D.M., "Digital Cartography & Photo Interpretation from a Database Viewpoint," New Applications of Databases, Academic Press, 1984.

McKeown, D., "The Role of Artificial Intelligence in the Integration of Remotely Sensed Data with Geographic Information Systems," IEEE Trans. Geosc. Rem. Sens., GE-25, #3, May 1987.

Medioni, G. et al., "Matching Images using Linear Features," IEEE Trans. Patt. Anal. Mach. Intell., PAMI-6, #6, Nov. 1984.

Meirovitch, L., Methods of Analytical Dynamics, McGraw Hill, 1970.

Menn, M., "Autonomous Navigation for GPS Via Crosslink Ranging," IEEE Position, Location and Navigation, 1986.

Mercer, B. (Intera), oral communication, 1987.

Mettrey, W., "An Assessment of Tools for Building Large Knowledge-Based Systems," AI Magazine, Vol.8, #4, Winter 1987.

Minsky, M., "A framework for representing knowledge," in Winston, P. (ed), The Psychology of Computer Vision, McGraw Hill, 1975.

Moravec, H., "Towards automatic visual obstacle avoidance," Proc. Fifth Intl. Conf. on Artif. Intell., Cambridge, MA, 1977.

Nelson, R.C. et al., "A Consistant Hierarchical Representation for Vector Data," Computer Graphics, Vol. 20, #4, 1986.

Nevatia, R., Machine Perception, Prentice Hall, 1982.

Pearson, J.J. et al., "Video Rate Image Correlation Processor," Proc SPIE: Applications of Digital Image Processing, Vol. 119, 1977.

Perez, A. et al., "An Iterative Thresholding Algorithm for Image Segmentation," IEEE Trans. Patt. Anal. Mach. Intell., PAMI-9, #6, Nov. 1987.

Pratt, W. "Correlation Techniques of Image Processing," IEEE Trans. Aerosp. Elect. Systs., May 1974.

Pratt, W., Digital Image Processing, John Wiley & Sons, 1974.

Price, K., "Symbolic matching of images and scene models," Proc. IEEE Workshop Comput. Vision, Aug. 1982.

Pun, T., "Entropic Thresholding, A New Approach," Comp. Graph. Image Proc., Vol. 16, 1981.

Raetsch, H., Die Entwicklung einer Datenstruktur fuer die Speicherung und Manipulation Digitaler Technischer Graphic, Ph.D. Thesis, Technical Univ. Graz, Austria, 1985.

Raggam, J. "Experiments to Study Earth Curvature and Topography Impacts on SAR Mapping Accuracy," Proc. First Intl. Workshop on Image Rectification Techniques for Spaceborne Synthetic Aperture Radar, Loipersdorf, Austria, Jan. 1987.

Rosenfeld, A. et al., "Thresholding Using Relaxation," IEEE Trans. Patt. Anal. Mach. Intell., PAMI-3, #5, Sept. 1981.

Rosenfeld, A., et al., Digital Picture Processing, Acad. Press, 1982.

Rosenfeld, A., ed. Multiresolution Image Processing and Analysis, Springer Verlag, 1984.

Samet, H. "The Quadtree & Related Hierarchical Data Structures," Computing Surveys, Vol. 16, #2., 1984.

Sankoff, et al., Time Warps, String Edits, and Macromolecules: The Theory and Practice of Sequence Comparison, Addison Wesley, 1983.

Schwarz, J. et al., "Identification of Partially Obscured Objects in Two and Three Dimensions by Matching Noisy Characteristic Curves," Robotics Report #46, New York Univ., 1985.

Shapiro, L. et al., "Structural Descriptions and Inexact Matching," IEEE Trans. Patt. Anal. Mach. Intell., PAMI-3, Sept. 1981.

Smith, J., et al., "Closed-Form Least-Squares Source Location Estimation from Range-Difference Measurements," IEEE Trans. Acoust. Speech Sig. Proc., ASSP-35, #12, Dec. 1987.

Stein, B., et al., "Equatorial Sparing of the NAVSTAR/GPS 18 Satellite Constellation," IEEE Position, Location and Navigation Symposium, 1986.

Stockham, T. "Image Processing in the Context of a Visual Model," Proc. IEEE, Vol. 60, 1972.

Svedlow, M., et al., "Image Registration: Similarity Measure and Preprocessing Method Comparisons," IEEE Trans. Aerosp. Elect. Systs., AES-14, #1, Jan. 1978.

Teasley, S., "Flight Test Results of an Integrated GPS and Strapdown Inertial System," IEEE Position, Location and Navigation Symposium, 1986.

Triendl, E., "Lokalisierung von durch Zeichnungen beschriebenen Strukturen in Bildern," DAGM, 1981.

Turney, J. et al., "Recognizing Partially Hidden Objects," IEEE Intl. Conf. Robot. and Autom., 1985.